CAD-Based Iris Design Procedures for Multi-Mode Coupled Cavity Devices

Werner Steyn

Dissertation presented for the Degree of Doctor of Philosophy
in Engineering at the University of Stellenbosch

Promoter: Prof. P. Meyer *Date:* March 2002

Declaration

I, the undersigned, hereby declare that the work contained in this dissertation is my own original work and that I have not previously in its entirety or in part submitted it at any university for a degree.

Date:

W. Steyn

Opsomming

Sleutelwoorde: multi-modale golfgeleier resoneerder filters, rekenaargesteunde ontwerp, irisse, diplekser, koppelstruktuur.

Multi-modale gekoppelde resoneerder filters word reeds vanaf die eerste verskyning van kommersiële sateliet-kommunikasiestelsels in 1970 gebruik. Vir hierdie toepassing is die fisiese grootte en massa van die filters in die kommunikasiestelsels van groot belang. Multi-modale filters gebruik meer as een resonante modus in 'n golfgeleier resoneerder om die fisiese grootte en massa van die filter te verminder. Hoe meer resonante modusse in een golfgeleier resoneerder, hoe kleiner en ligter die filter. Die gebruik van meer modusse kompliseer egter die ontwerp van die filter.

'n Baie belangrike aspek van multi-modale filterontwerp is die ontwerp van die irisse wat die golfgeleier resoneerder skei. Die irisse word tans ontwerp, óf deur middel van Bethe se klein iris teorie, óf met die gebruik van 'n standaard numeriese metode. 'n Onlangse studie toon aan dat sekere standaard toevoegings tot Bethe se teorie, benaderings bevat wat tot foutiewe iris ontwerp kan lei. Numeriese metodes is dus noodsaaklik vir akkurate iris ontwerp. Hierdie studie wys egter dat die bestaande numeriese tegnieke beperk is tot die ontwerp van relatief eenvoudige irisse.

Hierdie proefskrif bied drie nuwe rekenaargesteunde ontwerpsprosedures vir die doeltreffende ontwerp van verskillende klasse irisse in multi-modale golfgeleier resoneerder filters. Die nuwe metodes word getoets aan die hand van numeriese voorbeelde, en/of gemete resultate.

Twee nuwe komplekse multi-modale golfgeleier resoneerder filter toepassings is ontwerp deur gebruik te maak van die nuwe ontwerpsprosedures. Die eerste is 'n nuwe diplekser struktuur met twee vierde-orde Chebyschev filterkanale in drie golfgeleier resoneerders wat elk vier resonante modusse ondersteun. Deur korrekte en akkurate plasing van die irisse word 'n groot verbetering in kanaalisolasie bo 'n bestaande multi-modale diplekser verkry.

Die tweede toepassing is die ontwikkeling van 'n nuwe koppelstruktuur vir die vervanging van die gebruiklike koppel- en aanpassingskroewe. 'n Derde-orde trippel-modus filter, gebaseer op hierdie nuwe struktuur, is ook ontwerp deur van die nuwe ontwerpsalgoritmes gebruik te maak.

Abstract

Keywords: Multi-mode, coupled cavity filter, iris, Computer Aided Design (CAD), diplexer, coupling structure.

Multi-mode coupled cavity filters have been the mainstay of commercial satellite communications systems since their introduction in 1970. Multi-mode filters use more than one resonant mode in a single cavity resonator, thereby reducing the size and weight of the filter. This is especially advantageous for satellite applications where the size and weight of the communications payload must be minimised. The use of more modes also increases the complexity of the filter design.

Iris design plays an integral part in the design of multi-mode coupled cavity filters. Currently, irises are mostly designed using either the small aperture theory derived by Bethe, or a standard numerical technique. A recent study comparing these two techniques shows that approximations made in standard correction factors applied to small aperture theory, can lead to unacceptable errors. While numerical techniques are clearly required for the accurate design of complex irises, the standard numerical technique is only suited to the design of relatively simple iris structures.

This dissertation presents three new CAD procedures for the design of irises in multi-mode coupled cavity devices. The new procedures are verified by numerical examples and measurements.

Two new multi-mode coupled cavity devices were designed and tested using the CAD procedures developed in this work. The first is a new diplexer structure that realises two fourth order Chebyschev filter channels in three quadruple-mode cavities. Through correct placement and accurate design of irises, channel isolation was increased beyond that of existing multi-mode diplexer structures.

The second application is the development of a new coupling structure for the replacement of coupling and tuning screws. A third order triple-mode cavity filter, including this new fixed coupling element, was designed using the CAD procedures developed in this dissertation.

Acknowledgements

Several people contributed to this project in various ways and it would not have been possible without their help. Firstly, I would like to thank my promoter, Prof. Meyer, for insight, help and patience.

I would like to thank Mr. W. Croukamp for many painstaking hours of meticulous machining over a period of three years. Mr. A. Cupido should also be mentioned for the etching of most of the iris components.

To the people sharing the office, Thomas, Chris, Mark and Martinette: thank you for insightful conversations and creative contributions.

Finally I would like to thank my wife, Mariza, for her support and for proofreading this dissertation. You have been my inspiration and I hope that I will be able to return the favour in the near future.

Table of Contents

Chapter 4: Measurement Techniques

Chapter 5: CAD Tools

Chapter 6: CAD Procedures for Iris Design

Chapter 7: Diplexer Design

Chapter 1

Introduction

1.1 HISTORICAL PERSPECTIVE

The history of coupled waveguide cavity filters dates from 1948 with the description and implementation of direct-coupled cavity filters by Fano and Lawson [1]. Their filter consisted of a number of waveguide cavities separated by thin inductive irises as shown in figure 1.1. The theory was based on a low-pass prototype, but the synthesis procedure and implementation was problematic. This first step, though, led to a lot of activity in the field with large contributions made by S. B. Cohn, R. Levy, L. Young and others, establishing sound and versatile synthesis and design techniques. Irises were designed using the small aperture theory derived by Bethe [2] in 1944 and the measured polarisability data presented by Cohn in 1952 [3]. Correction factors for large apertures and finite iris thickness were derived and used for a wide variety of aperture shapes and sizes.

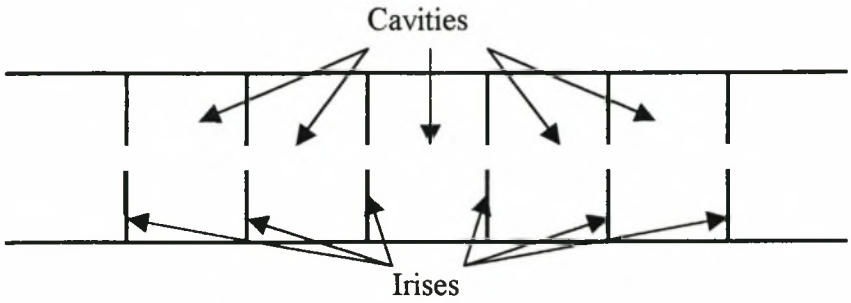

Figure 1.1: Direct-coupled Cavity filter

Waveguide cavities support an infinite number of resonant modes at an infinite number of frequencies. Choosing the dimensions of the cavity carefully can result in resonance of some of these modes at the same frequency. This property of waveguide cavities, whereby degenerate modes can be used to realise more than one resonator in a single cavity, was investigated by Fano and Lawson [1] in 1948. In 1951 Lin [4] also demonstrated a fifth order filter realised in a single cylindrical cavity. At this time prototypes were deemed to be impractical, since the authors could not achieve

independent control of the wanted degenerate modes, as well as suppression of unwanted modes.

This was the state of coupled cavity filter design until the launch of the first commercial satellite communications systems in the late 1960s. New technology calling for reduction in filter size and weight was required, sparking new interest in the use of multi-mode coupled cavity filters. The first dual-mode cavity filter was developed by Atia and Williams [5] at Comsat Laboratories in 1970 and showed that multi-mode cavity filters were indeed commercially viable, and could reduce the number of physical cavities (and thereby the size and weight) of standard coupled cavity filters by a factor of two.

Another significant advantage of multi-mode cavities is that the structure allows coupling to non-adjacent resonators. This can be achieved by using cross-shaped irises or coupling screws. This cross-coupling between resonators results in transfer function zeros along the real or imaginary axis, thereby permitting the realisation of elliptical and linear phase filter functions – the first multiple-coupled waveguide cavity filters. It was therefore possible to improve filter performance without increasing the physical dimensions, at the cost of increased design complexity.

After dual-mode filters, the obvious step towards the design of triple-mode filters was taken. A number of filter structures employing various resonant modes and realising a variety of filter functions were presented [6, 7] between 1971 and 1989. For an elliptical triple-mode filter, three inter-cavity coupling coefficients must be controlled uniquely and simultaneously by an iris containing more than one aperture. With the introduction of quadruple-mode filters [8] in 1987 the number of required couplings increased to four. While it was still possible to design such irises with small aperture theory, some inherent limitations leading to inaccuracies made this task very difficult.

At about the same time interest in numerical electromagnetic (EM) techniques was starting to bloom. From 1985 onward a large number of contributions investigating the EM-analysis of various iris scattering problems can be observed, including techniques such as the Finite Elements Method (FEM) [9], Method of Moments (MOM) [10], Finite Difference Time Domain (FDTD) [11] and the Mode-Matching Method (MM) in various forms and hybridisations [12, 13, 14, 15]. The latter method has proven to be very efficient in analysing waveguide discontinuities, especially

when the guide modal fields are known analytically. It is therefore not surprising that the first EM-evaluation of a coupled cavity structure coupling coefficient was presented in 1991 using the mode-matching technique [16]. A study by Yao [17] in 1994 compared the accuracy of coupling coefficients determined by small aperture theory and the mode-matching method. Even for simple geometries where only one coupling mode is evaluated, errors of up to 10% on the part of the small aperture theory was found, clearly illustrating the importance of numerical methods in iris design.

Today, most designers follow a two-step procedure to design coupled cavity filters. In the first stage, the iris dimensions are determined by using either small aperture theory, or by calculating the two natural resonant frequencies of each mode coupled by the iris numerically. In the second stage, the full filter is optimised with a numerical code.

While the mode-matching method has been used extensively for determining the natural resonant frequencies in coupled cavity filter design, some problems can be identified. Firstly, very little information on how these resonant frequencies are determined and identified in a multi-mode environment is available. It is well known that the mode-matching technique is used to determine the Generalised Scattering Matrix of the coupled cavity structure and that the natural resonant frequencies are calculated by finding the roots of the characteristic equation $\Re(f) = \det[\mathbf{S}_{GSM} + \mathbf{I}]$. In a multi-mode environment, though, a large number of roots must be found, some of which are in very close proximity. This would generally require an impractical number of frequency point evaluations to resolve. Once the problem of determining the roots has been overcome, each root must be linked to a specific propagating mode in order to calculate the coupling coefficient.

A second problem of the standard technique demonstrated in this thesis, is that the method is invalid when cross-coupling between propagating modes in the cavities occurs. This means that this technique is limited to the design of relatively simple irises. All irises without both E- and H-plane symmetries, such as single off-centred irises, are immediately disqualified. It is therefore impossible to design a large number of irises used in multi-mode cavity filters and diplexers [18, 19].

1.2 EFFICIENT INTEGRATED CAD PROCEDURES

This dissertation presents CAD-based iris design procedures for multi-mode coupled cavity devices. Three distinct CAD procedures, each aimed at a specific class of iris design problem, have been developed. The procedures are fast, accurate and capable of designing a very wide range of irises for coupling between synchronously and asynchronously tuned identical and non-identical cavity resonators. Iris structures include centred and off-centred, single, symmetrical and asymmetrical multiple aperture irises. Each of the methods is illustrated through either numerical or measured examples. While the implementation in this thesis is for cylindrical cavities and rectangular irises, the design procedures are not limited to these geometries.

The first CAD procedure is an efficient enhancement of the standard numerical technique, whereby the natural resonant frequencies of a coupled cavity structure is used to determine the iris coupling coefficients [20]. This procedure can be used for the design of irises where no cross-coupling between propagating modes occurs. The problems with the standard analysis technique outlined in the previous section are overcome in the following ways:

- An adaptive sampling algorithm is used to construct a rational interpolation model of the characteristic function from a minimum number of EM-evaluations. Typically, not more than 25 EM-evaluations were found to be sufficient to describe the function accurately to within 0.1%.
- The natural resonant frequencies of the coupled cavity structure are given by the roots of the characteristic equation, some of which are very closely placed for multi-mode applications. Using the characteristic equation directly results in a challenging and time-consuming problem. Since rational interpolation describes the characteristic equation as a ratio of two polynomials, finding the roots of this equation is reduced to the trivial problem of determining the roots of the numerator polynomial.
- In order to determine the coupling coefficients, the natural resonant frequencies (roots of the characteristic equation) must be linked to specific propagating modes in the cavities. A technique for doing this is presented.

- It is shown that the isolation of specific propagating modes in the Generalised Scattering Matrix (GSM) representation of the coupled cavity structure leads to a reduction in the complexity of the characteristic equation and a considerable reduction in the number of EM-evaluations required for coupling coefficient calculation. From this reduced characteristic equation, the resonant frequency of the coupled system can also be extracted directly.
- The Aggressive Space Mapping (ASM) routine, where EM-analysis is used in conjunction with small aperture theory, is applied to establish an efficient CAD procedure for the design of multi-mode irises where no cross-coupling between propagating modes exists.

The second CAD procedure was developed for the design of irises where cross-coupling between propagating modes exists, and the resonant frequencies of the modes are in close proximity. The procedure makes use of optimisation of the complete equivalent circuit model of the coupled cavity structure to fit the transmission and reflection response of the physical structure found from a mode-matching EM-analysis. The use of the Adaptive Sampling algorithm minimises the number of EM-evaluations required for the structure analysis. Since the parameter extraction method is often non-unique, the direct coupling coefficients are iteratively updated to match those found from an equivalent reactance description of the iris. This process ensures that the coefficients of cross-coupling are extracted accurately. The design procedure is applied to an off-centred iris separating two identical cavities supporting degenerate TE_{113}-cos, TE_{113}-sin and TM_{012} modes, resolving all coupling coefficients and resonator frequencies.

A third CAD procedure, based on a measurement method that determines coupling coefficients and resonator frequencies from the phase of the reflection coefficient, was developed for design of irises separating non-identical or asynchronously tuned cavities. This procedure can also be used when cross-coupling occurs between modes that are resonant at different frequencies, for example cross-coupling between components of different filter channels in a diplexer. The Adaptive Sampling algorithm is again applied to minimise the number of frequency point evaluations. Optimisation of iris structures is performed by Aggressive Space Mapping. In order to show the feasibility of this procedure, a diplexer realising two fourth order filter channels in three quadruple-mode cavities is presented. The main aim of this

prototype is the improvement of channel isolation, caused by cross-coupling between components of the two filter channels, by correct placement and accurate design of input/output and coupling irises. Cavity dimensions allow the propagation of the first eight cylindrical modes and off-centred iris coupling between non-identical cavity resonators is required. Design and measurement of this diplexer clearly demonstrates the abilities of this CAD procedure in a multi-mode environment.

1.3 NEW COUPLING ELEMENT

The investigation of the off-centred iris problem led to the development of a new coupling element for use in multi-mode waveguide cavity filters. This coupling element is basically a shorted rectangular waveguide stub placed in the end-walls of the cavity. The magnetic fields of the cavity modes are perturbed to achieve coupling that can be controlled by the position, the cross-sectional dimensions and the depth of the stub. Some of the advantages of coupling by this means are:

- The structure is basically a shorted iris structure and can therefore be analysed and designed by the efficient CAD procedures mentioned above.
- The coupling element is placed in the cavity end-walls and does not protrude into the cavity. The power-handling capability of the filter is increased, because no sharp metallic edges are located in the cavity body.
- In addition to replacement of coupling screws, the number of tuning screws can also be reduced by controlling the resonant frequencies with the coupling element and cavity dimensions.

The application of the new coupling element is demonstrated by the design of a third order triple-mode cavity filter without tuning or coupling screws. The coupling elements are designed using the phase of reflection coefficient CAD procedure mentioned above and measurements agree well with numerical predictions.

1.4 ORIGINAL CONTRIBUTIONS

The original contributions in this dissertation can be summarised as follows:

- Efficient CAD procedures for the design of irises separating non-identical or asynchronously tuned cavities, in the presence of cross-coupling to modes inside or outside the frequency band of interest [20].
- The development of a quadruple-mode diplexer showing greatly improved channel isolation over existing prototypes.
- The development of a new coupling element for the replacement of coupling screws and reduction of tuning screws in multi-mode coupled cavity filters.
- Application of an Adaptive Sampling algorithm with Rational Interpolation to the problem of resolving the natural resonant frequencies of coupled cavity structures.
- Simplifying analysis of coupled cavity structures by reduction of entries in the Generalised Scattering Matrix description.

1.5 LAYOUT OF THE THESIS

For the sake of completeness, the dissertation starts with a detailed discussion of the standard synthesis theory for multiple-coupled cavity filters, namely the synthesis procedures. These procedures relate transfer functions to equivalent circuits that can be used in the design of coupled cavity filters.

This is followed in chapter 3 by an exposition of classical coupled cavity filter design, where a mixture of analytical and empirical data is used to convert equivalent circuit descriptions to high performance physical filter structures. Topics include microwave cavity design, the use of small aperture theory for input/output and inter-cavity iris design, and an example of a manufactured sixth order dual-mode pseudo-elliptical filter is presented.

Chapter 4 gives an overview of measurement techniques used to find the resonant frequencies of, and the coupling coefficients between resonators. Two of these techniques, the phase of reflection coefficient technique and the direct optimisation of an equivalent circuit method are shown to be well suited to use in EM-analysis and design.

This concludes a substantial discussion of the standard theory and techniques as available in literature. Such an in-depth examination of theoretical and experimental methods is essential for a number of reasons:

- It is not available as a whole in literature
- Since the new CAD techniques presented in this thesis follow directly from standard techniques, these must be understood fully.
- A large part of the original contribution of this work is the integration of a wide variety of analysis and design techniques into efficient CAD procedures for specific classes of iris design problems.

Chapter 5 is a short chapter dealing with the implementation of the tools used in the EM-analysis and design procedures. The first subsection introduces the specific formulation of the Mode-Matching routine used in this work, while the remainder presents the implementations of the Adaptive Sampling Algorithm and the Aggressive Space Mapping routine.

The classical design theory, measurement techniques and numerical tools are brought together in chapter 6 to culminate in the development of efficient CAD procedures for iris design in a multi-mode waveguide environment. These CAD procedures are applied to, and verified by, two design examples in chapters 7 and 8.

In chapter 7 the design of a diplexer realised in three quadruple-mode cavities clearly demonstrates the effectiveness of the CAD procedures developed in chapter 6 by producing input/output irises and inter-cavity coupling irises between identical and non-identical cavities.

Chapter 8 describes the use of the new coupling element in a third order triple-mode filter without coupling or tuning screws and chapter 9 concludes the thesis.

Chapter 2

Basic Theory of Synthesis for Narrow-Band Coupled Resonator Filters

2.1 INTRODUCTION

An equivalent circuit of a multiple-coupled cavity filter, where the coupling between synchronously tuned resonators is controlled by mutual inductances, can be seen in figure 2.1. Atia and Williams first published a general synthesis technique for symmetrical filters in 1972. Since then contributions by especially Rhodes, Cameron and Pfitzenmaier have extended the theory to include synthesis techniques for both symmetrical and asymmetrical realisations of filter functions such as:

- Filters of even and odd degree
- Prescribed transmission and/or group-delay equalisation zeros
- Asymmetric or symmetric frequency responses
- Singly or doubly terminated networks

Most of the techniques follow the same path of obtaining a general coupling matrix, which includes the maximum number of inter-resonator couplings required by the transfer function. This technique has remained mostly unchanged since the original work by Atia and Williams [21] and is presented in section 2.

Once found, the general coupling matrix can be manipulated mathematically to minimise the number of couplings required and to better suit different filter topologies. Some special cases of such rotation transforms are covered in section 3.

The crux of the general synthesis procedure relates the coupling matrix to the short-circuit admittance parameters of the network. The Darlington synthesis method is used to obtain the admittance parameters from a given voltage transfer ratio. For symmetrical in-line prototype networks, Rhodes developed a simpler and more direct synthesis procedure using only the even-mode representation of the equivalent circuit.

Section 4 deals with the use, and the conditions for use, of the Darlington and Rhodes synthesis methods.

Section 5 examines the use of coupling matrix optimisation routines for the direct synthesis of the equivalent circuit parameters of multiple-coupled cavity filters. Finally, some examples of the use of the various synthesis procedures are given in section 6.

2.2 EQUIVALENT CIRCUIT AND FUNDAMENTAL DEFINITIONS

The general equivalent circuit of n identically tuned, coupled cavities is presented in figure 2.1. Each cavity is tuned to a resonant frequency of $\omega_0 = \frac{1}{\sqrt{LC}} = 1\text{rad/s}$ and the resonator impedance is $Z = \sqrt{\frac{L}{C}} = 1\Omega$ throughout.

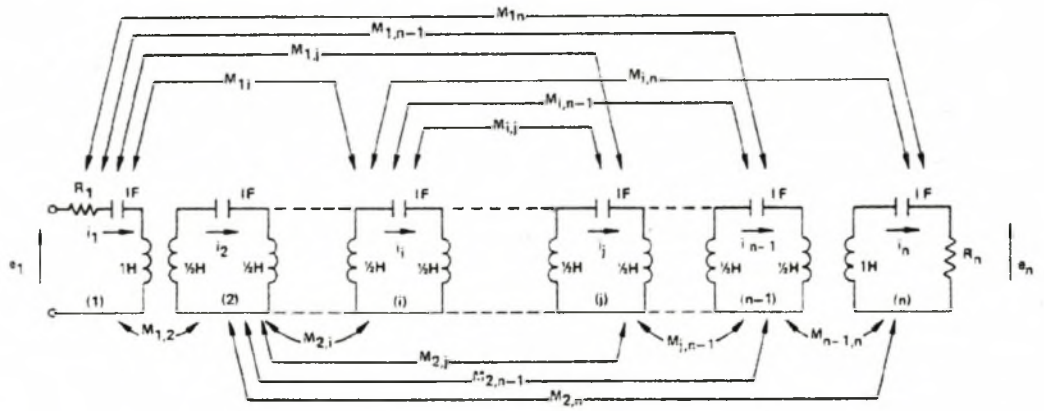

Figure 2.1: General 2-port composed of tuned coupled cavities [22].

The loop equations for the network, assuming a narrow bandwidth, can be written as:

$$\mathbf{E} = \mathbf{Z} \cdot \mathbf{I} \tag{2.1a}$$

$$\begin{bmatrix} e_1 \\ 0 \\ 0 \\ 0 \\ . \\ . \\ . \\ e_n \end{bmatrix} = \begin{bmatrix} S+R_1 & jM_{12} & jM_{13} & . & . & . & jM_{1n} \\ jM_{12} & S & jM_{23} & . & . & . & . \\ jM_{13} & jM_{23} & S & . & . & . & . \\ . & . & . & . & . & . & . \\ . & . & . & . & . & . & . \\ . & . & . & . & . & . & . \\ . & . & . & . & . & S & jM_{n-1,n} \\ jM_{1n} & . & . & . & . & jM_{n-1,n} & S+R_n \end{bmatrix} \cdot \begin{bmatrix} i_1 \\ i_2 \\ i_3 \\ . \\ . \\ . \\ i_{n-1} \\ i_n \end{bmatrix} \quad (2.1b)$$

Where the bandpass variable $S = j\left(\omega - \frac{1}{\omega}\right)$, and the narrow-band approximation $jM_{ij} \approx j\omega M_{ij} \approx j\omega_0 M_{ij}$, $\omega_0 = 1$rad/s, can be made.

The impedance matrix can be expressed as:

$$\mathbf{Z} = (\mathbf{SI} + \mathbf{M_R}) \quad (2.2)$$

Where $\mathbf{I}$ = identity matrix and,

$$\mathbf{M_R} = \mathbf{R} + \mathbf{jM} \quad (2.3)$$

The matrix $\mathbf{R}$ has all zero entries except for the (1,1) and (n,n) elements, which are R_1 and R_n respectively. The voltage transfer function for the doubly terminated circuit in figure 2.1 can be expressed as:

$$|t(j\omega)|^2 = \frac{4R_1}{R_n}\left|\frac{e_n(j\omega)}{e_1(j\omega)}\right|^2 \quad \text{where } e_n = i_n R_n \quad (2.4)$$

and

$$i_n = e_1 \frac{|cofactor Z_{1n}|}{|\mathbf{Z}|} \quad (2.5)$$

The general synthesis of bandpass filters in multiple-coupled waveguide cavities is most conveniently done by assuming symmetrical networks [22]. This means that $R_1 = R_n = R$ and $M_{ij} = M_{ji}$, and the M-matrix is symmetrical about the anti-diagonal. Equation (2.4) therefore simplifies to

$$|t(j\omega)| = 2\left|\frac{e_n(j\omega)}{e_1(j\omega)}\right| \quad (2.6)$$

The M-Matrix is also referred to as the coupling matrix and contains all the coupling information of the multiple-coupled cavity filter. A synthesis technique must be able to extract the coupling matrix and the 2-port network terminations R_1 and R_n.

2.2.1 COUPLING MATRIX SYNTHESIS

An equivalent two-port circuit, in terms of admittance-parameters with the ideal transformers included, is given in figure 2.2. The rest of the theory follows the procedure set forth in [6] and [23]. The two-port short-circuit admittance-parameters relating to figure 2.2(b) are:

$$\begin{bmatrix} i_1 \\ i_n \end{bmatrix} = \begin{bmatrix} y_{11} & y_{12} \\ y_{21} & y_{22} \end{bmatrix} \cdot \begin{bmatrix} e_1 \\ e_n \end{bmatrix} \tag{2.7}$$

of which $y_{21} = y_{12}$ (reciprocal network)

These parameters are scaled through the ideal transformers to find the inner network of figure 2.1.

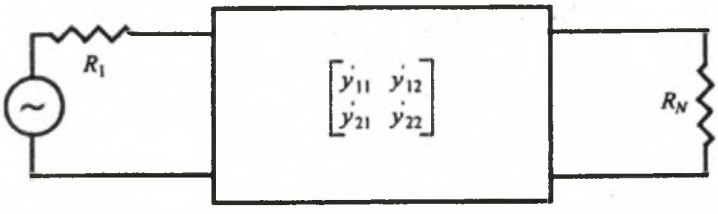

(a)

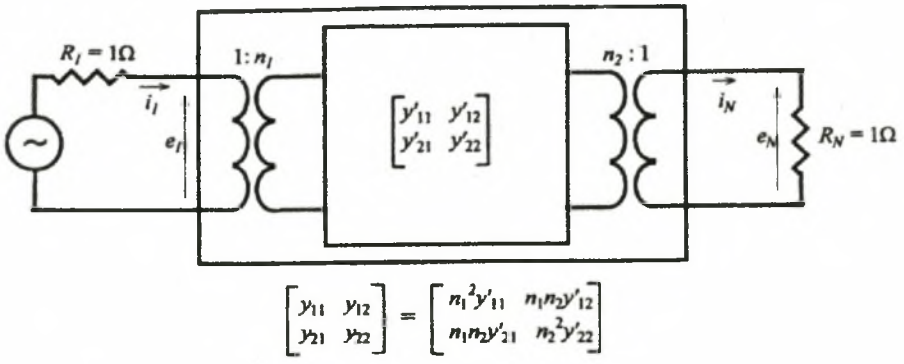

(b)

Figure 2.2(a) and (b): Short-circuit admittance-parameters of equivalent circuit [23].

$$\begin{bmatrix} i_1 \\ i_n \end{bmatrix} = \begin{bmatrix} n_1^2 y'_{11} & n_1 n_2 y'_{12} \\ n_1 n_2 y'_{21} & n_2^2 y'_{22} \end{bmatrix} \cdot \begin{bmatrix} e_1 \\ e_n \end{bmatrix} \tag{2.8}$$

With reference to equation (2.2) $y_{21}(s)$ and $y_{22}(s)$ can be determined by setting $R = 0$

$$y_{21}(s) = \left.\frac{i_n}{e_1}\right|_{R=0} = j\left[-\mathbf{M} - \omega\mathbf{I}\right]^{-1}_{n1}$$
$$y_{22}(s) = \left.\frac{i_n}{e_n}\right|_{R=0} = j\left[-\mathbf{M} - \omega\mathbf{I}\right]^{-1}_{nn} \tag{2.9}$$

Equations (2.9) are the crux of the synthesis, as it is through these two equations that the physical network consisting of coupled cavities, is mathematically related to the transfer function.

Since **M** is real and symmetric about its principal diagonal, all of its eigenvalues are real. Therefore an n x n matrix **T,** consisting of rows of orthogonal unit vectors, exists which satisfies the following equation:

$$-\mathbf{M} = \mathbf{T} \cdot \mathbf{\Lambda} \cdot \mathbf{T}^t \tag{2.10}$$

where $\mathbf{\Lambda}$=diag[λ_1, λ_2, λ_3, ... , λ_n], λ_i are the eigenvalues of $-\mathbf{M}$, and $\mathbf{T} \cdot \mathbf{T}^t = \mathbf{I}$. Substituting (2.10) into (2.9) gives:

$$y_{21}(s) = j\left[\mathbf{T} \cdot \Lambda \cdot \mathbf{T}^t - \omega\mathbf{I}\right]^{-1}_{n1}$$
$$y_{22}(s) = j\left[\mathbf{T} \cdot \Lambda \cdot \mathbf{T}^t - \omega\mathbf{I}\right]^{-1}_{nn} \tag{2.11}$$

The general solution for an element i, j of the RHS of (2.11) is:

$$\left[\mathbf{T} \cdot \Lambda \cdot \mathbf{T}^t - \omega\mathbf{I}\right]^{-1}_{ij} = \sum_{k=1}^{n} \frac{T_{ik}T_{jk}}{\omega - \lambda_k}, \qquad i, j = 1, 2, 3, \ldots, \text{n}$$

Therefore, (2.11) becomes

$$y_{21}(s) = j\sum_{k=1}^{n} \frac{K_{21}}{\omega - \lambda_k} = j\sum_{k=1}^{n} \frac{T_{nk}T_{1k}}{\omega - \lambda_k}, \text{ and}$$
$$y_{22}(s) = j\sum_{k=1}^{n} \frac{K_{22}}{\omega - \lambda_k} = j\sum_{k=1}^{n} \frac{T^2{}_{nk}}{\omega - \lambda_k} \tag{2.12}$$

Atia and Williams [21] supply some sufficient conditions that the rational 2x2 matrix found in (2.7) is the desired admittance matrix of the 2-port in figure 2.1. These are:

- The poles λ_k are purely imaginary and satisfy:

$$\sum_{k=1}^{n} \lambda_k = 0; \tag{2.13a}$$

- The residues of the partial fraction expansions (K_{22} and K_{21}) in (2.12) are real;

- $$\sum_{k=1}^{n} \lambda_k K_{22} = 0 \quad \text{and} \quad \sum_{k=1}^{n} K_{21} = 0 \tag{2.13b}$$

From (2.12) it is clear that a partial fraction expansion of $y_{21}(s)$ and $y_{22}(s)$ yields both the first and last rows of the **T**-matrix and the eigenvalues λ_k of the **M**-matrix:

$$T_{nk} = \sqrt{K_{22k}}$$

$$T_{1k} = \frac{K_{21k}}{T_{nk}} = \frac{K_{21k}}{\sqrt{K_{22k}}}, \qquad k = 1, 2, 3, \ldots, \text{n} \tag{2.14}$$

The transformer turn ratios are determined to scale the row vectors to unity (the row vectors of **T** must be unit vectors), and to yield the 'inner' network of figure 2.2:

$$n_1^2 = R_1 = \sum_{k=1}^{n} T_{1k}^2, \qquad n_2^2 = R_n = \sum_{k=1}^{n} T_{nk}^2 \tag{2.15}$$

$$\text{Then,} \quad T'_{1k} = \frac{T_{1k}}{n_1} \quad \text{and} \quad T'_{nk} = \frac{T_{nk}}{n_2} \tag{2.16}$$

At this stage it should be noted that abs(T'_1)= T_n. The remaining rows of **T** can be constructed by using an orthonormalisation process such as the Gram-Schmidt process. This process is detailed in Appendix A.

2.2.2 USE OF THE EVEN- AND ODD- MODES

As mentioned earlier, the coupled cavity network is assumed to be electrically symmetrical. When working with symmetrical networks, it is advantageous to use the related even- and odd-mode representations of the network, as the **M**-matrix is reduced in size, thereby improving computation speed and accuracy [22]. This new matrix $\mathbf{M}_e$ corresponds to the excitation of the unterminated network by two identical zero impedance voltage sources applied at both ports, as shown in figure 2.3. The odd mode matrix can also be found and utilised, though it is more customary to use the even mode matrix.

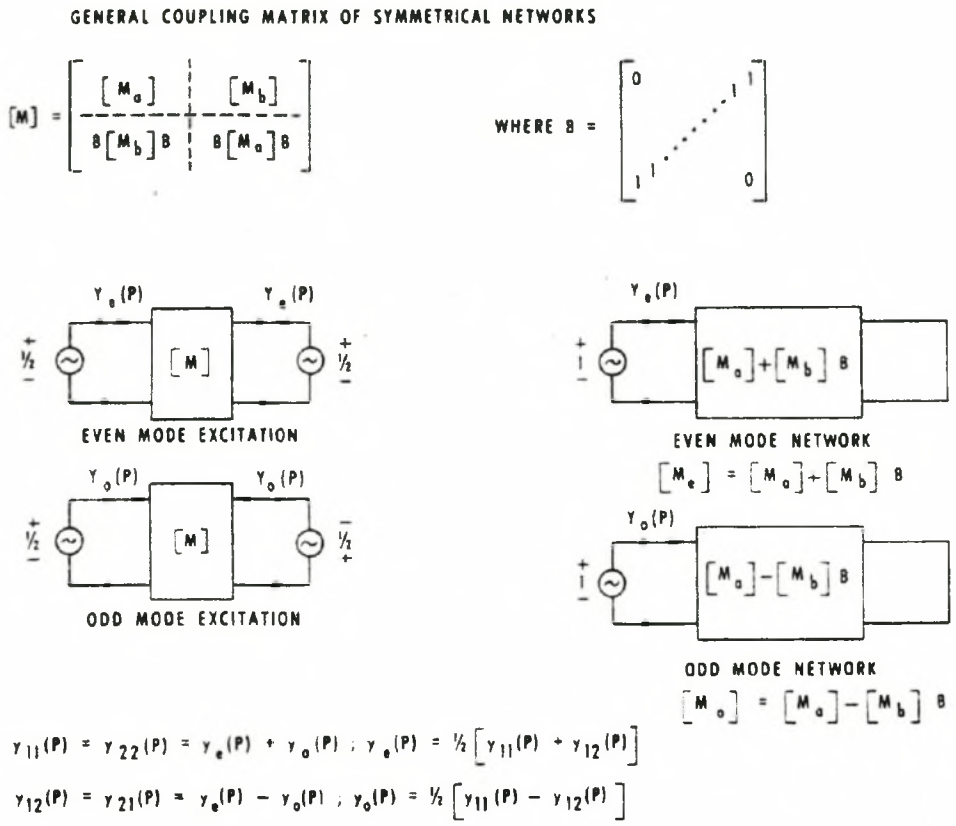

Figure 2.3: Even- and odd-mode coupling matrices for a symmetrical network [21].

The *n/2* by *n/2* $\mathbf{M}_e$-matrix can be found from the full *n* x *n* **M**-matrix by folding it along the centre line of the rows and the columns and is shown in equations (2.17) and (2.18) [22]. This is possible, as for symmetrical networks $M_{ij} = 0$ if $i+j$ is an **even** number [24].

$$\mathbf{M} = \begin{bmatrix} 0 & M_{12} & 0 & M_{14} & 0 & M_{16} & \cdot & \cdot & \cdot & M_{1,n} \\ M_{12} & 0 & M_{23} & 0 & \cdot & \cdot & \cdot & \cdot & \cdot & \cdot \\ 0 & M_{23} & 0 & M_{34} & \cdot & \cdot & \cdot & \cdot & \cdot & \cdot \\ M_{14} & 0 & M_{34} & \cdot & \cdot & \cdot & \cdot & \cdot & \cdot & \cdot \\ 0 & \cdot & \cdot & \cdot & \cdot & \cdot & \cdot & \cdot & \cdot & \cdot \\ M_{16} & \cdot & \cdot & \cdot & \cdot & \cdot & \cdot & \cdot & \cdot & \cdot \\ \cdot & \cdot & \cdot & \cdot & \cdot & \cdot & \cdot & \cdot & \cdot & \cdot \\ \cdot & \cdot & \cdot & \cdot & \cdot & \cdot & \cdot & \cdot & \cdot & \cdot \\ \cdot & \cdot & \cdot & \cdot & \cdot & \cdot & \cdot & \cdot & 0 & M_{n-1,n} \\ M_{1,n} & \cdot & \cdot & \cdot & \cdot & \cdot & \cdot & 0 & M_{n-1,n} & 0 \end{bmatrix} \qquad (2.17)$$

$$\mathbf{M}_e = \begin{bmatrix} M_{1,n} & M_{12} & M_{1,n-2} & M_{14} & M_{1,n-4} & \cdots & M_{1,n/2} \\ M_{12} & M_{2,n-1} & M_{23} & \cdot & \cdot & \cdots & \cdot \\ M_{1,n-2} & M_{23} & M_{3,n-2} & \cdot & \cdot & \cdots & \cdot \\ \cdot & \cdot & \cdot & \cdot & \cdot & \cdots & \cdot \\ \cdot & \cdot & \cdot & \cdot & \cdot & \cdots & \cdot \\ \cdot & \cdot & \cdot & \cdot & \cdot & \cdots & \cdot \\ \cdot & \cdot & \cdot & \cdot & \cdot & \cdots & \cdot \\ \cdot & \cdot & \cdot & \cdot & \cdot & \cdots & \cdot \\ \cdot & \cdot & \cdot & \cdot & \cdot & \cdots & \cdot \\ M_{1,n/2} & \cdot & \cdot & \cdot & \cdot & \cdots & M_{n/2,(n/2)+1} \end{bmatrix} \tag{2.18}$$

From figure 2.3 it is clear that for symmetrical networks, the even-mode short-circuit driving admittance is:

$$2Y_e = y_{21} + y_{22}, \tag{2.19a}$$

and as to the residues of y_{21} and y_{22}:

$$\sum_{k=1}^{n} \frac{C|K_{21}|}{\omega - \lambda_k} = \sum_{k=1}^{n} \frac{|K_{22}|}{\omega - \lambda_k}, \text{ where } C \text{ is some constant.} \tag{2.19b}$$

Equations (2.9) to (2.12) can now be rewritten to include the use of $\mathbf{M}_e$, Y_e and a new transformation matrix $\mathbf{T}_e$.

$$Y_e(s) = j\left[-\mathbf{M}_e - \omega\mathbf{I}\right]^{-1} \tag{2.20}$$

$$-\mathbf{M}_e = \mathbf{T}_e \cdot \Lambda \cdot \mathbf{T}_e^t \tag{2.21}$$

$$Y_e(s) = \sum_{k=1}^{n} \frac{K_e}{\omega - \lambda_k} = \sum_{k=1}^{n} \frac{T_{e1}}{\omega - \lambda_k} \tag{2.22}$$

The normalised residues of Y_e now form the first row of the new *n/2* by *n/2* $\mathbf{T}_e$-matrix and is related to the *n* values of the first and last rows of the full **T**-matrix by:

$$T_{e1} = \sqrt{2}T_{1k} = \sqrt{2}T_{nk} \tag{2.23}$$

The rest of the rows are found by an orthonormalisation process such as the Gram-Schmidt process.

2.3 REDUCTION OF THE M-MATRIX

In general, all the elements of the **M**-matrix are non-zero, implying that all the possible couplings are present. Non-zero elements on the main diagonal represent resonator offset frequencies, as can be found in electrically asymmetric networks and asynchronously tuned filters. In many cases, all these couplings are not practically realisable given the desired topology of the filter. A lot of activity in this area has produced practical coupling matrices for symmetrical and asymmetrical dual-mode inline prototype networks [25, 26, 27], asymmetrical canonical filters [24], and linear phase filters [28]. Minimising the number of physical couplings can also reduce the complexity of the final filter. It is therefore necessary to find a way to transform the full coupling matrix into a realisable form by reducing unwanted entries to zero while preserving the eigenvalues and eigenvectors of the coupling matrix.

While several practical forms of the coupling matrix can be found, the method for establishing such forms is of interest. Cameron [23] presents a method to achieve forms known as the 'folded canonical' and the 'right-column justified' forms. A similarity transform on the n x n **M**-matrix is carried out by pre- and post-multiplying it by an n x n rotation matrix **R** and its transpose $\mathbf{R}^t$:

$$\mathbf{M}_r = \mathbf{R}_r \cdot \mathbf{M}_{r-1} \cdot \mathbf{R}_r^t, \qquad r = 1, 2, 3, \ldots, k \tag{2.24}$$

where k is the number of transformations required to reduce all unwanted elements to zero. Choosing the element $[i,j]$ $(i \neq j)$ as pivot element of **R**, implies that elements $R_{ii} = R_{jj} = cos\theta_r$, $R_{ij} = -R_{ji} = sin\theta_r$, $(i, j \neq 1 \text{ or } n)$, and θ_r is the angle of rotation illustrated in table 2.1[23]:

Table 2.1
Example of 7th degree Rotation Matrix $\mathbf{R}_r$ pivot [3,5]

	1	2	3	4	5	6	7
1	1						
2		1					
3			c_r		$-s_r$		
4				1			
5			s_r		c_r		
6						1	
7							1

$c_r = \cos\theta_r$, $s_r = \sin\theta_r$

The similarity transform applied to the coupling matrix $\mathbf{M}_{r-1}$, will change the elements in rows i and j and the columns i and j. The k^{th} element in row or column i or j (but not for $k = i,j$), will change in value according to the following formula:

$$\begin{aligned} M'_{ik} &= c_r M_{ik} - s_r M_{jk}, && \text{for an element in row } i \\ M'_{jk} &= s_r M_{ik} + c_r M_{jk}, && \text{for an element in row } j \\ M'_{ki} &= c_r M_{ki} - s_r M_{kj}, && \text{for an element in column } i \\ M'_{kj} &= s_r M_{ki} + c_r M_{kj}, && \text{for an element in column } j \end{aligned} \tag{2.25}$$

where $k(\neq i, j) = 1, 2, 3, \ldots, n$, and the unprimed elements belong to $\mathbf{M}_{r-1}$ and the primed elements to $\mathbf{M}_r$.

Two important properties of this transformation can be noted:

- Only the elements in the rows and columns i and j of the pivot $[i,j]$ are influenced by the transformation.
- If two elements facing each other across the rows and columns of the pivot are zero before the transformation, they will remain zero after the transformation.

This means that a routine procedure can be followed to reduce unwanted elements to zero while leaving required elements untouched. This procedure transforms the **M**-matrix into its 'folded canonical' form and starts by reducing unwanted elements in the first row, then the n-th column, the second row, the n-1-th column and so forth until all unwanted elements are zero. Table 2.2 summarises this procedure for a 7x7 coupling matrix [23].

Table 2.2: Example of Reduction of M-Matrix to Folded Canonical Form

Unwanted Element	Row/ Column	Pivot $[i,j]$	$\theta_r = \tan^{-1}(cM_{kl} / M_{mn})$				
			k	l	m	n	c
M_{16}	Row 1	[5,6]	1	6	1	5	-1
M_{15}	Row 1	[4,5]	1	5	1	4	-1
M_{14}	Row 1	[3,4]	1	4	1	3	-1
M_{13}	Row 1	[2,3]	1	3	1	2	-1
M_{37}	Column 7	[3,4]	3	7	4	7	1
M_{47}	Column 7	[4,5]	4	7	5	7	1
M_{57}	Column 7	[5,6]	5	7	6	7	1
M_{25}	Row 2	[4,5]	2	5	2	4	-1
M_{24}	Row 2	[3,4]	2	4	2	3	-1
M_{46}	Column 6	[4,5]	4	6	5	6	1

This method is only unconditionally valid for transformation of full coupling matrices and not even-mode matrices. For even-mode matrices it is often necessary to reduce elements on the main diagonal, which cannot be handled by this method. For this kind of transformation a similar, but different, reduction formula is derived for each individual case. An example of a third order even-mode matrix, where M_{22} must be reduced, is [25]:

$$\begin{bmatrix} M_{11} & M_{12} & M_{13} \\ M_{12} & M_{22} & M_{23} \\ M_{13} & M_{23} & M_{33} \end{bmatrix} \rightarrow \begin{bmatrix} M'_{11} & M'_{12} & M'_{13} \\ M'_{12} & 0 & M'_{23} \\ M'_{13} & M'_{23} & M'_{33} \end{bmatrix}$$

The rotation matrix required here is of the same form of that above with the pivot [2,3].

$$\mathbf{R} = \begin{bmatrix} 1 & 0 & 0 \\ 0 & c_1 & -s_1 \\ 0 & s_1 & c_1 \end{bmatrix} \tag{2.26}$$

After the transformation, the following changes to the elements of the coupling matrix are observed:

$$\begin{aligned} M'_{12} &= c_1 M_{12} - s_1 M_{13}, \quad M'_{13} = s_1 M_{12} + c_1 M_{13} \\ M'_{22} &= c_1^2 M_{22} - 2c_1 s_1 M_{23} + s_1^2 M_{33} \\ M'_{23} &= c_1 s_1 M_{22} - s_1^2 M_{23} + c_1^2 M_{23} - c_1 s_1 M_{33} \\ M'_{33} &= s_1^2 M_{22} + 2c_1 s_1 M_{23} + c_1^2 M_{33} \end{aligned} \tag{2.27}$$

To reduce M_{22} to zero the following must hold:

$$M_{33} t^2 - 2M_{23} t + M_{22} = 0 \tag{2.28}$$

where $t = \tan\theta_1$ and θ_1 is the angle required to determine s_1 and c_1

Solving for t gives the two possible solutions:

$$t = \frac{M_{23} \pm \sqrt{M_{23}^2 - M_{22} M_{33}}}{M_{33}} \tag{2.29}$$

An extra realisability condition requires that $M_{23}^2 \geq M_{22} M_{33}$

Substituting the value of t back into the equation results in the final values of the coupling matrix $\mathbf{M}_1$. Although the method used here is similar to that of the full

coupling matrix, the values of the elements in rows i and j of the pivot $[i,j]$ differ from those presented for the full coupling matrix, and elements on the main diagonal can be reduced.

2.4 FINDING THE ADMITTANCE PARAMETERS FROM THE VOLTAGE TRANSFER RATIO $S_{21}(s)$

The synthesis of most filter functions starts with the determination of a voltage transfer ratio with the required pass-band and stop-band response. In this case, a low-pass prototype voltage transfer function will be used. In order to ensure the realisability of this function as the doubly terminated network of figure 2.1, some realisability conditions must be met:

For $$S_{21}(s) = \frac{M(s)}{N(s)}$$

a) M and N are real polynomials and N is strictly Hurwitz (zeros in left half plane)

b) Order $M \leq$ (order N) – 2

Condition (b) can immediately be seen from equation (2.5) and ensures that there are at least two zeros at infinity.

The method for determining the admittance parameters used here is known as the Darlington Method, originally presented in [29] and summarised in [30]:

1) From any of the specification functions such as $|V_2/V_1|^2$ together with the values for R_1 and R_2, find the transmission coefficient $S_{21}(s)$.

2) From $S_{21}(s)$ find the reflection coefficient $S_{11}(s)$.

3) From $S_{11}(s)$ together with the value of R_1, find the input impedance $Z_{in}(s)$.

4) From $Z_{in}(s)$ synthesize the required network.

R_1 and R_2 used here are not yet the normalised terminations of figure 2.2.

For a lossless network, $S_{11}(s)$ is related to $S_{21}(s)$ by :

$$S_{11}(s)S_{11}(-s) = 1 - S_{21}(s)S_{21}(-s) \tag{2.30}$$

$$\text{And} \quad S_{11}(s) = \pm \frac{S_{11num}(s)}{S_{11den}(s)} \tag{2.31}$$

The denominator of $S_{11}(s)$ is the same as that of $S_{21}(s)$ and is therefore also Hurwitz. The numerator is not necessarily Hurwitz, and may have zeros in the left and right half planes, but must occur in conjugate pairs, if complex.

$Z_{in}(s)$ can be found from $S_{11}(s)$ from equation (2.32):

$$\frac{Z_{in}(s)}{R_1} = \frac{1 - S_{11}(s)}{1 + S_{11}(s)} \tag{2.32}$$

From (2.31) and (2.32) $Z_{in}(s)$ can have one of two forms

$$Z_{in}(s) = R_1 \frac{S_{11den}(s) \pm S_{11num}(s)}{S_{11den}(s) \mp S_{11num}(s)} = \frac{Z_m(s)}{Z_n(s)} \tag{2.33}$$

depending on the signs chosen for the numerator and denominator of S_{11}. The two networks found this way are dual networks; the impedance of the one is the admittance of the other.

Returning to figure 2.1, the input impedance can be written as:

$$Z_{in}(s) = \frac{z_{11}[1/y_{22} + R_2]}{z_{22} + R_2} \tag{2.34}$$

The $Z_{in}(s)$ found in (2.33) can be written in the same form as that of (2.34) by dividing the numerator and denominator into its even and odd parts, extracting either the even or the odd parts and then multiplying with R_2.

$$Z_{in}(s) = \frac{Z_m^{\ e} + Z_m^{\ o}}{Z_n^{\ e} + Z_n^{\ o}} \tag{2.35}$$

For the **even** order case, the odd parts are taken outside the brackets leaving:

$$Z_{in}(s) = \frac{Z_m^{\ o}}{Z_n^{\ o}} \frac{\left[\frac{R_2 Z_m^{\ e}}{Z_m^{\ o}} + R_2\right]}{\left[\frac{R_2 Z_n^{\ e}}{Z_n^{\ o}} + R_2\right]} \tag{2.36}$$

Comparing (2.34) and (2.36) gives:

$$y_{22}(s) = \frac{1}{R_2}\frac{Z_m^{\,o}}{Z_m^{\,e}} \tag{2.37}$$

The denominator of $y_{21}(s)$ is the same as that of $y_{22}(s)$, and the numerator has the same transmission zeros as $S_{21}(s)$. Therefore:

$$y_{21}(s) = \frac{1}{R_2}\frac{M(s)}{Z_m^{\,e}} \tag{2.38}$$

By taking the even part of $Z_{in}(s)$ out of the brackets in (2.35), for the **odd** order case:

$$y_{22}(s) = \frac{1}{R_2}\frac{Z_m^{\,e}}{Z_m^{\,o}} \qquad \text{and} \qquad y_{21}(s) = \frac{1}{R_2}\frac{M(s)}{Z_m^{\,o}}$$

Equations (2.37) and (2.38) can now be used to find either the full **M**-matrix or Y_e and the even-mode matrix $\mathbf{M}_e$.

This method of finding the admittance parameters is very sensitive to the accuracy of root-finding algorithms when determining $S_{11}(s)$, especially when the desired ripple in the pass-band becomes small. It is therefore desirable to use a transfer function where the reflection zeros are known explicitly, as is used by Atia and Williams in [6, 22]. A much simpler, shorter and direct way to find Y_e is proposed by Rhodes in [25] and [31].

The filter functions mentioned before all have the property that the numerator of the reflection coefficient is either an even or an odd function, therefore they are realisable as symmetrical networks. Using the bisection theorem [30], we can write:

$$S_{21}(s) = \frac{Y_e - Y_o}{(1+Y_e)(1+Y_o)} \tag{2.39}$$

$$\text{Also,} \quad S_{21}(s) = \frac{E(s)}{D_k(s)D_k^{\,*}(s)} \tag{2.40}$$

Where k = (order of the denominator $S_{21}(s)$)/2

and $D^*(s)$ is equal to $D(s)$ with the coefficients replaced by their complex conjugates. From (2.39) and (2.40) it is also clear that $Y_o = Y_e^*$ and the zeros of $D(s)$ are the zeros of Y_o+1. The poles of $S_{21}(s)$ are all in the left half plane (Hurwitz polynomial) and occur in complex conjugate pairs. The choice of roots for $D(s)$ is very important; positive and negative roots must be chosen alternately.

Once the roots of $D_k(s)$ are chosen, $D_k(s)$ can be expanded into the even and odd parts of its real and imaginary parts as follows:

$$D_k(s) = E_1(s) + O_1(s) + \mathrm{j}^*[E_2(s) + O_2(s)] \tag{2.41}$$

$Y_e(s)$ can then easily be found from (2.39) as:

$$Y_e(s) = \frac{E_1(s) + jO_2(s)}{O_1(s) + jE_2(s)} \qquad \text{for } k \text{ even} \tag{2.42a}$$

or

$$Y_e(s) = \frac{O_1(s) + jE_2(s)}{E_1(s) + jO_2(s)} \qquad \text{for } k \text{ odd} \tag{2.42b}$$

This method is very accurate as $Y_e(s)$ is derived directly from $S_{21}(s)$ and there is no need to find the roots of $S_{11}(s)S_{11}(-s)$ as with the Darlington Method.

In all cases described above, the simplest method of finding the normalised termination of the doubly terminated network in figure 2.1 is given by [23]. The denominator of $S_{21}(s)$ is of the form:

$$N(s) = \sum_{k=0}^{n} d_k s^{n-k} \tag{2.43}$$

By an algorithm for the calculation of the inverse of a matrix $(\lambda\mathbf{I} - \mathbf{A})$ presented in [32], and the use of (2.2) and (2.3), one obtains

$$d_0 = 1$$

$$d_1 = -trace(\mathbf{A}) = -trace(-j\mathbf{R} + \mathbf{M}) = j(R_1 + R_n) \tag{2.44}$$

This means that the coefficient of the s^{n-1}-term of the denominator of $S_{21}(s)$ is related to the values of R_1 and R_n. Since a symmetrical network is assumed, $R = R_1 = R_n$ can be found from:

$$R = \frac{coefficient(s^{n-1})}{2} \tag{2.45}$$

Extracting R by this method automatically normalises the impedance levels of the network.

2.5 SYNTHESIS OF COUPLED CAVITY FILTERS BY COUPLING MATRIX OPTIMISATION

While the general synthesis techniques described above can always be used to find a general coupling matrix, the procedure for reducing this matrix to comply with the required filter topology is often cumbersome and sometimes even divergent [33, 27]. This has prompted investigations into the use of direct optimisation of the coupling matrix to fit a desired filter topology. Initially, the objective error function used was the difference between the frequency response of the network and a frequency specification. This approach was found to be inefficient and often resulted in non-optimum solutions [33].

Two methods have been published to overcome this problem. The first method by Atia [33] reconstructs the transfer functions S_{21} and S_{11} from the coupling matrix and minimises the error at the position of the transmission and reflection zeros. The procedure is as follows:

$$S_{21} = \frac{1}{1+\varepsilon^2\Phi^2(\lambda)} \tag{2.46}$$

where $\lambda = (f_o/BW)[f/f_o - f_o/f]$, ε is a scale factor related to the pass-band ripple and

$$\Phi(\lambda) = \frac{\prod_{i=1}^{N}(\lambda - A_i)}{\prod_{j=1}^{M}(\lambda - B_i)} \tag{2.47}$$

with A_i and B_i the reflection and transmission zeros respectively.

The following relations for a lossless two-port network can be found:

$$\begin{aligned} S_{21} &= \frac{-2j\sqrt{R_1R_2}P_{12}}{D + P_0R_1R_2 - j(P_{11}R_1 + P_{22}R_2)} \\ S_{11} &= \frac{D - P_0R_1R_2 + j(P_{11}R_1 + P_{22}R_2)}{D + P_0R_1R_2 - j(P_{11}R_1 + P_{22}R_2)} \end{aligned} \tag{2.48}$$

P_0, P_{11}, P_{12}, P_{22} and D are polynomials that can be related to the coupling matrix **M** by:

$$[\lambda I - M]^{-1}_{11} = \frac{P_{11}}{D} \qquad [\lambda I - M]^{-1}_{12} = \frac{P_{12}}{D}$$
$$[\lambda I - M]^{-1}_{22} = \frac{P_{22}}{D} \qquad P_0 = \frac{P_{12}^2 - P_{11}P_{22}}{D} \tag{2.49}$$

The polynomials are obtained using the Souriau-Frame algorithm [34] for the inverse of a matrix.

Specific topologies can be found by using a matrix **T,** the same size as **M,** as a mask to enforce zero-entries in the coupling matrix. This T-matrix has all entries equal to 1 except where zeros are to be placed in the M-matrix. The error function used is

$$Errf = \sum_{i=1}^{N}\left[S_{11}(A_i)\right]^2 + \sum_{i=1}^{N}\left[S_{21}(B_i)\right]^2 + \left[\varepsilon - \hat{\varepsilon}\right]^2 \tag{2.50}$$

and is minimised by a standard gradient unconstrained search algorithm.

This method converges very quickly and is reported to be independent of the initial coupling matrix guess. It is also very accurate when the positions of the reflection zeros are known explicitly.

The second method by Amari [35] follows very much the same procedure as that of [33], but uses an analytical gradient-based optimisation technique. The initial guess of the coupling matrix does seem to be important here. The best results were obtained with an initial guess containing 0.5 for direct couplings, zero cross-coupling entries, and $R_1 = R_n = 1$.

In both cases the accuracy of the optimisation procedures can be increased even further if the final coupling matrix is used as an initial guess in a full frequency optimisation procedure. The excellent initial guess together with the increased information available results in a better approximation of the desired frequency response.

2.6 EXAMPLES OF MULTIPLE-COUPLED CAVITY FILTER SYNTHESIS

2.6.1 SIXTH ORDER ELLIPTICAL PROTOTYPE FILTER SYNTHESIS

The first step in the design procedure is to select a suitable low-pass prototype filter function. If frequency selectivity and pass-band loss are taken as the significant filtering parameters, then Butterworth and Chebyschev filter functions lag behind filter functions with finite transmission zeros such as Elliptic and Chebyschev Rational Function (with finite transmission zeros) filters [5]. The filter functions used in [22], [21], [5] and [6] are all of the form:

$$|t(s)|^2 = \frac{1}{1+\varepsilon^2(-1)^r s^{2r}\dfrac{\prod_{k=1}^{m}(s^2+z_k{}^2)^2}{\prod_{k=1}^{l}(s^2+p_k{}^2)^2}}, \qquad \text{where } r+2m+1\geq 2l \text{ for realisability}$$

This elliptic filter function does not inherently produce an equiripple response in the pass- or stop-band. The filter function used in the example is of the above form with $r=m=l=2$ and the response shown in figure 2.4.

$$z_1 = 0.725591 \qquad z_2 = 0.971439$$

$$p_1 = 1.592692 \qquad p_2 = 2.132335$$

for pass-band ripple of 0.05dB, $\varepsilon = 21.997276$

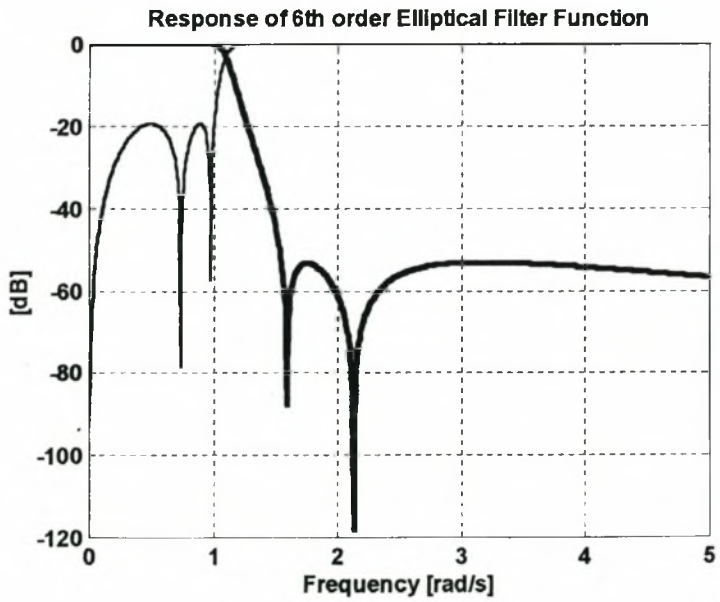

Figure 2.4: Response of 6th order elliptical prototype filter function

$$S_{21}(s) = \frac{M(s)}{N(s)}$$

$$M(s) = s^4 + 7.083520s^2 + 11.533854$$

$$N(s) = 21.997276(s^6 + 2.175886s^5 + 3.837416s^4 + 4.217644s^3 + 3.392813s^2 + 1.794499s + 0.524331)$$

From $N(s)$ R is extracted according to (2.45) as $R = 2.175886/2 = 1.087943\Omega$

$S_{11}(s)$ is usually now calculated from (2.30), but since the positions of the reflection poles are known from the transfer function, $S_{11}(s)$ can be determined directly. From (2.32) and (2.33) the input impedance $Z_{in}(s)$ is calculated:

$$Z_m(s) = 3.814384s^6 + 4.149833s^5 + 10.122597s^4 + 8.043858s^3 + 7.418312s^2 + 3.422454s + 1$$

$$Z_n(s) = 4.149833s^5 + 4.514781s^4 + 8.043858s^3 + 5.52318s^2 + 3.422454s + 1$$

$Z_m(s)$ and $Z_n(s)$ are now divided into their even and odd parts and the admittance parameters are determined from (2.37) and (2.38). The required R_2 can be determined as 1/(constant term in $Z_n(s)$) = 1.

$$y_{22}(s) = \frac{4.149833s^5 + 8.043858s^3 + 3.422454s + 1}{3.814384s^6 + 10.122597s^4 + 7.418312s^2 + 1}$$

$$y_{21}(s) = \frac{s^4 + 7.08352s^2 + 11.533854}{3.814384s^6 + 10.122597s^4 + 7.418312s^2 + 1}$$

The partial fraction expansions required by (2.12) yield the following:

$$K_{21}^{\ 1} = 1.088146 \qquad \lambda_1 = 1.179722j$$
$$K_{21}^{\ 2} = -1.088146 \qquad \lambda_2 = -1.179722j$$
$$K_{21}^{\ 3} = -2.267514 \qquad \lambda_3 = 1.043595j$$
$$K_{21}^{\ 4} = 2.267514 \qquad \lambda_4 = -1.043595j$$
$$K_{21}^{\ 5} = 2.918429 \qquad \lambda_5 = 0.415888j$$
$$K_{21}^{\ 6} = -2.918429 \qquad \lambda_6 = -0.415888j$$

and

$$K_{22}^{\ 1} = 0.094344 \qquad \lambda_1 = 1.179722\text{j}$$
$$K_{22}^{\ 2} = 0.094344 \qquad \lambda_2 = -1.179722\text{j}$$
$$K_{22}^{\ 3} = 0.196596 \qquad \lambda_3 = 1.043595\text{j}$$
$$K_{22}^{\ 4} = 0.196596 \qquad \lambda_4 = -1.043595\text{j}$$
$$K_{22}^{\ 5} = 0.253032 \qquad \lambda_5 = 0.415888\text{j}$$
$$K_{22}^{\ 6} = 0.253032 \qquad \lambda_6 = -0.415888\text{j}$$

Using equation (2.13) the first and last rows of the full **T**-matrix can be found as:

$$T_1 = T_6 = [0.294478 \quad 0.294478 \quad 0.425094 \quad 0.425094 \quad 0.482263 \quad 0.482263]$$

The full **T**-matrix along, with the corresponding diagonal matrix Λ containing the poles λ_k, can then be used to calculate the coupling matrix **M** as in (2.10). It is customary, though, to convert to the even-mode admittance-parameter $Y_e(s)$ at this stage, as the matrix manipulations are faster and more accurate.

With the residues of $y_{21}(s)$ and $y_{22}(s)$ known, equations (2.19) can be used to find the constant C which will yield the required even-mode admittance function:

$$C = 0.086701$$

After cancellation of the partial fraction terms, the required residues and poles remain:

$$K_{ye}^{\ 1} = 0.094344 = 0.307154^2 \qquad T_{e1}^{\ 1} = 0.307154 \qquad \lambda_1 = 1.179722\text{j}$$
$$K_{ye}^{\ 2} = 0.196596 = 0.443392^2 \qquad T_{e1}^{\ 2} = 0.443392 \qquad \lambda_2 = -1.043595\text{j}$$
$$K_{ye}^{\ 3} = 0.253032 = 0.503022^2 \qquad T_{e1}^{\ 3} = 0.503022 \qquad \lambda_3 = 0.415888\text{j}$$

The normalisation constant can be found from:

$$n_1^{\ 2} = \sum_{k=1}^{3} \left(T_{e1}^{\ k}\right)^2 \quad \text{and} \quad T_{e1}' = \frac{T_{e1}}{n_1}$$

where T_{e1}' forms the first row of the $\mathbf{T}_e$-matrix. The other rows are found from the Gram-Schmidt orthonormalisation process with any two other linearly independent unit vectors. In this example [1, 0, 0] and [0, 1, 0] are used to form the general transformation matrix

$$\mathbf{T}_e = \begin{bmatrix} 0.416455 & 0.601173 & 0.682023 \\ 0.909156 & -0.275378 & -0.312413 \\ 0 & 0.750172 & -0.661243 \end{bmatrix}$$

from which the even-mode coupling matrix is determined (2.21).

$$\mathbf{M}_e = \begin{bmatrix} 0.020893 & 0.530822 & -0.658202 \\ 0.530822 & 0.936569 & 0.301501 \\ -0.658202 & 0.301501 & -0.405447 \end{bmatrix}$$

From the even-mode coupling matrix the full coupling matrix can be found. Usually all coupling elements M_{ij} are present and further steps need to be taken to ensure the realisation of the filter in a specific form, i.e. three dual mode cavities or two triple mode cavities etc.

$$\mathbf{M} = \begin{bmatrix} 0 & 0.530822 & 0 & -0.658202 & 0 & 0.020893 \\ 0.530822 & 0 & 0.301501 & 0 & 0.936569 & 0 \\ 0 & 0.301501 & 0 & -0.405447 & 0 & -0.658202 \\ -0.658202 & 0 & -0.405447 & 0 & 0.301501 & 0 \\ 0 & 0.936569 & 0 & 0.301501 & 0 & 0.530822 \\ 0.020893 & 0 & -0.658202 & 0 & 0.530822 & 0 \end{bmatrix}$$

The synthesis can also be done through the direct way of Rhodes as described earlier. From (2.40) we find:

$$D_3(s) = 4.690125\mathrm{s}^3 + (5.102589 + 2.589018\mathrm{j})\mathrm{s}^2 + (5.50873 + 2.710097\mathrm{j})\mathrm{s} + 2.401443 + 2.401443\mathrm{j}$$

$D_3(s)$ can be divided into the even and odd parts of its real and imaginary parts (2.43) and we find $Y_e(s)$ directly from (2.44). The partial fraction expansion of $Y_e(s)$ yields the following residues and poles:

$$K_{ye}^{\ 1} = 0.506063 = 0.711381^2 \qquad T_{e1}^{\ 1} = 0.711381 \qquad \lambda_1 = 1.179722\mathrm{j}$$
$$K_{ye}^{\ 2} = 0.393193 = 0.627051^2 \qquad T_{e1}^{\ 2} = 0.627051 \qquad \lambda_2 = -1.043595\mathrm{j}$$
$$K_{ye}^{\ 3} = 0.188687 = 0.434381^2 \qquad T_{e1}^{\ 3} = 0.434381 \qquad \lambda_3 = 0.415888\mathrm{j}$$

The normalisation constant is determined as $n_1 = 1.043045$, giving exactly the same $\mathbf{T}_e$-matrix as for that found by the Darlington method. The direct method presented by Rhodes is clearly much shorter and as a result it is numerically more accurate.

2.6.2 SIXTH ORDER PSEUDO-ELLIPTICAL DUAL MODE IN-LINE PROTOTYPE FILTER SYNTHESIS

As mentioned previously, the calculated **M**-matrix needs to be transformed for the realisation of different prototype networks, i.e. dual mode or triple mode cavities. When a symmetrical dual mode in-line prototype network is to be realised, an extra realisability condition given by Rhodes et al [25] must be met:

- For a low-pass prototype filter of order N, there must be a minimum number of m transmission zeros at infinity. This number is

$$2m = \begin{cases} \dfrac{N}{2} & \text{for } \dfrac{N}{2} \text{ even} \\ \dfrac{N}{2}+1 & \text{for } \dfrac{N}{2} \text{ odd} \end{cases} \tag{2.51}$$

This constraint means that a sixth order elliptical filter (with only two zeros at infinity) is unrealisable using a dual mode in-line prototype network.

The general form of the n x n even mode coupling matrix adhering to the realisability condition above, is the following:

$$\mathbf{M}_e = \begin{bmatrix} M_{11} & M_{12.} & 0 & 0 & & & \\ M_{12} & M_{22} & M_{23} & 0 & & & \\ 0 & M_{23} & M_{33} & M_{34} & & & \\ 0 & & & & & & \\ & & & & & & \\ & & & & & M_{n-1,n-1} & M_{n-1,n} \\ & & & & & M_{n-1,n} & M_{n,n} \end{bmatrix} \tag{2.52}$$

with $M_{r,r} = 0$ for $r = 1$ to $m - 1$

This matrix is not yet in the correct form required to realise the filter function, and must be transformed using the matrix reduction techniques discussed in section 3. The specific transformation for this type of realisation does not follow any general rule and is derived for the even degrees 6 to 12 in [25]. For a sixth order prototype filter the necessary transformation is as follows:

$$\begin{bmatrix} 0 & M_{12} & 0 \\ M_{12} & M_{22} & M_{23} \\ 0 & M_{23} & M_{33} \end{bmatrix} \rightarrow \begin{bmatrix} 0 & M'_{12} & M'_{13} \\ M'_{12} & 0 & M'_{23} \\ M'_{13} & M'_{23} & M'_{33} \end{bmatrix} \tag{2.53}$$

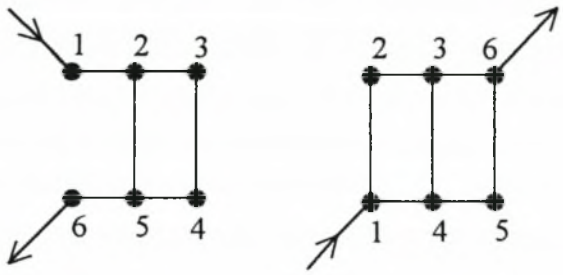

Figure 2.5: The transformation for a 6^{th} order dual mode in-line network [25].

The even-mode coupling matrix reduction method presented in section 3 is used to reduce M_{22} to zero, yielding the required even-mode coupling matrix illustrated in figure 2.3. The full coupling matrix resulting from this transformation is

$$\mathbf{M} = \begin{bmatrix} 0 & M_{12} & 0 & M_{14} & 0 & 0 \\ M_{12} & 0 & M_{23} & 0 & 0 & 0 \\ 0 & M_{23} & 0 & M_{34} & 0 & M_{36} \\ M_{14} & 0 & M_{34} & 0 & M_{45} & 0 \\ 0 & 0 & 0 & M_{45} & 0 & M_{56} \\ 0 & 0 & M_{36} & 0 & M_{56} & 0 \end{bmatrix} \tag{2.54}$$

As an example, a sixth order Chebyschev Real Function low-pass prototype filter function is used. In order to satisfy (2.51) two transmission zeros are chosen at infinity and a zero at $\omega_1 = 1.71 rad/s$. For a pass-band ripple of 0.05dB a ripple constant of ε = 0.107608 is chosen. The minimum attenuation in the stop-band is 50dB and the response of the low-pass prototype is shown in figure 2.6.

The synthesis of the filter is done using Rhodes' method and the even-mode admittance driving function is calculated as:

$$Y_e(s) = \frac{k_1}{s-\lambda_1} + \frac{k_2}{s-\lambda_2} + \frac{k_3}{s-\lambda_3}$$

$$K_1 = 0.171780 \qquad \lambda_1 = 1.169165\text{j}$$
$$K_2 = 0.369138 \qquad \lambda_2 = -0.991048\text{j}$$
$$K_3 = 0.430589 \qquad \lambda_3 = 0383184\text{j}$$

The $\mathbf{T}_e$-matrix is calculated from (2.22) and (2.23)

$$\mathbf{T}_e = \begin{bmatrix} 0.665746 & 0.616413 & 0.420497 \\ 0.746178 & -0.549968 & -0.375170 \\ 0 & 0.563534 & -0.826093 \end{bmatrix}$$

and the resulting $\mathbf{M}_{e1}$-matrix is:

$$\mathbf{M}_{e1} = \begin{bmatrix} 0 & -0.34188 & 0.750392 \\ -0.34188 & -0.078157 & -0.669505 \\ 0.750392 & -0.669505 & -0.483145 \end{bmatrix}$$

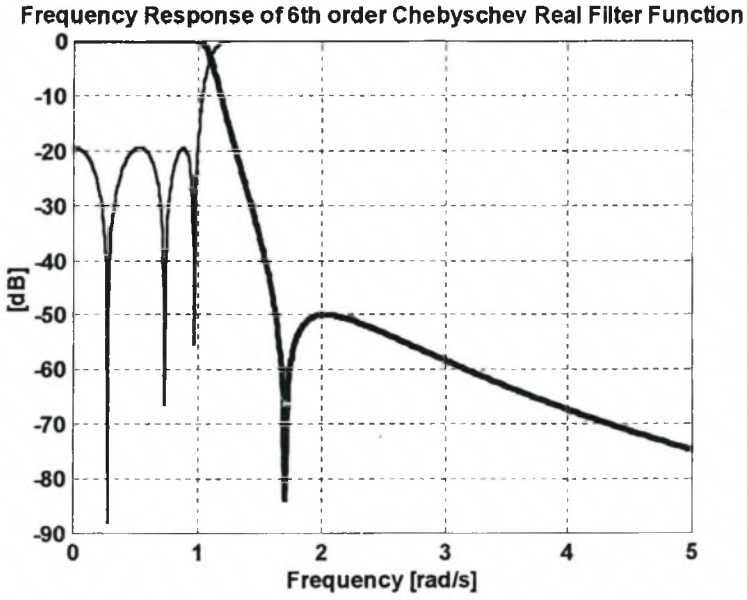

Figure 2.6: Response of 6th order Chebyschev Real Prototype Filter Function.

This matrix must be transformed to obtain the required form of equation (2.52). This is done by reducing $M_{e1}(1,3)$ to zero using the folded canonical method in section 3 with pivot [2,3]. The matrix resulting from this first transformation is:

$$\mathbf{M}_{e2} = \begin{bmatrix} 0 & 0.824603 & 0 \\ 0.824603 & 0.091661 & 0.592136 \\ 0 & 0.592136 & -0.652963 \end{bmatrix}$$

The reduction method by Rhodes presented in section 3 is now used to reduce this matrix to the form of equation (2.53). The roots of t are determined according to (2.28) and (2.29).

$$t = -1.888042 \text{ or } 0.074351$$

and the angle of rotation:

$$\theta = \tan^{-1} t$$
$$= -1.083712$$

$$c_r = \cos\theta$$
$$s_r = \sin\theta$$

$$\mathbf{R} = \begin{bmatrix} 1 & 0 & 0 \\ 0 & c_r & -s_r \\ 0 & s_r & c_r \end{bmatrix}$$

This transformation through equation (2.24) results in the required form for an even-mode coupling matrix realisable as a dual mode in-line network:

$$\mathbf{M}_{e3} = \begin{bmatrix} 0 & 0.385957 & -0.728703 \\ 0.385957 & 0 & -0.640684 \\ -0.728703 & -0.640684 & -0.561302 \end{bmatrix}$$

yielding the full coupling matrix:

$$\mathbf{M} = \begin{bmatrix} 0 & 0.385957 & 0 & -0.728703 & 0 & 0 \\ 0.385957 & 0 & -0.640684 & 0 & 0 & 0 \\ 0 & -0.640684 & 0 & -0.561302 & 0 & -0.728703 \\ -0.728703 & 0 & -0.561302 & 0 & -0.640684 & 0 \\ 0 & 0 & 0 & -0.640684 & 0 & 0.385957 \\ 0 & 0 & -0.728703 & 0 & 0.385957 & 0 \end{bmatrix}$$

For realisability all elements along the main diagonal must be positive. The absolute values of these elements can be used, as it has no effect on the resulting network. The final coupling matrix that will be realised is therefore:

$$\mathbf{M} = \begin{bmatrix} 0 & 0.385957 & 0 & -0.728703 & 0 & 0 \\ 0.385957 & 0 & 0.640684 & 0 & 0 & 0 \\ 0 & 0.640684 & 0 & 0.561302 & 0 & -0.728703 \\ -0.728703 & 0 & 0.561302 & 0 & 0.640684 & 0 \\ 0 & 0 & 0 & 0.640684 & 0 & 0.385957 \\ 0 & 0 & -0.728703 & 0 & 0.385957 & 0 \end{bmatrix}$$

2.7 CONCLUSION

This chapter presented the basic methods used in synthesis of narrow-band multiple-coupled cavity filters.

The theory is based upon an equivalent circuit description of multiple-coupled resonators, where the couplings between synchronously tuned resonators are controlled by mutual inductances. Writing the resonator loop equations in matrix form, results in a coupling matrix containing the mutual inductances. This matrix controls the response of the coupled resonator network.

In the following chapters these coupling matrices will be linked to physical coupled cavity structures, resulting in high-performance coupled cavity filter components.

Chapter 3

Classical Coupled Cavity Filter Design

3.1 INTRODUCTION

This chapter presents design techniques derived from electromagnetic theory, network theory and empirical models. These methods form the basis of multiple-coupled cavity filter design and have been used as such since the earliest prototypes of these filters were presented [5, 6].

The two main aspects of coupled cavity filter design are the design of cavity resonators and irises that couple energy between these resonators. In this chapter cavity resonator design will be introduced first, followed by iris design and the effect that irises have on the cavity resonant frequency. The chapter is concluded by providing two filter design examples.

3.2 CAVITY RESONATOR DESIGN

Distributed resonant circuits utilise the resonant properties of standing waves created by interference of forward and reverse travelling waves on the transmission structure. Microwave cavity resonators are created by enclosing a volume of dielectric by a conducting material. Such a resonator supports an infinite number of resonant modes, each at a specific resonant frequency. In a cylindrical cavity resonator (figure 3.1) the resonant modes can be divided into TE_z and TM_z mode sets.

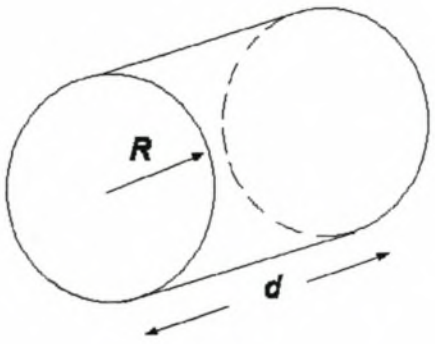

Figure 3.1: Cylindrical cavity resonator

$\underline{TE_z}$

$$
\begin{aligned}
H_z &= J_n(k_c r)\cos n\phi \sin \beta z \\
E_r &= \frac{j\omega\mu n}{k_c^2}\frac{J_n(k_c r)}{r}\sin n\phi \sin \beta z \\
E_\phi &= \frac{j\omega\mu}{k_c} J_n'(k_c r)\cos n\phi \sin \beta z \\
H_r &= -\frac{\beta}{k_c} J_n'(k_c r)\cos n\phi \cos \beta z \\
H_\phi &= \frac{\beta n}{k_c^2}\frac{J_n(k_c r)}{r}\sin n\phi \cos \beta z
\end{aligned}
\tag{3.1}
$$

$\underline{TM_z}$

$$
\begin{aligned}
E_z &= J_n(k_c r)\cos n\phi \cos \beta z \\
E_r &= -\frac{\beta}{k_c} J_n'(k_c r)\cos n\phi \sin \beta z \\
E_\phi &= -\frac{\beta n}{k_c^2}\frac{J_n(k_c r)}{r}\sin n\phi \sin \beta z \\
H_r &= \frac{j\omega\varepsilon n}{k_c^2}\frac{J_n(k_c r)}{r}\sin n\phi \cos \beta z \\
H_\phi &= -\frac{j\omega\varepsilon}{k_c} J_n'(k_c r)\cos n\phi \cos \beta z
\end{aligned}
\tag{3.2}
$$

where $J_n(k_c r)$ is the Bessel function of the first kind and $J_n'(k_c r) = \frac{\partial J_n(k_c r)}{\partial r}$.

n, l and v are the mode indices; n = 0, 1, 2, ..., l = 1, 2, 3, ..., and

$$v = \begin{cases} 1, 2, 3, \ldots \text{ TE-modes} \\ 0, 1, 2, \ldots \text{ TM-modes} \end{cases}$$

$\beta = \frac{v\pi}{d}$ and v the number of half wavelengths in the z-direction.

$k_c = \frac{p_{nl}}{R}$ with p_{nl} the l^{th} zero of the Bessel function of order n for the TM modes, and

p_{nl} the l^{th} zero of the derivative of the Bessel function of order n for the TE modes

In equations (3.1) and (3.2) degenerate modes exist for all modes that do not have axial symmetry, i.e. all modes with $n > 0$.

The resonant frequencies can be determined from a relation between the cavity wavelength and the number of half wavelengths p in the cavity [36]:

$$d = \frac{v\lambda_g}{2} = \frac{v\lambda}{2}\sqrt{1-\left(\frac{\lambda}{\lambda_c}\right)^2} \tag{3.3}$$

With λ_c the cut-off wavelength of the resonant mode in the cavity,

$$f_0 = \frac{cv}{2d}\sqrt{1+\left(\frac{2d}{v\lambda_c}\right)^2} \tag{3.4}$$

For the case of a TM_{n10}-mode, the mode is resonant at the cut-off frequency, with the length of the cavity arbitrary. In designing a cavity resonator it is always important to know whether other modes in the cavity are close to resonance. Such modes are called spurious modes and can cause unwanted transmission responses. Depending on the application, a relatively large spurious free frequency band (5-10%) may be required and the conventional way of determining this is by using a mode chart. A mode chart showing the resonant frequencies of some neighbouring modes relative to the resonant frequency of the TE_{111} mode is shown in figure 3.2.

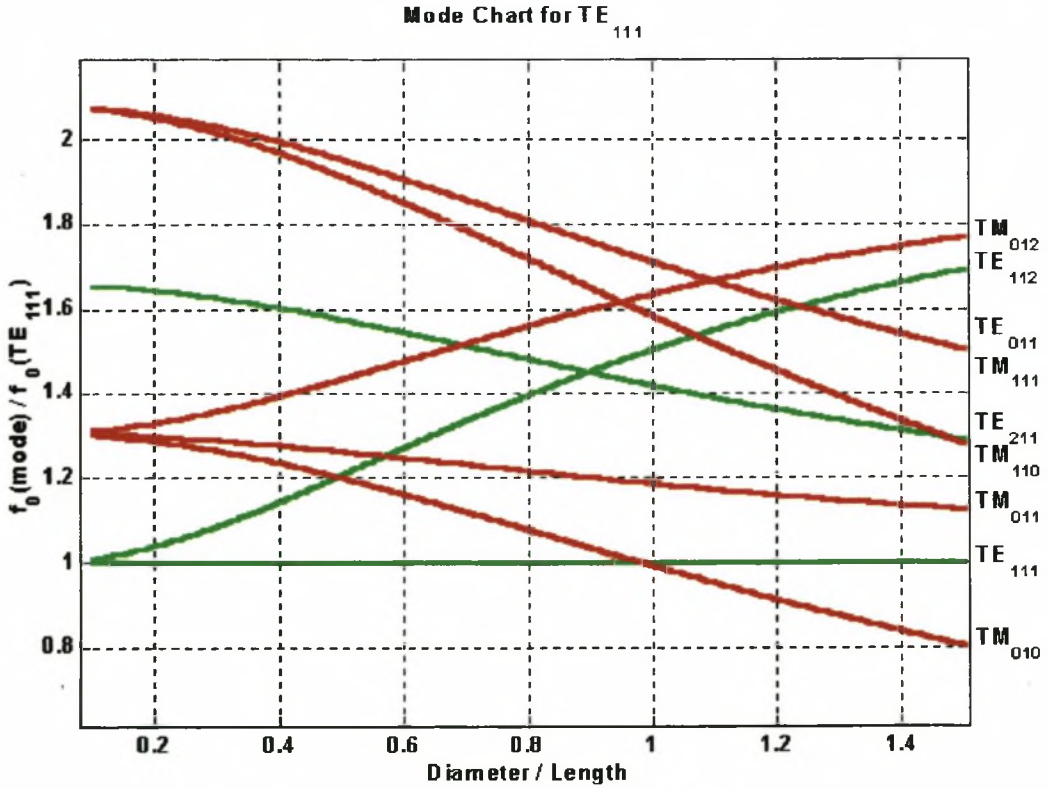

Figure 3.2: Mode chart of TE_{111} mode

For higher order modes the mode chart becomes more congested and spurious free regions become smaller. While degenerate modes exist for all modes where $n > 0$, mode line crossings on the mode chart also indicate that these modes are degenerate for that specific diameter to length ratio.

Another very important property of a cavity resonator is the unloaded Q, which is an indication of the ratio of power loss in the walls of the cavity to the amount of energy stored in the cavity.

$$Q_u = \frac{\omega U}{P_l} \tag{3.5}$$

The energy stored in the modes can be determined using either the stored magnetic or electric energy, as they are equal at resonance. It is usually most convenient to use the electric energy for TE_z modes ($E_z = 0$) and the magnetic energy for TM_z modes ($H_z = 0$).

$$U = \frac{\varepsilon_0}{2}\iiint_V \boldsymbol{E}\cdot\boldsymbol{E}dv = \frac{\mu_0}{2}\iiint_V \boldsymbol{H}\cdot\boldsymbol{H}dv \tag{3.6}$$

The losses caused by finite conductivity of the cavity walls can be determined from the surface currents associated with the loss-free field solutions [37].

$$\boldsymbol{J}_s = \hat{\boldsymbol{n}}\times\boldsymbol{H} \tag{3.7}$$

where $\hat{\boldsymbol{n}}$ is a unit vector normal to the surface directed into the cavity. The power loss is then:

$$P_l = \frac{R}{2}\int_{\text{walls}} \boldsymbol{J}_s\cdot\boldsymbol{J}_s^* dS = \frac{R}{2}\int_{\text{walls}} |\boldsymbol{H}_{\tan}|^2 dS \tag{3.8}$$

In equation (3.8) $R = 1/\sigma\delta_s$ is the resistive part of surface impedance of the metal wall with conductivity σ and skindepth $\delta_s = (2/\omega\mu\sigma)^{1/2}$. Substitution of equations (3.6) to (3.8) into equation (3.5) leaves [37]:

$$Q_u = \frac{\lambda_0}{\delta_s}\frac{\left[1-\left(\frac{n}{p_{nl}}\right)^2\right]\left[p_{nl}^2+\left(\frac{v\pi R}{d}\right)^2\right]^{\frac{3}{2}}}{2\pi\left[p_{nl}^2+\frac{2R}{d}\left(\frac{v\pi R}{d}\right)^2+\left(1-\frac{2R}{d}\right)\left(\frac{nv\pi R}{p_{nl}d}\right)^2\right]} \quad \text{for TE modes and} \tag{3.9}$$

$$Q_u = \frac{\lambda_0}{\delta_s} \begin{cases} \dfrac{\left[p_{nl}^2 + \left(\dfrac{v\pi R}{d} \right)^2 \right]^{\frac{1}{2}}}{2\pi \left(1 + \dfrac{2R}{d} \right)} & l > 0 \\ \dfrac{p_{nl}}{2\pi \left(1 + \dfrac{2R}{d} \right)} & l = 0 \end{cases} \quad \text{for TM modes} \qquad (3.10)$$

In most cases the use of higher order modes results in higher unloaded Q-values as a result of a higher volume to surface area ratio.

3.3 CLASSICAL IRIS DESIGN

Coupling in multiple-coupled waveguide cavity filters is often described in two ways, depending on the equivalent network prototype used. While the Kurzrok type of description [38] uses a LC prototype that relates to the susceptances of the iris structures (input-output and coupling irises), a coupling coefficient between coupled resonators is normally used. Most of this chapter will deal with the coupling coefficient description, but some properties, such as the influence of irises on the resonator frequencies, is best described in terms of normalised iris reactance. Relationships between the two descriptions can also be derived and is described at the end of this section.

The coupling of an electromagnetic field through a small aperture in a common wall of zero thickness between two waveguide regions, can be derived using Bethe's theory [2]. The field generated in the second region depends on the field-strengths in the first cavity and the polarisability (geometry) of the aperture. Since Bethe's theory only holds for very small apertures in walls of zero thickness, several contributions were made to include the effects of large apertures and non-zero wall-thickness. Cohn ([39], [3] and [40]) measured the polarisabilities for larger apertures and Levy [41] and McDonald [42] proposed correction factors to account for these effects. This theory has been used extensively in iris design since the first commercial multi-mode filters were introduced by Atia and Williams [5] in the early 1970's.

3.3.1 COUPLING COEFFICIENT

The equivalent network prototype of the general multiple-coupled cavity filter is repeated in figure 3.3 with the coupling coefficient related to the mutual inductance given by equation (3.11).

$$K_{ij} = \frac{M_{ij}}{\sqrt{L_1 L_2}} = M_{ij} \tag{3.11}$$

The mutual inductances can be related directly to the coupling coefficients between two waveguide cavities connected by an aperture in a common wall.

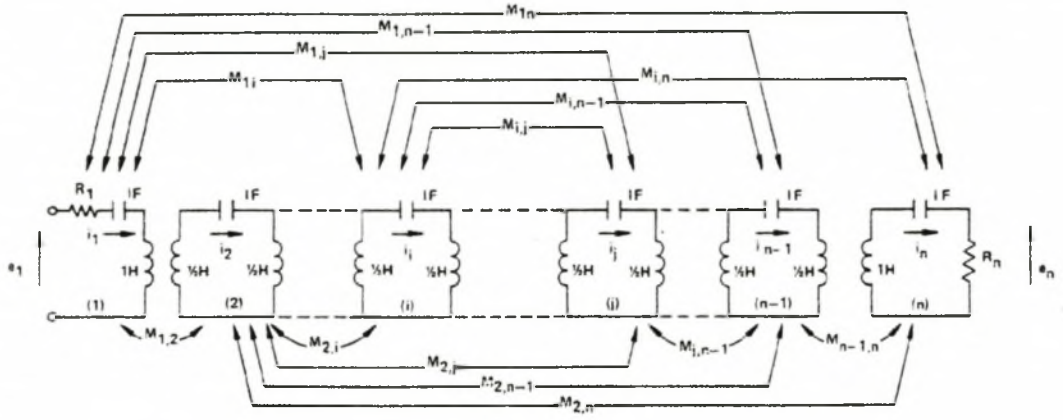

Figure 3.3: Equivalent circuit of multiple-coupled cavity filter.

The most general equation relating the coupling coefficient between two identical cavities connected by an aperture in a common wall, is given by Rosenberg [43]:

$$\bar{K} = \frac{\text{Energy lost through aperture by coupling}}{2 \cdot \text{Energy stored in cavity mode}} \tag{3.12}$$

The term above the line is derived from Bethe's theory which relates the electromagnetic fields incident on one side of the iris to the fields generated on the other side. Electric and magnetic dipoles placed in the centre of the apertures, form the sources for fields generated in the second region. The magnitudes of the dipoles depend on the strengths of the tangential H-fields and perpendicular E-fields in the first region, and the geometry of the aperture. Quantitatively, the electric and magnetic dipole moments are given by:

$$\begin{aligned} \boldsymbol{P}_o &= -\varepsilon_o P \boldsymbol{E}_n \\ \boldsymbol{M}_o &= -M \boldsymbol{H}_t \end{aligned} \tag{3.13}$$

where P is the electric, and M the magnetic polarisability of the aperture. Using Bethe's theory the average power lost through the aperture can be determined [44]:

$$P_L = \frac{|A_a|^2 S_a}{2} \tag{3.14}$$

where A_a, the amplitude of the normal mode fields excited in the coupled cavity, is given by:

$$A_a = \frac{\omega\left(\mu_0 M H_t^2 + \varepsilon_0 P E_n^2\right)}{S_a} \tag{3.15}$$

In equation (3.15) P and M are again the electric and magnetic polarisabilities of the aperture. S_a is the peak power of the coupling mode in the coupled cavities and can be determined from the Pointing vector:

$$S_a = \iint_S \mathrm{Re}\left[\boldsymbol{E} \times \boldsymbol{H}^*\right] \cdot d\boldsymbol{s} \tag{3.16}$$

The energy stored in the modes can be determined using equation (3.6). Substitution of equations (3.6) and (3.14) – (3.16) into equation (3.12) provides the basic equation whereby the coupling coefficient between two cavities connected by an aperture in a common wall can be calculated.

$$K = M \frac{\boldsymbol{H}_t \cdot \boldsymbol{H}_t}{\iiint_V \boldsymbol{H} \cdot \boldsymbol{H} dv} + P \frac{\boldsymbol{E}_n \cdot \boldsymbol{E}_n}{\iiint_V \boldsymbol{E} \cdot \boldsymbol{E} dv} \tag{3.17}$$

Where $\boldsymbol{H}_t$ and $\boldsymbol{E}_n$ are taken in the centre of the aperture. The practical implications of this equation are the following [45]:

- Coupling through apertures is obtained by tangential magnetic fields and perpendicular electric fields in the aperture.
- To couple two modes, the same field components must exist in the aperture.
- If both tangential magnetic and perpendicular electric fields exist in the aperture, the magnetic and electric polarisabilities of the aperture control the relative coupling strengths.

- TE_z modes have no E_z components and therefore no perpendicular E-field components: Coupling can only occur through tangential magnetic fields in the aperture.
- TM_z modes have E_z components: Coupling can occur through tangential magnetic fields and perpendicular electric fields in aperture. To limit coupling to either one an aperture with the correct polarisability must be chosen.

Equation (3.17) can be used to calculate the coupling coefficient analytically by substituting the field expansions of the coupling modes. Some analytical solutions, such as for the end-wall coupling of two cylindrical cavities supporting the TE_{11n} resonance, are readily available [6]. Noting that the perpendicular E-field is zero in this case, the coupling coefficient becomes:

$$K = \frac{M\lambda_0^2 n^2}{l_c^3 3R^2} \tag{3.18}$$

where n is the number of half-wavelengths along the length of the cavity, l_c is the cavity length and R the cavity radius with the magnetic polarisability M the only unknown.

3.3.2 CALCULATION OF EXTERNAL Q OF WAVEGUIDE TERMINATED CAVITIES

The two-port network terminations found in figure 3.3 are most conveniently realised by using the loaded or the external Q of waveguide terminated cavities. The external Q is related to the network termination by [6]:

$$Q_e = \frac{1}{R} \tag{3.19}$$

and can be calculated using equation (3.20) given by [44]

$$Q_e = \frac{\omega U}{P_L} \tag{3.20}$$

where $\omega = 2\pi f$ is the angular resonance frequency, U is the energy stored in the cavity resonant mode and P_L is the average power lost through the iris to the terminating guide. The energy stored can be calculated from equation (3.6) in the same way as in the previous section. The average power lost through the iris is again given by equation (3.14), where A_a now becomes the amplitude of the normal mode

field in the terminating guide. The terminating guide in this work is always WR90 X-band rectangular waveguide and for the frequency range of interest the only propagating mode is the TE_{10} mode. With this in mind, equation (3.15) becomes

$$A_a = \frac{\omega \mu_0 M H_{term} H_{cav}}{S_a} \tag{3.21}$$

with M the magnetic polarisability of the iris, H_{term} the amplitude of the tangential magnetic field in the terminating guide, and H_{cav} the amplitude of the tangential magnetic field in the cavity in the centre of the aperture. S_a is the peak power of the normal mode in the terminating guide and can be calculated using equation (3.16). Specific loaded Q-values of waveguide terminated coupled cavities can now be determined by substitution of the mode fields in the various regions into the preceding equations. For example, the external Q of a cylindrical cavity supporting a TE_{11n} resonance, terminated by a rectangular waveguide at the end-wall, is given by [6]:

$$Q_e = \frac{abl_c^3 \lambda_g 3R^2}{4\pi M^2 \lambda^2 n^2} \tag{3.22}$$

where a and b are the cross-sectional dimensions of the rectangular waveguide, λ_g the wavelength in the rectangular waveguide and l_c and R the length and the radius of the cavity respectively. The parameter n is the number of half-wavelengths along the length of the cavity and M the magnetic polarisability of the iris.

3.3.3 POLARISABILITIES OF RECTANGULAR APERTURES

The polarisabilities of apertures can be derived analytically for simple geometries such as small circular and elliptical apertures in side-walls of zero thickness [2]. For example, a circular aperture of radius r has polarisabilities of $M = -\frac{2}{3}r^3$ and $P = \frac{4}{3}r^3$ [37] and a long narrow aperture of length l and width w has polarisabilities of $M = P = \frac{\pi}{16} l w^2$ [44]. Some attempts have also been made to calculate the polarisabilities by numerical methods such as the method of moments [46].

For more practical irises of finite thickness the measured polarisabilities by Cohn are used. Both the magnetic and electric polarisabilities of a number of different apertures with varying sizes were measured by means of an electrolytic tank experiment [3, 39]. While these measured values are for thin irises and apertures

small relative to the wavelength in the cavity, they still form the basis for the calculation of polarisabilities of a wide range of irises.

3.3.3.1 ELECTRICALLY LARGE APERTURES

As the size of an aperture increases, it approaches resonance and the polarisability of the aperture is greatly increased. Bethe's theory does not include this effect. Cohn [40] derives correction factors for apertures large relative to the cavity wavelength by examining Foster's reactance theorem. Since this theorem holds for any lossless passive two-terminal network, the reactance of an iris can be expressed as:

$$X(f) = -\frac{1}{B(f)} = \sum_{r=0}^{n} \frac{p_r f}{1 - \frac{f^2}{f_r^2}} + qf - \frac{m}{f} \tag{3.23}$$

where $X(f)$ is the reactance and $B(f)$ is the susceptance of the network, f is the frequency, f_r the frequencies of the poles of $X(f)$, and p_r, q and m are positive real constants. Comparing equation (3.23) to the derived reactance function of a small aperture in an infinitely thin iris for a TE_{11} mode in cylindrical waveguide [44], shows that for Bethe's small-aperture theory $p_r = m = 0$, which is equivalent to the reactance of the following conductance

$$X = -\frac{1}{B} = \frac{4\pi M Z_0}{0.955(\pi R^2)\lambda_g} \tag{3.24}$$

with Z_0 the waveguide impedance, λ_g the wavelength in the guide and R the cylinder radius. While this is a very good approximation for small apertures, practical apertures have an unlimited number resonances that must be included to model larger apertures. Cohn [40] also gives two extensions of equation (3.24) that account for these resonances.

$$\frac{X}{Z_0} = -\frac{Y_0}{B} = \frac{4\pi M}{0.955\left(\pi R^2\right)\lambda_g\left(1 - \frac{f^2}{f_r^2}\right)} \tag{3.25}$$

$$\frac{X}{Z_0} = -\frac{Y_0}{B} = \frac{4\pi M}{0.955\left(\pi R^2\right)\lambda_g}\left(\frac{2f_r}{\pi f}\tan\frac{\pi f}{2f_r}\right) \tag{3.26}$$

The first is a single pole function and in the second poles occur at $f = (2r+1)f_r$ and zeros at $f = 2rf_r$ for all integer values of m. Similarly, an infinite number of

reactance functions that conform to Foster's theorem and reduce to (3.24) for $f \to 0$ can be found. Cohn reports that in experimental investigation of many aperture shapes and sizes, the single-pole relation of equation (3.25) outperforms equation (3.26) and is recommended for use up to the first resonance of the aperture.

In order to use the above equations, the resonant frequency of the apertures must be determined. An empirical relationship for the resonant frequency of a rectangular aperture with length l and width w situated in the centre of a rectangular waveguide, is given by Cohn [40].

$$l = \frac{\lambda_r}{2}\sqrt{1+\left(\frac{2aw}{b\lambda_{g0}}\right)^2} \tag{3.27}$$

with λ_{g0} the guide wavelength. For w/l small, this reduces to $l \approx \lambda_r/2$ so that the resonant frequency of the aperture is almost equal to the cut-off frequency of TE_{10} mode in a waveguide with the same dimensions as the aperture. Rosenberg [43] presents another relation derived from (3.14):

$$f_r = \frac{c}{2l}\sqrt{1+\left(\frac{2w}{\lambda_{g0}}\right)^2} \tag{3.28}$$

The correction factor for the inclusion of the resonance of apertures large relative the guide wavelength is therefore:

$$c_1 = \frac{1}{1-\left(\frac{f}{f_r}\right)^2} \tag{3.29}$$

with f_r given by equations (3.27) and (3.28).

While the correction factors given above are derived for the magnetic polarisability of apertures with only tangential magnetic fields incident on the iris, the same correction factor holds for the electric polarisability, where, for w/l small, the resonant frequency of the aperture is almost equal to the cut-off frequency of the TM_{11} in a rectangular waveguide with the same dimensions as the aperture.

3.3.3.2 IRISES WITH FINITE THICKNESS

A second correction factor is introduced for the effect of finite wall thickness of an iris, t, which attenuates transmission through it [40]. The total attenuation α is approximately equal to the sum of the attenuation α_0 of an infinitely thin iris, and the attenuation α_1 of a length of waveguide, with the length equal to the thickness of the aperture. The two contributing factors are:

$$\alpha_0 = 10\log_{10}\frac{1}{|S_{nm}|^2}\,\text{dB} \tag{3.30}$$

$$\alpha_1 = \frac{54.6tA}{\lambda_c}\sqrt{1-\left(\frac{\lambda_c}{\lambda}\right)^2}\,\text{dB} \tag{3.31}$$

The correction factor required must account for the attenuation of the finite thickness of the iris given in equation (3.31) and can be rewritten as [41]

$$\begin{aligned} c_{2m} &= \exp\left[\frac{-2\pi A_m t}{\lambda_{cm}}\sqrt{1-\frac{f^2}{f_{cm}^2}}\right] \\ c_{2e} &= \exp\left[\frac{-2\pi A_e t}{\lambda_{ce}}\sqrt{1-\frac{f^2}{f_{ce}^2}}\right] \end{aligned} \tag{3.32}$$

where the first is the correction factor for magnetic polarisability with λ_{cm} and f_{cm} the cut-off wavelength and frequency for the TE_{10} mode in the aperture. The second equation is for the electric polarisability with λ_{ce} and f_{ce} the cut-off wavelength and frequency of the TM_{11} mode in the aperture. A_m and A_e were originally empirical constants with values ranging between one and three to account for slightly larger attenuation than what was expected [41]. A is approximately equal to three for $t < 0.02l$ and decreases slowly to one for large values of t.

McDonald [42] investigated the effect of finite iris thickness and calculated the magnetic and electric polarisabilities of thick irises using a variational technique. Levy [41] uses these results to determine relationships for A_m and A_e for thick cylindrical irises and shows how the original empirical constants are validated.

3.3.3.3 VARIATION OF FIELD-STRENGTH OVER THE APERTURE

In the original work by Bethe, the apertures were assumed to be very small so that the field distribution incident on the iris was assumed to be constant. For larger apertures,

though, a third correction term was introduced by Levy [41] to include the effect of variation of field-strength over the aperture. This basically comes down to an averaging of the fields incident upon the iris over the length of the aperture, and can be written as

$$c_{3m} = \frac{\int_l |H_t|^2 \, dl}{|H_{t\max}|^2 \, l}$$
$$c_{3e} = \frac{\int_l |E_n|^2 \, dl}{|E_{n\max}|^2 \, l} \tag{3.33}$$

where c_{3m} and c_{3e} are the correction factors for the magnetic and electric polarisabilities respectively. The final corrected polarisabilities can now be found by multiplying the various correction factors from equations (3.29), (3.32) and (3.33).

$$M_{corr} = c_1 c_{2m} c_{3m} M$$
$$P_{corr} = c_1 c_{2e} c_{3e} P \tag{3.34}$$

3.3.4 DETERMINING THE COUPLING COEFFICIENT FROM THE IRIS REACTANCE

Kurzrok [38] presents the following relationship between the coupling susceptance of *LC*-ladder network and the coupling coefficient of an iris coupling two resonant cavities.

$$B_{ij} = \frac{1}{\frac{\pi}{2}\left(\frac{\lambda_g}{\lambda_0}\right)^2 K_{ij}} \tag{3.35}$$

where B_{ij} is the normalised susceptance of the coupling circuit element between i^{th} and j^{th} resonators, K_{ij} is the coupling coefficient between the two resonators, and λ_g and λ_0 are the guide and free-space wavelengths respectively. This equation can be modified to include the relationship between the impedance inverter description of an iris and the coupling coefficient [47].

$$K = \frac{2}{\pi}\left(\frac{\lambda_0}{\lambda_g}\right)^2 \cdot K_{\text{inv}} \tag{3.36}$$

The impedance inverter K_{inv} and insertion phase ϕ can be determined from an equivalent T-circuit with a shunt reactance X_p and series reactances X_s on each arm [48].

$$\phi = -\tan^{-1}\left(\frac{2X_p + X_s}{Z_0}\right) - \tan^{-1}\frac{X_s}{Z_0}$$
$$K_{inv} = Z_0\left|\tan\left(\frac{\phi}{2} + \tan^{-1}\frac{X_s}{Z_0}\right)\right| \tag{3.37}$$

For thick irises these reactances can be determined from the scattering parameters of the iris as is shown in the EM-analysis chapter. For thin irises the series reactances become negligibly small and the shunt reactance can be determined using small aperture theory. The insertion phase and the impedance inverter are then determined from [4]:

$$\phi = -\tan^{-1}\frac{2X_p}{Z_0}$$
$$K_{inv} = Z_0\left|\tan\frac{\phi}{2}\right| \tag{3.38}$$

The equations above are derived for waveguide modes independent of the cavity length. It is clear from equation (3.12) that for the same iris, the coupling coefficient changes when higher order modes are used. For example, $K_{TE_{111}} = 3K_{TE_{113}}$ because the TE_{113} mode stores three times more energy than the TE_{111} mode. The coupling coefficient determined from equation (3.36) can therefore only be correct for modes with a specific number of half wavelengths in the z-direction. To find the correct relation between equations (3.17) and (3.36) an iris with a centred rectangular aperture was placed in a cylindrical waveguide supporting TE_{11} and TM_{01} modes. For such an iris there will be no cross-coupling between the two propagating modes and TE- and TM-modes will couple only through tangential magnetic fields and perpendicular electric fields respectively. For the TE_{11} mode the normalised inductive susceptance can be determined using small aperture theory [37] and is given in equation (3.24). The normalised capacitive susceptance of the iris with the TM_{01} mode incident is found to be:

$$\frac{B}{Y_0} = \frac{Z_0}{X} = \frac{0.92R^4}{P\lambda_g} \tag{3.39}$$

The coupling coefficients can be determined from equation (3.18) for the TE_{11n} mode and equation (3.40) for the TM_{01n} modes $n > 0$.

$$K_{TM_{01n}} = \frac{2\lambda_0^2 P}{\pi d R^2 J_1^2(k_c R)\lambda_c^2} \tag{3.40}$$

Table 3.1 summarises the results of this comparison between the two coupling coefficient calculation methods.

Table 3.1: Comparison of coupling coefficient calculation methods

	TM_{011}	TM_{012}	TM_{013}	TM_{014}
K equation (3.17)	$6.0986 \cdot 10^{-4}$	$3.0493 \cdot 10^{-4}$	$2.0329 \cdot 10^{-4}$	$1.52461 \cdot 10^{-4}$
K_{inv} equation (3.36)	$6.0975 \cdot 10^{-4}$	$6.0975 \cdot 10^{-4}$	$6.0975 \cdot 10^{-4}$	$6.0975 \cdot 10^{-4}$
	TE_{111}	TE_{112}	TE_{113}	TE_{114}
K equation (3.17)	0.01543	0.007714	0.005142	0.003857
K_{inv} equation (3.36)	0.01539	0.01539	0.01539	0.01539

It is clear from the table that the method using the impedance inverter corresponds very well to the well-known method from equation (3.17) for a one half-wavelength cavity resonator. Also evident is the fact that higher order coupling factors can also be determined from the equivalent *T*- reactance circuit by dividing the coupling coefficient by the number of half-wavelengths in the cavity. The result can then be described as the coupling coefficient of the iris connected to a *v*- half wavelength resonator that is resonant at the frequency at which the iris reactance was determined.

$$K_{niv} = \frac{K_{inv}}{v} \tag{3.41}$$

3.4 EFFECT OF IRISES ON CAVITY RESONANCE

Depending on the mode incident on the iris, the iris will either cause a slight increase or decrease in the resonant frequency of the cavity. At resonance a delicate balance exists between the electric and magnetic fields of the resonant mode. The introduction of an iris disturbs this balance and the resonant frequency changes in response to the effect of the iris. When the coupling is mostly as a result of tangential magnetic fields, as is the case for most irises described here, a slight decrease in the resonant frequency of the coupling mode will be experienced. The amount of electrical length that is added by the iris can be determined from:

$$\phi = \tan^{-1}\frac{2X}{Z_0} \tag{3.35}$$

where X/Z_0 is the normalised reactance of the iris. This value can be calculated analytically for each mode incident on the iris and is given for TE_{11}–mode in equation (3.25). The result is that the coupling coefficient that is calculated using the small aperture theory is not correct for the frequency it was calculated at, but for a slightly lower resonant frequency that can be calculated by taking the added phase of equation (3.35) into account. The coupling coefficient is therefore not frequency independent as is assumed in the synthesis techniques. This can be a source of error when small aperture theory, numerical techniques and measurement methods are compared. For input coupling from rectangular waveguide to the TE_{11}–mode in a cylindrical cavity the normalised reactance is:

$$\frac{X}{Z_0} = \frac{4\pi M}{3R^2\lambda_{gc}} \tag{3.36}$$

The corrected physical length of the cavity can then be given by the following [49]:

$$L_c = \frac{\lambda_g \nu}{2} - L_i, \quad \text{and} \tag{3.37}$$

$$L_i = \frac{\lambda_g \nu}{2}\left[\frac{1}{2\pi}\sum_i \tan^{-1}\frac{2X_i}{Z_0}\right] \tag{3.38}$$

where X_i/Z_0 are the normalised reactances of irises associated with a specific cavity mode. For small couplings the effect of the input iris is often much larger than that of the coupling irises and equation (3.38) can be approximated by:

$$L_i = \frac{\lambda_g v}{2}\left[\frac{\lambda_g^2}{2\lambda_0^2}\left(\sum_i M_i\right) + \frac{1}{2\pi}\tan^{-1}\frac{2X_{in/out}}{Z_0}\right] \tag{3.39}$$

where M_i are the coupling coefficients relating to a specific mode in the cavity. For multi-mode cavities the effects of the irises on all the modes must be determined and the largest correction factor is used in equations (3.38) or (3.39) to calculate the corrected length of the cavity.

3.5 FILTER DESIGN EXAMPLES

Two multi-mode waveguide filters were designed by means of the classical filter design method, built and tested. The first is a fourth order Chebyschev response filter constructed in two dual-mode cavities. The second is a sixth order pseudo-elliptical response filter constructed in three dual-mode cavities. Since the design procedure is the same in both cases, only the resulting filter and measurements of the first filter will be presented.

3.5.1 FOURTH ORDER CHEBYSCHEV RESPONSE DUAL-MODE FILTER

The design specifications of the filter call for a fourth order Chebyshev response filter with 2% bandwidth relative to a centre frequency on 10GHz and a desired pass-band reflection of 20dB. The filter was constructed using two dual-mode cavities supporting the TE_{111} degenerate modes. The degenerate modes were coupled by means of coupling screws and inter-cavity coupling was realised by a single centred rectangular iris as can be seen in figure 3.4.

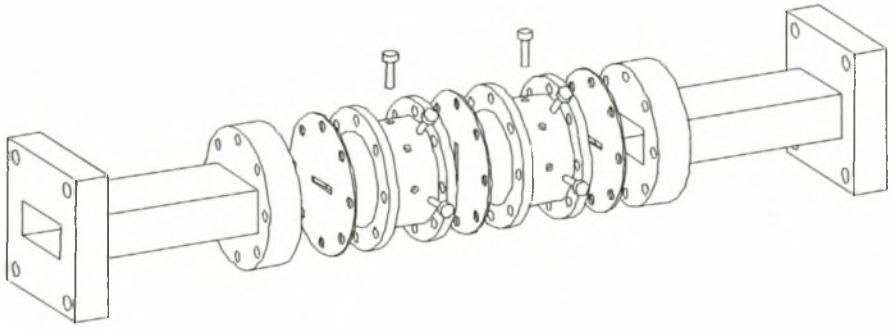

Figure 3.4: Fourth order Chebyschev response dual-mode filter

The in-band measurement of this filter is presented in figure 3.5 with the wide-band measurement given in figure 3.6. This measurement clearly shows the first spurious response at 11.5GHz, which is in good agreement with the theoretical prediction. Table 3.2 compares the measured results to the design specifications.

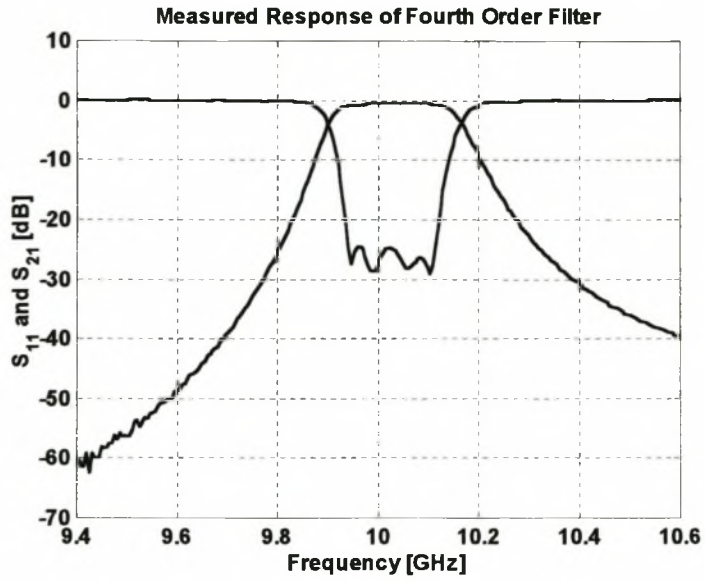

Figure 3.5: Measured response of fourth order filter

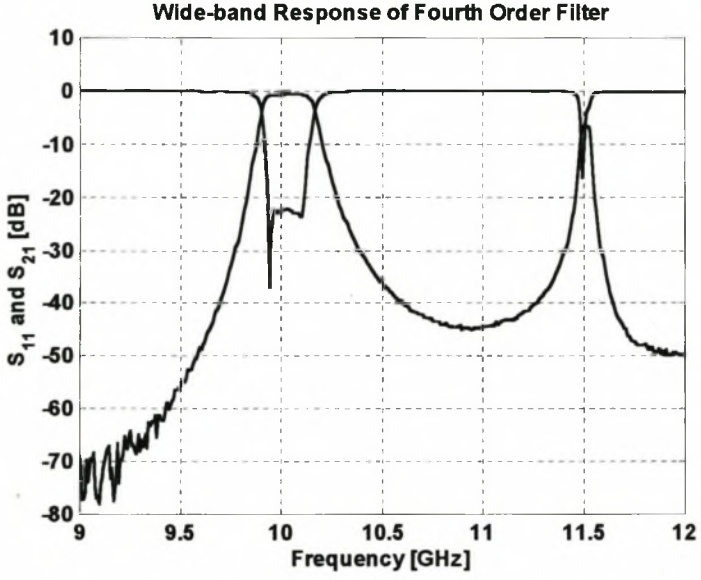

Figure 3.6: Wide-band response of fourth order filter

Table 3.2

Comparison of Measured Response and Design Specifications

	Desired	Measured	
Centre Frequency	10GHz	10.02GHz	
Bandwidth	2%	1.9%	1.6%
Reflection Loss in Passband	-20dB	-20dB	-24.5dB
Insertion Loss	0.3dB	0.55 dB	

3.5.2 SIXTH ORDER PSEUDO-ELLIPTICAL DUAL-MODE FILTER

This filter realises a sixth order pseudo-elliptical filter response in three dual-mode cavities. The cavities are fed through rectangular end-wall apertures by the TE_{10} mode in rectangular waveguide. The filter is constructed in cylindrical waveguide using the two degenerate TE_{111} modes in each cavity. These modes are coupled using coupling screws at $\phi = 45°$ and the inter-cavity couplings are realised by cross-shaped apertures. The design specifications are summarised in table 3.3.

Table 3.3
Design Specifications

Centre Frequency	10 GHz
Bandwidth	2 %
Reflection Loss in Passband	-20 dB
Minimum Attenuation in Stopband	50 dB

3.5.2.1 Filter Synthesis

A sixth order Chebyschev Real Function low-pass prototype filter function is used. In order to satisfy realisability conditions set forth by Rhodes [25] for dual-mode filters, two transmission zeros are chosen at infinity and a zero at $\omega_1 = 1.71 rad/s$. For a passband ripple of 0.05dB a ripple constant of $\varepsilon = 0.107608$ is chosen. This is the same prototype filter as was used as an example in the network synthesis chapter 2.6.2 and the final coupling matrix is taken as:

$$\mathbf{M} = \begin{bmatrix} 0 & 0.385957 & 0 & -0.728703 & 0 & 0 \\ 0.385957 & 0 & 0.640684 & 0 & 0 & 0 \\ 0 & 0.640684 & 0 & 0.561302 & 0 & -0.728703 \\ -0.728703 & 0 & 0.561302 & 0 & 0.640684 & 0 \\ 0 & 0 & 0 & 0.640684 & 0 & 0.385957 \\ 0 & 0 & -0.728703 & 0 & 0.385957 & 0 \end{bmatrix}$$

The coupling matrix and the network terminations are scaled by the bandwidth leaving the desired input/output and resonator couplings of table 3.4.

Table 3.4: Desired coupling elements of filter	
Lowpass Prototype	Bandpass: 2 % BW at 1 rad/s
R = 0.971507 Ω	R = 0.01943
$M_{12} = M_{56} = 0.385957$	$M_{12} = M_{56} = 0.007719$
$M_{23} = M_{45} = 0.640684$	$M_{23} = M_{45} = 0.012814$
$M_{34} = 0.561302$	$M_{34} = 0.011226$
$M_{14} = M_{36} = -0.728703$	$M_{14} = M_{36} = -0.014574$

3.5.2.2 Waveguide Dimensions

Standard X-band WR90 rectangular waveguide (dimensions a=22.86mm, b=10.16mm) is used to feed the filter. The cut-off wavelength of the TE_{10} mode in this guide is 6.557GHz. If the same cut-off frequency is chosen for the TE_{11} mode in the cylindrical cavity the cavity radius is 13.407mm. The uncorrected cavity length determined from equation (3.4) is 19.84mm. Using the mode chart in figure 3.2 this choice of diameter to length ratio results in a wide spurious free band with the first unwanted resonance occurring at 11.5GHz.

3.5.2.3 Iris Design

The external Q of the filter is related to the network terminations by equation (3.19)

$$Q_e = \frac{1}{R} = 51.4668$$

Using equation (3.22) the required magnetic polarisability of the input iris can be determined:

$$M^2 = \frac{abl^3\lambda_g 3R^2}{4\pi Q_e \lambda_0^{\,2}} = \left(2.5835\times10^{-7}\right)^2$$

where a = 22.86mm, b = 10.16mm, R = 13.407mm, ℓ = 19.84mm and λ_0 = 30mm. λ_g is the wavelength in the rectangular guide: $\lambda_g = \frac{\lambda_0}{\sqrt{1-\left(\frac{\lambda_0}{2a}\right)^2}} = 39.755\,\text{mm}$. The measured polarisabilities of Cohn, together with the correction factors given above are

used to determine the iris dimensions. Figure 3.7 shows the measured, corrected and desired magnetic polarisabilities of an iris of length 11.7mm and thickness 0.11mm.

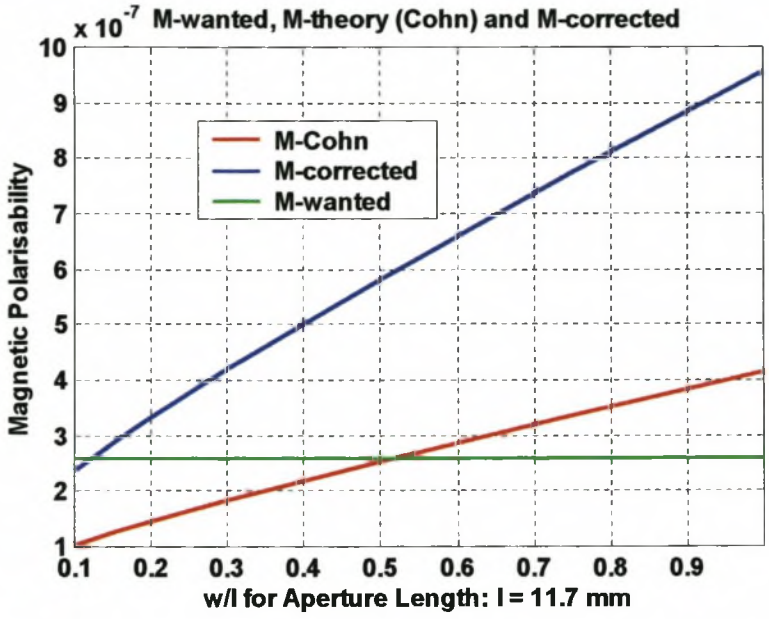

Figure 3.7: Magnetic polarisability of rectangular iris 11.7mm long, 0.11mm thick

From this graph the width of the aperture is determined as 1.383mm. A low width:length ratio is chosen because most of the approximations made in the derivation of the correction factors are more accurate for long thin irises.

As a result of the symmetry of the filter structure with $M_{23} = M_{45}$ and $M_{14} = M_{36}$ the two irises will be identical. For the coupling coefficients the required magnetic polarisabilities can be calculated from equation (3.18). For each iris a graph similar to that in figure 3.7 can be used to determine the dimensions of an iris capable of providing the required polarisabilities. Table 3.5 provides a summary of the iris dimensions.

Table 3.5

Final Dimensions of Irises

Iris Thickness	Input and Output Irises		Coupling M_{23} and M_{45}		Coupling M_{14} and M_{36}	
	Length	Width	Length	Width	Length	Width
0.11mm	11.7mm	1.383mm	8.5mm	1.126mm	8.8mm	1.13mm

3.5.2.4 Correction to Cavity Lengths

The physical length of each cavity must be adjusted to account for the resonant frequency change due to irises and the addition of the coupling and tuning screws. For the input and output irises, the normalised reactance (x/Z_0) is given by equation (3.36). The length correction to the first and last cavities due to the iris is therefore:

$$\Delta l_1 = \left(\frac{\lambda_{gc}}{4\pi}\right)\tan^{-1}\left(\frac{2x}{Z_0}\right)$$
$$= 0.93125\text{mm}$$

where λ_{gc} is the wavelength in the cylindrical cavity. For the cylindrical to cylindrical waveguide junction the normalised reactance is given by equation (3.24). The length correction for M_{23} and M_{45} is:

$$\Delta l_2 = \left(\frac{\lambda_{gc}}{4\pi}\right)\tan^{-1}\left(\frac{2x}{Z_0}\right)$$
$$= 0.2223\text{mm}$$

and the length correction for M_{14} and M_{36} is $\Delta l_3 = 0.2571\text{mm}$. A further length correction of 2% is included for the effect of the coupling and tuning screws. The corrected length of the resonator cavities 1 and 3, and cavity 2 is therefore:

$$l^{1,3}{}_{corrected} = l - \Delta l_1 - \Delta l_3 - 0.02l \qquad l^{2}{}_{corrected} = l - 2\Delta l_3 - 0.02l$$
$$= 18.255 \qquad = 18.929$$
$$\approx 18.3\text{mm} \qquad \approx 18.9\text{ mm}$$

Figure 3.8 shows the sixth order filter with the positions of the coupling and the tuning screws with a photograph of the manufactured filter shown in figure 3.9.

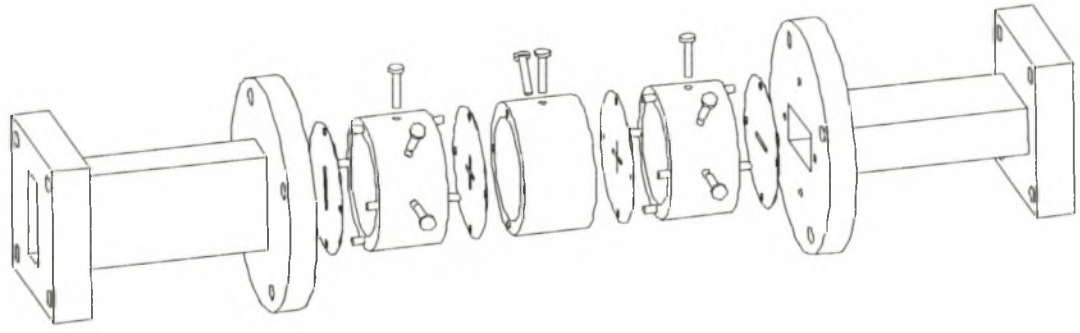

Figure 3.8: Sixth order pseudo-elliptical dual-mode filter

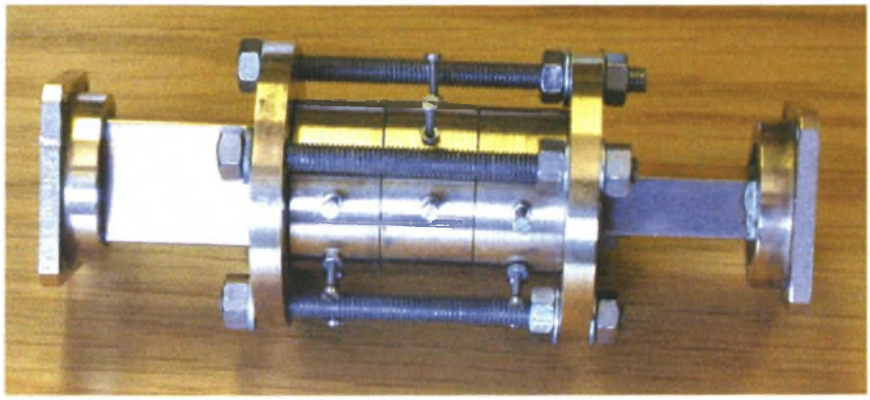

Figure 3.9: Photograph of Sixth order pseudo-elliptical dual-mode filter

The measured in-band and wide-band results of this filter can be seen in figures 3.10 and 3.11 respectively.

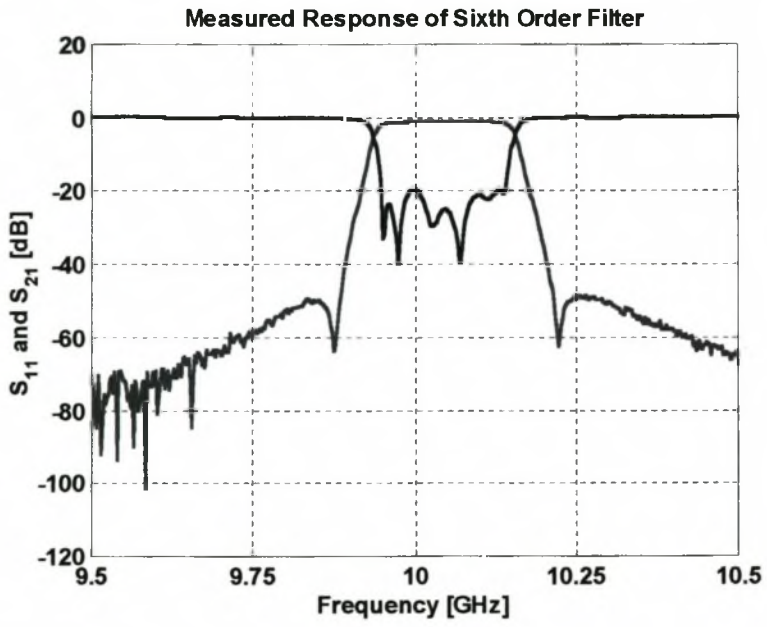

Figure 3.10: Measured response of sixth order pseudo-elliptic dual-mode filter

Table 3.6

Comparison of Measured Response and Design Specifications

	Desired	Measured
F_0	10 GHz	10.05 GHz
Bandwidth	2 %	1.92 %
Reflection Loss in Passband	-20 dB	-20 dB
Minimum Attenuation in Stopband	50 dB	50 dB
Insertion Loss	0.4 dB	0.85 dB

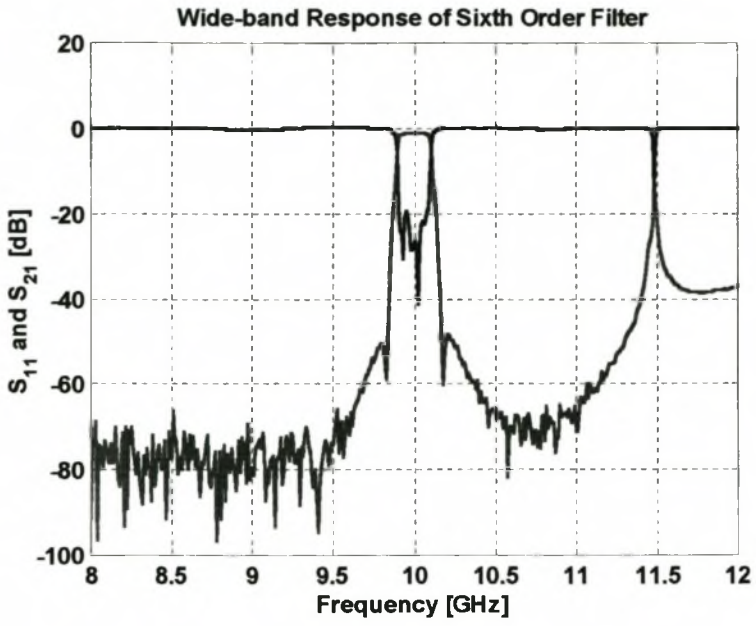

Figure 3.11: Measured wide-band response of sixth order pseudo-elliptic filter

The measured responses agree very well with the theoretical predictions and table 3.6 summarises the results.

3.6 CONCLUSION

The design techniques presented in this chapter have been used extensively in design of multi-mode coupled cavity filters. The techniques were derived from electromagnetic theory, network theory and empirical models.

Two multi-mode filters were designed using these classical design procedures. The filters were manufactured and from measurements, it is clear that the classical filter design techniques can still be used to design high performance microwave filter components.

The following chapter introduces measurement methods used for tuning and analysis of manufactured filters. Some of the methods are shown to be well suited to use in CAD procedures.

Chapter 4

Measurement Techniques

4.1 INTRODUCTION

Measurement and tuning form an integral part of the design and manufacture of multiple-coupled cavity filters. Even though EM-simulators and computers are becoming more advanced, the complexities of design and manufacture and tolerances of practical microwave filters still require the use of tuning elements to fine-tune the filter characteristics. In multi-mode cavity filter design, a number of novel contributions have been made in an attempt to avoid the use of tuning and coupling screws [47, 50]. The reason for this is two-fold. Firstly, tuning a complex microwave filter is usually very time-consuming and costly. Secondly, tuning and coupling screws introduce unwanted loss to the filter [51]. While the focus of this thesis is on the design and analysis of multi-mode cavity filters, an investigation into the use of measurement techniques provides insight into the nature of coupled resonators. Some of the techniques also lend themselves to EM-analysis and is extensively used as such in this work.

Measurement and tuning techniques can be divided into three main groups. The first consists of methods that use knowledge of reflection properties of an equivalent circuit to determine the coupling coefficients between resonators and, in some cases, the resonant frequencies of the resonators. The second group fits an equivalent circuit to the measured filter response by means of optimisation, while the third comprises methods that include time-domain techniques.

4.2 TUNING BY REFLECTION MEASUREMENT

4.2.1 OPEN AND SHORT CIRCUIT TUNING (DISHAL)

The well-known method by Dishal [52] is in most cases the basis for this group of techniques. Dishal uses the fact that a number of detuned coupled resonators will either appear as a short or an open circuit. By using a polar representation of the

reflection measurement, resonators can be tuned sequentially by observing the 180° phase change from either a short to open circuit, or an open to a short circuit as each resonator is tuned to the correct centre frequency. This method can be used to tune resonators, but gives no coupling coefficient information. Resonators are also tuned one by one, assuming that resonators and tuning elements have no effect on each other.

4.2.2 CALCULATING COUPLING COEFFICIENTS FROM REFLECTION PHASE MEASUREMENTS (ATIA AND WILLIAMS)

An expansion of Dishal's technique including determination of coupling coefficients was presented by Atia and Williams [53] and has been used extensively. The method is based on the input impedance characteristics of the short-circuited multiple-coupled cavity filter equivalent circuit of figure 4.1.

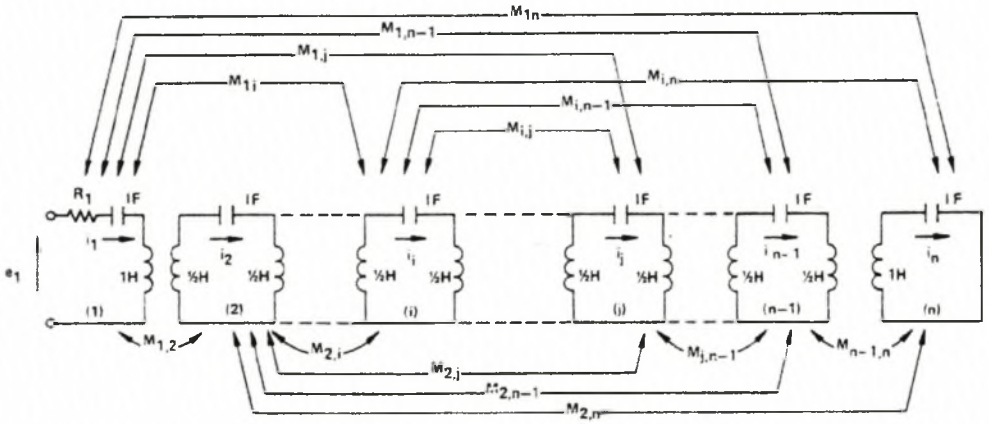

Figure 4.1: Equivalent circuit of short-circuited multiple-coupled cavity filter

Using the coupling matrix description of this circuit developed in chapter 2, the input impedance of this circuit can be found as:

$$Z_{11}^{(n)} = \frac{\det\left(j\lambda\mathbf{I} - j\mathbf{M}_n\right)}{\det\left(j\lambda\mathbf{I} - j\mathbf{M}_{n-1}\right)} \tag{4.1}$$

where $\mathbf{M}_{n-1}$ is the matrix resulting from deleting the first row and column of $\mathbf{M}_n$, $\lambda = j(\omega - 1/\omega)$ and $\mathbf{I}$ is the identity matrix. The poles and zeros of $Z_{11}^{(n)}$ are the eigenvalues of $\mathbf{M}_{n-1}$ and $\mathbf{M}_n$ respectively. The reflection coefficient, S_{11}, which is easily measured, is related to the input impedance by:

$$S_{11}^{(n)} = \frac{Z_{11}^{(n)} - R}{Z_{11}^{(n)} + R} \tag{4.2}$$

From this relation it is clear that the 0° and 180° phase positions of the reflection coefficient correspond exactly to the poles and zeros of the input impedance. Using equation (4.1) and conditions for synchronous tuning of the resonators, the coupling coefficients can be determined. In the case of three coupled cavities, the typical return loss phase is plotted in figure 4.2.

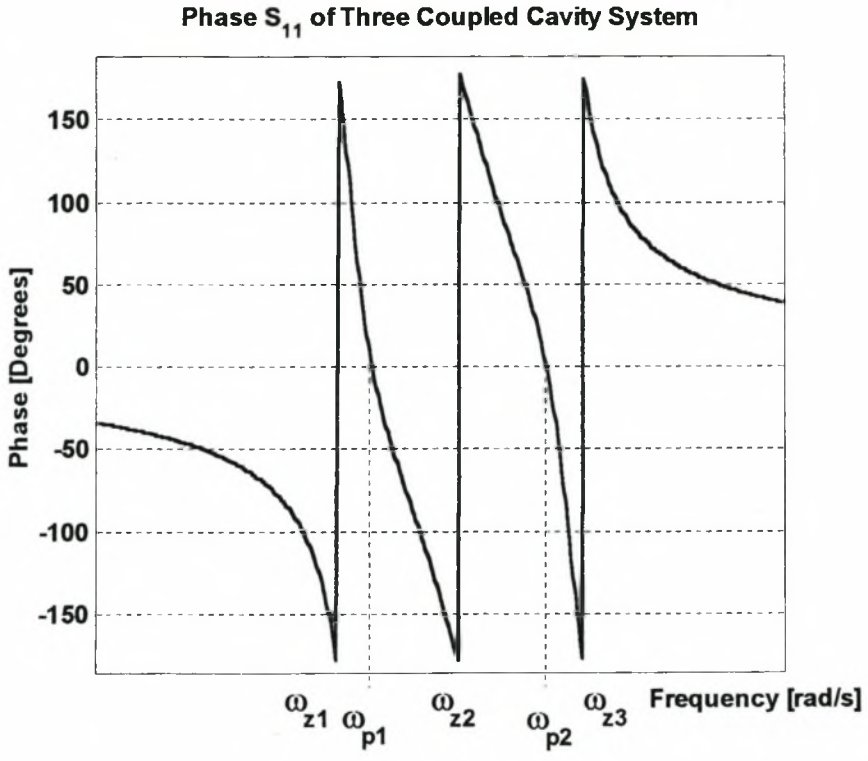

Figure 4.2: Phase of reflection coefficient of third order coupled cavity system

The conditions for synchronous tuning are [53].

$$\begin{aligned} \omega_{z2} &= \omega_0 \\ \omega_{z2} - \omega_{z1} &= \omega_{z3} - \omega_{z2} \\ \omega_{z2} - \omega_{p1} &= \omega_{p2} - \omega_{z2} \end{aligned} \tag{4.3}$$

With $\lambda = \left(\frac{\omega}{\omega_0} - \frac{\omega_0}{\omega} \right) \cong \frac{2}{\omega_0}(\omega - \omega_0)$ the input impedance is:

$$Z_{11}^{(3)} = j \frac{\lambda^3 - \lambda\left(M_{23}^2 + M_{12}^2\right)}{\lambda^2 - M_{23}^2} \tag{4.4}$$

and the coupling coefficients are:

$$M_{23} = \frac{\left(\omega_{p1} - \omega_{p2}\right)}{\omega_0}$$
$$M_{12} = \frac{\sqrt{\left(\omega_{z1} - \omega_{z3}\right)^2 - \left(\omega_{p1} - \omega_{p2}\right)^2}}{\omega_0} \tag{4.5}$$

Coupling coefficients of higher order coupled cavity systems can be determined by following the same procedure. A further improvement on this technique presented by Williams et al [54] includes the calculation of the network termination R_1 in figure 4.1 by measuring the frequencies at which the angle of the reflection coefficient is equal to 90°, for at these values:

$$R = \pm Z \tag{4.6}$$

The result is that the direct coupling coefficients and the network terminations can be calculated from a single measurement of the reflection coefficient. Although no information about the resonant frequencies of specific resonators is known, the filter can be tuned by correctly placing the 0° and 180° phase positions. The fact that this procedure is applied to a number of resonators simultaneously also means that the effects of tuning and coupling elements on neighbouring resonators can be readily seen and accounted for. The effect of finite unloaded Q of the resonators places a limit on the smallest coupling that can be measured accurately. McDonald [55] and Atia [53] show that if loss is taken into account, the coupling coefficient between two coupled cavities can be determined as:

$$M_{12}^2 = \frac{\left(\omega_{z1} - \omega_{z2}\right)^2}{\omega_0^{\,2}} + \frac{1}{Q_u^2} \tag{4.7}$$

In most cases the effect of loss can be ignored, but when the coupling is small, loss must be taken into account. Atia proposes an approximate rule that M must be at least $10(1/Q)$ for an error of less than 0.5%.

4.2.3 DETERMINING COUPLING COEFFICIENTS AND RESONANT FREQUENCIES (ATIA AND YAO)

Another technique presented by Atia and Yao [56] that also employs the phase of the reflection coefficient of the short-circuited coupled cavity structure, allows for the calculation of the resonant frequencies of individual resonators. For the equivalent circuit of figure 4.3 the input impedance of loop i when resonator n is terminated in a

short circuit at reference plane *T-T*, can be determined from the following recursive equations:

$$Z_{in}^{(i)} = j\frac{Z_{0i}}{\omega\omega_{0i}}\frac{P_i(\omega^2)}{Q_i(\omega^2)}, \; i = 1, 2, \ldots, n \tag{4.8}$$

where

$$P_{i+1}(\omega^2) = Q_i(\omega^2), \; i = 1, 2, \ldots, n\text{-}1 \tag{4.9}$$

$$m_{i,i+1}^2\omega^2 Q_{i+1}(\omega^2) = (\omega^2 - \omega_{0i}^2)P_{i+1}(\omega^2) - P_i(\omega^2) \; i = 1, 2, \ldots, n\text{-}1 \tag{4.10}$$

and

$$m_{i,i+1}^2 = \omega_{0i}\omega_{0(i+1)}\frac{M_{i,i+1}^2}{Z_{0i}Z_{0(i+1)}} = \omega_{0i}\omega_{0(i+1)}k_{i,i+1}^2 \tag{4.11}$$

In the above equations ω_{0i} and Z_{0i} are the resonant frequencies and characteristic impedances of resonator i, and $m_{i,i+1}$ and $k_{i,i+1}$ are the coupling bandwidths and coupling coefficients respectively.

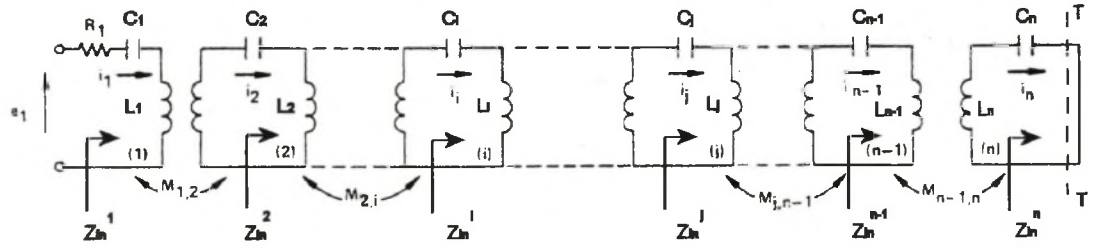

Figure 4.3: Equivalent circuit for calculation of coupling coefficients and resonator frequencies.

$P_i(\omega^2)$ and $Q_i(\omega^2)$, which are the zeros and poles of the input impedance of the one port network at loop i, can again be found from the 0° and 180° positions of the phase of the reflection coefficient:

$$\begin{aligned} P_i(\omega^2) &= \prod_{t=1}^{n-i+1}(\omega^2 - [\omega_{zt}^i]^2) \\ Q_i(\omega^2) &= \prod_{q=1}^{n-i}(\omega^2 - [\omega_{pq}^i]^2) \end{aligned}, \; i = 1, 2, \ldots, n\text{-}1 \tag{4.12}$$

where ω_z and ω_p have the same definitions as in section 4.2.2 above and can be found as in figure 4.2. Using the recursive relations the resonant frequencies of the network can be calculated as

$$\omega_{0i}^2 = \frac{\prod_{t=1}^{n-i+1}\left[\omega_{zt}^i\right]^2}{\prod_{q=1}^{n-i}\left[\omega_{pq}^i\right]^2}, \; i = 1, 2, \ldots, n \tag{4.13}$$

and the coupling coefficients of the network are given by.

$$m_{i,i+1}^2 = \sum_{t=1}^{n-i+1}\left[\omega_{zt}^i\right]^2 - \sum_{q=1}^{n-i}\left[\omega_{pq}^i\right]^2 - \omega_{0i}^2 \; , i = 1, 2, \ldots, n\text{-}1 \tag{4.14}$$

The value of the network termination R_1 in figure 4.3 can also be determined by using the frequency corresponding to $\pm 90°$ phase of the input reflection coefficient.

$$R_1 = \frac{Z_{01}}{\omega_{01}\omega_{90°}} \left| \frac{\prod_{t=1}^{n}\left(\omega_{90°}^2 - \left[\omega_{zt}^1\right]^2\right)}{\prod_{q=1}^{n-1}\left(\omega_{90°}^2 - \left[\omega_{pq}^1\right]^2\right)} \right| \tag{4.15}$$

The finite unloaded Q of the resonators also limits the accuracy of measuring small couplings.

Since all the information of a coupled cavity network, including coupling coefficients, resonator frequencies and network terminations, can be extracted from the reflection coefficient of the short-circuited network, this method can also be used for numerical analysis and design. The use of loss-less cavities in the analysis routine also negates the limitations imposed by finite resonator Q. Using the adaptive sampling and rational interpolation technique, a large number of frequency points can be generated efficiently, thereby increasing the accuracy of the method. Since this is a general method for cascaded coupled resonators without knowledge of the properties of the resonators, this method can be used to design coupled cavity structures employing cavities of different sizes supporting different resonant modes. It is also useful for the analysis and design of cavities that are resonant at different frequencies, such as is often required for asymmetric filters and the analysis of coupling to spurious modes and different channels in a multiplexer.

4.2.4 USE OF FILTER DELAY CHARACTERISTICS (NESS)

A problem with the measurement of phase characteristics of a waveguide filter is that the reference plane for measurement is usually not coincident with the input slot. This leads to a phase offset and inaccurate measurement results. Chen [57] proposes the introduction of two impedance inverters to account for the offset. Another method, that uses the delay characteristics of the input reflection coefficient of the short-circuited network, is presented by Ness [58] and Accatino [59]. The external Q of a cavity, which is the input coupling, is found to be directly proportional to the slope of the phase of the reflection coefficient at resonance, with resonance defined as the frequency at which the maximum of the phase slope occurs. With the group delay of the reflection coefficient defined as

$$\Gamma_d(\omega) = -\frac{\partial \phi}{\partial \omega} \tag{4.16}$$

where ϕ is the phase of S_{11} in radians and ω the angular frequency, the measurement reference plane can now be moved by adding waveguide phase $e^{j\beta l}$ to the input cavity measurement. The correct reference plane is found where the maximum of the group delay occurs at the -180° phase position of the reflection coefficient, as can be seen in figure 4.4.

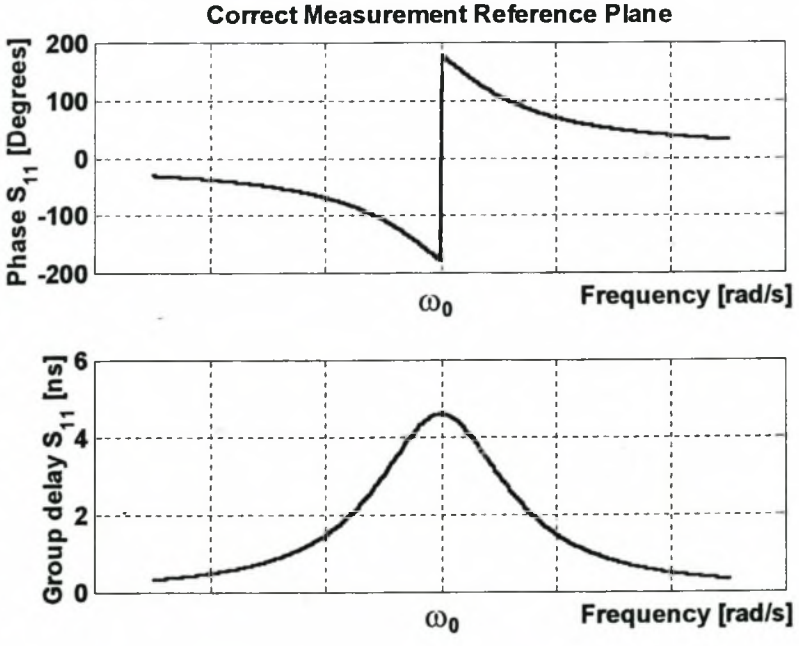

Figure 4.4: Reference plane set so that frequency of 180° phase coincides with maximum group delay

Ness [58] proceeds to derive equations relating the external Q of the input resonator and the coupling coefficients between synchronously tuned resonators, to the group delay of the reflection coefficient. For a single resonator the input coupling can be found as:

$$\Gamma_{d1}(\omega_0) = \frac{4Q_e}{\omega_0} \tag{4.17}$$

For two coupled cavities the result from equation (4.17) can be used to calculate the coupling coefficient:

$$k_{12} = \frac{4}{\omega_0 \sqrt{\Gamma_{d1}\Gamma_{d2}}} \tag{4.18}$$

where Γ_{d2} is the group delay of the coupled resonator structure at the centre frequency. Equations for higher order systems are also derived and presented [58]. While this method provides accurate results for lumped element networks, some errors are observed in measurement of waveguide filters. The reason for this is that the phase slope characteristics of various resonators differ and must be taken into accounted in the calculation of the network parameters. Another disadvantage of the procedure is that resonators must be tuned sequentially.

All the methods described above are unfortunately limited to the measurement of either directly coupled resonators, or systems where cross-coupling is relatively small. In many cases it is sufficient to tune the resonators and coupling coefficients of the filter first, without allowing cross-coupling. When the cross-coupling is small, inclusion thereof will have a very small effect on the resonator frequencies and only small adjustments will be required to fine-tune the filter response. For the direct determination of network parameters including cross-coupling, optimisation methods have been proposed.

4.3 OPTIMISATION TECHNIQUES IN MEASUREMENT

Measurement techniques in this section all adjust equivalent circuit descriptions of the filter under test to fit a measured response [60, 59, 61]. Deviations from the ideal solution can immediately be seen and corresponding tuning can be performed. This procedure is repeated until the extracted model matches the ideal equivalent circuit

and the filter is correctly tuned. The equivalent circuit used is basically the well-known equivalent circuit of the general multiple-coupled cavity filter, but to account for resonator detuning and loss, some adjustments have been made.

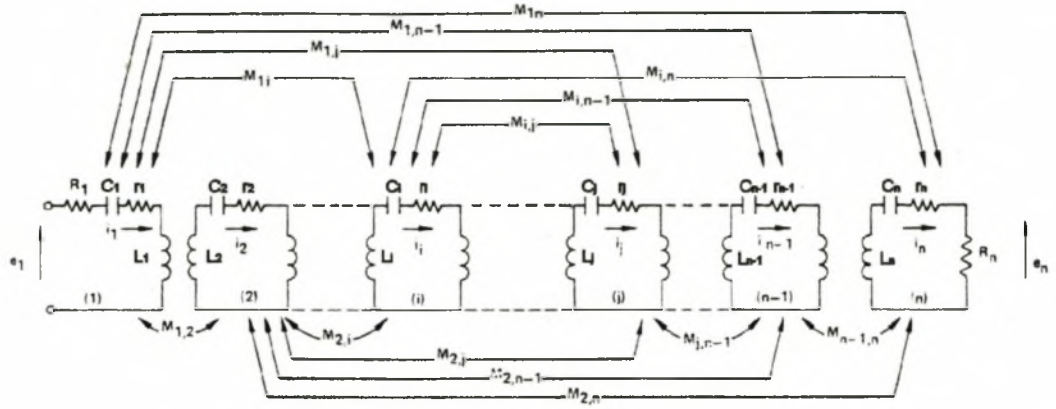

Figure 4.5: Equivalent circuit including detuned resonators and resonator loss

In the figure above ω_{0i} and Z_{0i} are the resonant frequencies and characteristic impedances of resonator i, and finite unloaded Q of resonators is included by providing r_i where $r_i = \frac{1}{Q_u \cdot BW}$ [57]. Asynchronous resonator frequencies can also be included by fixing C_i = L_i = 1 and ω_0 = 1, and allowing non-zero entries on the main diagonal of the coupling matrix. Writing loop equations for the first two coupled resonators of figure 4.5 results in the following impedance matrix:

$$Z = \begin{bmatrix} j\left(\omega L_1 - \frac{1}{\omega C_1}\right) + r_1 & jM_{12} \\ jM_{12} & j\left(\omega L_2 - \frac{1}{\omega C_2}\right) + r_2 \end{bmatrix} \tag{4.19}$$

Setting $C_i = L_i = 1$ and adding non-zero entries on the main diagonal result in:

$$Z = \begin{bmatrix} j\left(\omega - \frac{1}{\omega} + M_{11}\right) + r_1 & jM_{12} \\ jM_{12} & j\left(\omega - \frac{1}{\omega} + M_{22}\right) + r_2 \end{bmatrix} \tag{4.20}$$

At resonance the following equations must hold:

$$j\left(\omega_{01}-\frac{1}{\omega_{01}}+M_{11}\right)=0$$
$$j\left(\omega_{02}-\frac{1}{\omega_{02}}+M_{22}\right)=0 \tag{4.21}$$

so that the resonant frequencies of the resonators can be determined from equation (4.22).

$$\omega_{0i}=\frac{-M_{ii}+\sqrt{M_{ii}^2+4}}{2} \tag{4.22}$$

A positive M_{ii} indicates a resonant frequency that is lower than ω_0 = 1rad/s, and a negative M_{ii} indicates a resonant frequency that is higher than 1rad/s.

This method of determining the resonant frequencies of coupled resonators can be used in optimisation routines to fit the response of an equivalent circuit as in figure 4.5 to a measured filter response. Once the equivalent circuit has been extracted, specific filter elements can be tuned to obtain the ideal response. While many examples of practical filters tuned with this type of technique have been presented [60, 61], the starting positions of this tuning procedure are always close to the optimal solution. Even for lower order filters, a bad starting position will almost always result in a local minimum termination of the optimisation phase. Kahrizi et al [60] use a multi-level optimisation routine whereby the filter and equivalent circuit response is characterised by only the poles and zeros of transmission and reflection coefficients. This results in a more robust optimisation technique, but a good starting position is still required.

Another problem is that even if a minimum is found close to the global one, it may not be unique and great care must be taken to ensure that the mapping between the extracted equivalent circuit and the physical filter elements is correct. Atia and Williams [53] use the same rotation techniques as was introduced for the synthesis of multiple-coupled cavity filters to obtain the correct mapping.

This method can provide all necessary information required for tuning and includes cross-coupling and finite unloaded Q of resonators. The fact that the method is performed on the complete assembled filter, makes it a very good technique for the final fine-tuning of multiple-coupled cavity filters. Other techniques such as that presented by Atia and Yao in section 4.2.3 will be required to obtain a good starting

position. This method can also be used as a general technique for the numerical analysis and design of coupled cavity structures. Specific applications thereof will be treated in chapter 6.

4.4 OTHER METHODS

4.4.1 MEASUREMENT BY WEAK COUPLING

This technique also used by Couffignal et al [62] is a well-known and widely used technique for the measurement of input coupling to resonators and the coupling coefficient between coupled resonators. The two measurement configurations are shown in figures 4.6 and 4.7.

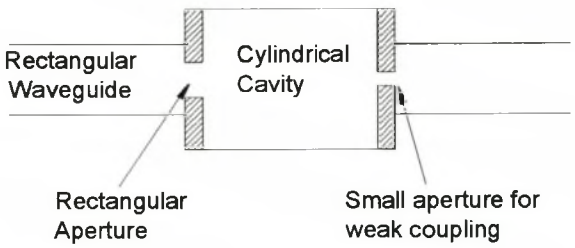

Figure 4.6: Measurement setup for input coupling measurement

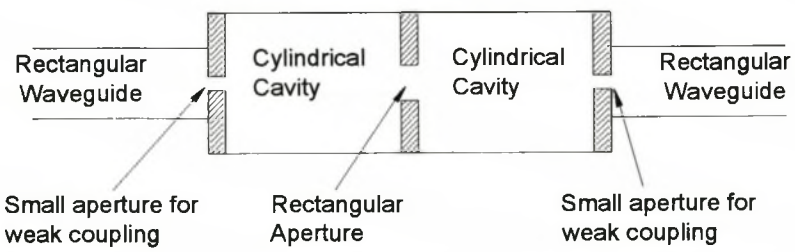

Figure 4.7: Measurement setup for coupling coefficient measurement

The transmission responses of the two measurement setups can be seen in figures 4.8 and 4.9. The input coupling can be determined from figure 4.8 as

$$R = \frac{1}{Q_e} = \frac{\Delta f}{f_0} \tag{4.23}$$

and the coupling coefficient between two coupled resonators from figure 4.9.

$$M_{12} = \frac{\Delta f}{f_0} \tag{4.24}$$

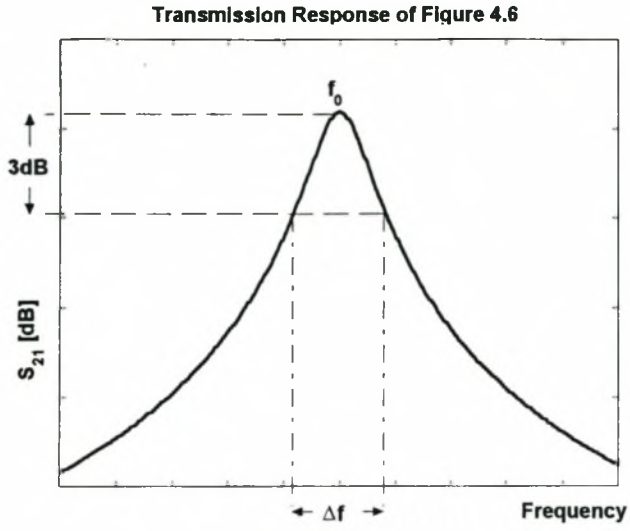

Figure 4.8: Transmission response of input coupling measurement

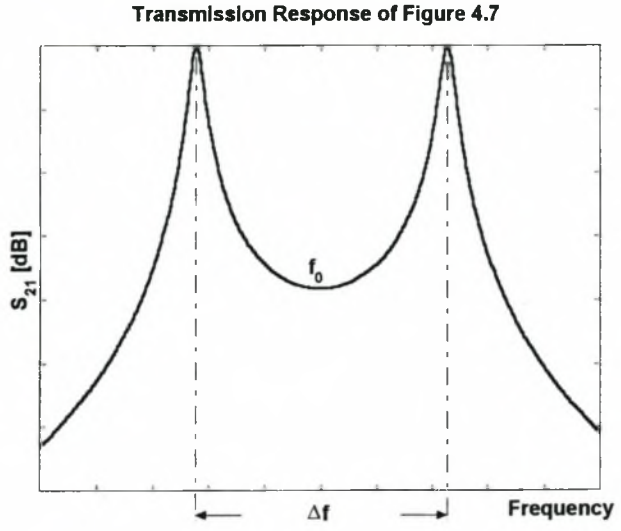

Figure 4.9: Transmission response of coupling coefficient measurement

In theory this method can also be used for the calculation of input/output and inter-cavity coupling coefficients in an EM-analysis. In practice, though, the use of very small irises to realise weak input coupling requires a very large number of cylindrical modes for the mode-matching technique to be accurate, making this method inefficient. Some cases where this has been used for EM-analysis [18, 62] will be discussed in more detail in the chapter dealing with EM-analysis techniques.

4.4.2 FILTER TUNING IN THE TIME DOMAIN

Filter tuning can also be accomplished by investigating time-domain characteristics of an all-pole filter [63]. Using a special type of Fourier transformation, the time domain response of the reflection coefficient of a correctly tuned filter produces a number of

characteristic peaks and nulls as can be seen in figure 4.10b. The nulls correspond to the individual resonators, while the peaks are an indication of the coupling coefficients between the resonators.

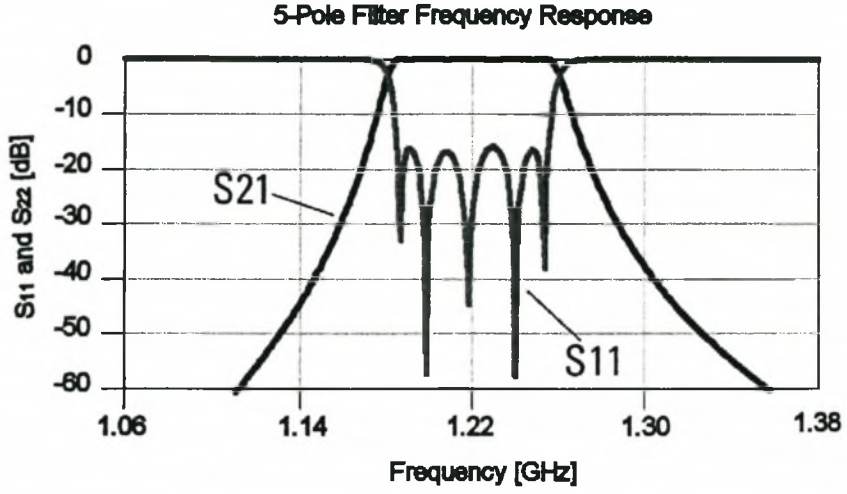

Figure 4.10a: Frequency response of 5-pole filter

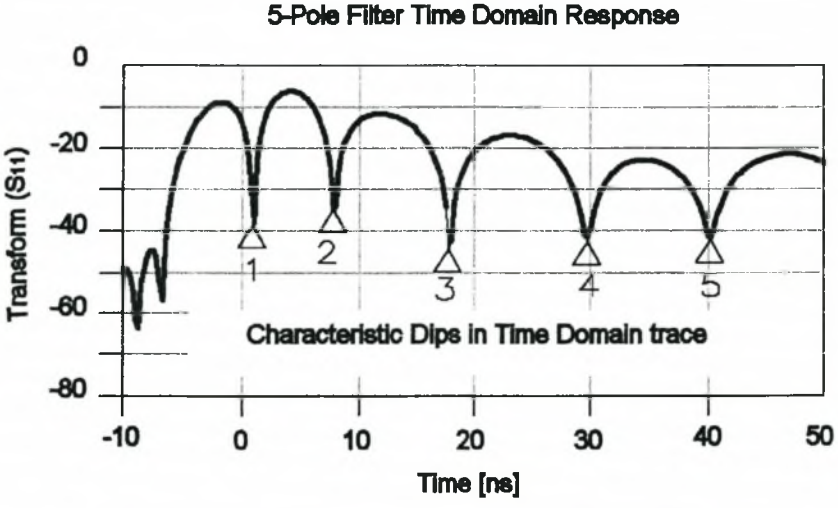

Figure 4.10b: Time domain response of 5-pole filter

The individual dips in the time domain response are only visible when the corresponding resonators are correctly tuned to the centre frequency of the filter. This method has also recently been extended to include tuning of filters with finite transmission zeros and asymmetrical frequency responses [64]. While this method can be used for tuning of multiple-coupled cavity filters, the actual resonator frequencies and coupling coefficients cannot be extracted, and is therefore not well suited to use in EM-analysis.

4.5 CONCLUSION

Measurement techniques play an integral part in the fine-tuning of multi-mode coupled cavity filters. This chapter presented methods used for tuning and evaluation of manufactured filters.

Two methods, in particular, were found to be well suited to use in CAD procedures. The first uses the phase of a reflection coefficient measurement to determine the coupling coefficients and resonant frequencies of the resonators. The second method uses direct optimisation of the equivalent circuit of the filter to fit the measured response. This procedure extracts all coupling coefficients, including coefficients of cross-coupling, and resonator frequencies.

This chapter concludes the discussion of standard classical and experimental design techniques, which form the basis of the CAD procedures developed later in the thesis. The following chapter presents three basic numerical tools used in the development of these CAD procedures.

Chapter 5

CAD Tools

5.1 INTRODUCTION

This chapter introduces the basic tools used in the design and analysis of microwave structures and components. Three main software techniques will be used in this work.

Of the many numerical techniques available for the analysis of such structures, the Mode-Matching technique is very well suited to waveguide problems where the magnetic and electric field expansions in terms of eigenmodes are known analytically. Arndt et al. [65] also notes that, for microwave components composed of cylindrical and rectangular waveguides such as transformers, filters, couplers and multiplexers, efficient mode-matching building blocks have been successfully demonstrated.

For the analysis of more complicated structures, space discretisation methods such as the three-dimensional finite element method (FEM), and the finite difference time domain method (FDTD) are typically used. Due to the vast differences in sizes of various components such as aperture size, iris thickness and cavity dimensions, to name but a few, very fine discretisation is required [66]. This leads to very high requirements for storage capacity and CPU power. Another shortcoming particularly of interest is the difficulties in determining resonant frequencies of cavities accurately. A lot of activity on this problem has been observed [11, 9, 67], but errors from the analytical solutions ranging from 0.5% to 5% are still published. These errors are unacceptable for narrow-band filter design, leaving the mode-matching method as the optimal choice. The specific formulation and use of this method in the context of this work is examined in section 2.

Even though the mode-matching technique is very efficient, generating EM-analyses at a large number of frequency points, such as for a full frequency response of a band-pass filter, is still time-consuming. Some of the analysis methods described in the CAD chapter, such as the method using the phase of the reflection coefficient, also require many frequency point evaluations to be accurate or at all useable. Section 3

investigates an efficient adaptive sampling algorithm [68] that, together with rational interpolation, significantly reduces the number of EM-analyses required for the design of microwave components.

Optimisation has become an essential part of the design of microwave devices. When optimisation is performed using an EM-simulator this process can be very time-consuming, especially when gradient-based optimisation is used. While this is often the preferred method, the error function gradient must be computed for each input parameter, resulting in many EM-evaluations with only very small perturbations about the starting point. Recently the space mapping technique [69] has proven to be very effective in minimising the number of EM-simulations required in the optimisation process by finding a link or map between two different models of the design problem. All the CPU-intensive optimisation is performed on a fast and simple model of the problem, while the EM-simulation is only used for the iterative validation of the map. The basic principles of this method are covered in section 4.

5.2 THE MODE-MATCHING TECHNIQUE

The mode-matching technique is a very well known and widely used technique for the analysis of microwave circuits, especially waveguide structures. The generalised scattering matrix (GSM), containing information of the scattering parameters of all incident modes on a waveguide discontinuity, is generated by this technique and is an important tool for design and analysis in a multimode waveguide environment.

According to the theory of the mode-matching method set forth in [12], the electric and magnetic fields in two regions sharing a common interface are expanded into a finite sum of fundamental modes. Although several formulations can be used to represent these modes on the surface, the TE-TM expansion is most commonly used [70]. The name of the method is derived from the matching of the tangential fields of these fundamental modes on each side of the shared surface. Using the orthogonality property of the modes, a set of linear independent equations can be found, relating the amplitudes of the incident modes to that of the reflected modes. With some mathematical manipulation, the GSM of the discontinuity can then be extracted.

For the increased efficiency of this technique, some special formulations are revisited. These include the use of a frequency independent coupling integral matrix, the line integral formulation, and the use of coupling matrix reduction and symmetry of the structure to reduce the computational effort of the technique.

5.2.1 FORMULATION

The formulation used here follows that of Omar and Schünemann [12] for the boundary reduction type problem as in figure 5.1, with the cylindrical region I the larger, and the rectangular region II the smaller. Slightly varying formulations for boundary enlargement and mixed type problems can also be derived [12].

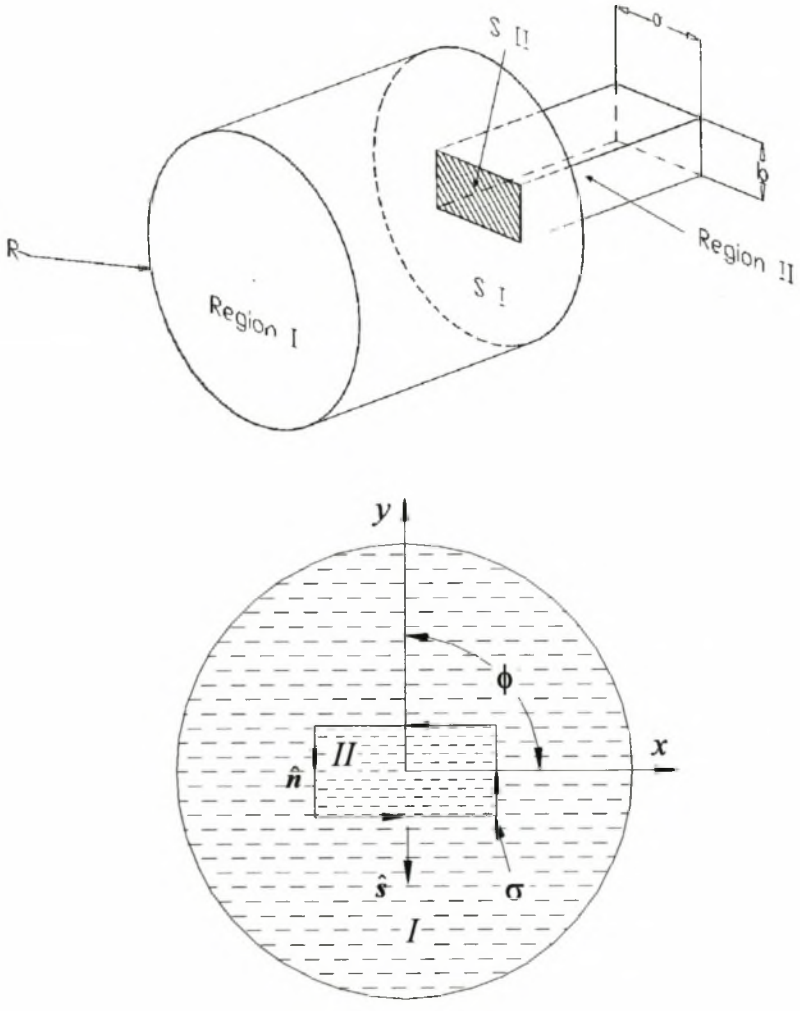

Figure 5.1: Cylindrical to Rectangular Waveguide step discontinuity.

The transverse electric and magnetic fields in each region are expanded in an infinite set of modes. This infinite set can be truncated as the solution to the problem converges.

$$
\begin{aligned}
\boldsymbol{E}_t^I(r,\phi,z) &= \sum_n \boldsymbol{e}_{t_n}^I(r,\phi)(a_n^I e^{-\gamma_n^I z} + b_n^I e^{+\gamma_n^I z}) \\
\boldsymbol{H}_t^I(r,\phi,z) &= \sum_n \boldsymbol{h}_{t_n}^I(r,\phi)(a_n^I e^{-\gamma_n^I z} - b_n^I e^{+\gamma_n^I z}) \\
\boldsymbol{E}_t^{II}(x,y,z) &= \sum_n \boldsymbol{e}_{t_n}^{II}(x,y)(a_n^{II} e^{+\gamma_n^{II} z} + b_n^{II} e^{-\gamma_n^{II} z}) \\
\boldsymbol{H}_t^{II}(x,y,z) &= \sum_n \boldsymbol{h}_{t_n}^{II}(x,y)(a_n^{II} e^{+\gamma_n^{II} z} - b_n^{II} e^{-\gamma_n^{II} z})
\end{aligned}
\tag{5.1}
$$

The transverse fundamental modes or eigenfunctions can be derived from the vector potentials:

$$
\begin{aligned}
\boldsymbol{\Pi}_{TE}(\boldsymbol{\rho},z) &= \Psi(\boldsymbol{\rho})e^{-\gamma z}\hat{\boldsymbol{i}}_z \\
\boldsymbol{\Pi}_{TM}(\boldsymbol{\rho},z) &= \Phi(\boldsymbol{\rho})e^{-\gamma z}\hat{\boldsymbol{i}}_z
\end{aligned}
\tag{5.2}
$$

$$
\begin{aligned}
\boldsymbol{e}_t &= j\omega\mu\hat{\boldsymbol{i}}_z \times \nabla_t \Psi - \gamma \nabla_t \Phi \\
\boldsymbol{h}_t &= -\gamma \nabla_t \Psi - j\omega\varepsilon\hat{\boldsymbol{i}}_z \times \nabla_t \Phi
\end{aligned}
\tag{5.3}
$$

where $\boldsymbol{\rho}$ is either $(\boldsymbol{x},\boldsymbol{y})$ or $(\boldsymbol{r},\boldsymbol{\phi})$, and Ψ and Φ are the TE and TM solutions to the Helmholtz equation satisfying the boundary equations in each waveguide respectively.

$$
\begin{aligned}
\Psi_{nl}^I(r,\phi) &= \frac{-P}{k_c} J_n(k_c r)\left(\cos n\phi + \sin n\phi\right) \\
\Phi_{nl}^I(r,\phi) &= \frac{P}{k_c} J_n(k_c r)\left(\cos n\phi + \sin n\phi\right)
\end{aligned}
\tag{5.4a}
$$

$$
\begin{aligned}
\Psi_{nl}^{II}(x,y) &= -Q\cos k_x x \cos k_y y \\
\Phi_{nl}^{II}(x,y) &= -Q\sin k_x x \sin k_y y
\end{aligned}
\tag{5.4b}
$$

$J_n(k_c r)$ is the Bessel function of the first kind, n and l are the mode indices. In the cylindrical guide $n = 0, 1, 2, \ldots$ and $l = 1, 2, 3, \ldots$. $k_c = \frac{p_{nl}}{R}$ with p_{nl} the l^{th} zero of the Bessel function of order n for the TM modes, and the derivative of the Bessel function of order n for the TE modes.

In the rectangular guide neither n nor l can be zero for the TM modes and $k_c^2 = \omega^2\mu\varepsilon + \gamma^2 = k_x^2 + k_y^2$, $k_x = \frac{n\pi}{a}$ and $k_y = \frac{l\pi}{b}$.

Solving the Helmholtz equation in the cylindrical guide provides both the cosine and the sine solutions of (5.4a), where both solutions coexist as degenerate modes for all $n > 0$. For $n = 0$ either the cosine or the sine solution is valid.

Expanding (5.3) fully provides the field distributions for the complete set of eigenfunctions in the cylindrical waveguide (5.5) and rectangular waveguide (5.6):

$$\begin{aligned}
\boldsymbol{e}_{TE}^{I} &= \frac{Pj\omega u}{k_c}\left(\frac{n}{k_c}\frac{J_n(k_c r)}{r}\sin n\phi\hat{\boldsymbol{i}}_r + J_n'(k_c r)\cos n\phi\hat{\boldsymbol{i}}_\phi\right) = \sqrt{Z_{TE}}\cdot\tilde{\boldsymbol{e}}_{TE}^{I} \\
\boldsymbol{h}_{TE}^{I} &= \frac{P\gamma}{k_c}\left(-J_n'(k_c r)\cos n\phi\hat{\boldsymbol{i}}_r + \frac{n}{k_c}\frac{J_n(k_c r)}{r}\sin n\phi\hat{\boldsymbol{i}}_\phi\right) = \sqrt{Y_{TE}}\cdot\tilde{\boldsymbol{h}}_{TE}^{I} \\
\boldsymbol{e}_{TM}^{I} &= \frac{P\gamma}{k_c}\left(-J_n'(k_c r)\cos n\phi\hat{\boldsymbol{i}}_r + \frac{n}{k_c}\frac{J_n(k_c r)}{r}\sin n\phi\hat{\boldsymbol{i}}_\phi\right) = \sqrt{Z_{TM}}\cdot\tilde{\boldsymbol{e}}_{TM}^{I} \\
\boldsymbol{h}_{TM}^{I} &= \frac{Pj\omega\varepsilon}{k_c}\left(-\frac{n}{k_c}\frac{J_n(k_c r)}{r}\sin n\phi\hat{\boldsymbol{i}}_r - J_n'(k_c r)\cos n\phi\hat{\boldsymbol{i}}_\phi\right) = \sqrt{Y_{TM}}\cdot\tilde{\boldsymbol{h}}_{TM}^{I}
\end{aligned} \tag{5.5a}$$

$$\begin{aligned}
\boldsymbol{e}_{TE}^{I} &= \frac{Pj\omega u}{k_c}\left(-\frac{n}{k_c}\frac{J_n(k_c r)}{r}\cos n\phi\hat{\boldsymbol{i}}_r + J_n'(k_c r)\sin n\phi\hat{\boldsymbol{i}}_\phi\right) = \sqrt{Z_{TE}}\cdot\tilde{\boldsymbol{e}}_{TE}^{I} \\
\boldsymbol{h}_{TE}^{I} &= \frac{P\gamma}{k_c}\left(-J_n'(k_c r)\sin n\phi\hat{\boldsymbol{i}}_r - \frac{n}{k_c}\frac{J_n(k_c r)}{r}\cos n\phi\hat{\boldsymbol{i}}_\phi\right) = \sqrt{Y_{TE}}\cdot\tilde{\boldsymbol{h}}_{TE}^{I} \\
\boldsymbol{e}_{TM}^{I} &= \frac{P\gamma}{k_c}\left(-J_n'(k_c r)\sin n\phi\hat{\boldsymbol{i}}_r - \frac{n}{k_c}\frac{J_n(k_c r)}{r}\cos n\phi\hat{\boldsymbol{i}}_\phi\right) = \sqrt{Z_{TM}}\cdot\tilde{\boldsymbol{e}}_{TM}^{I} \\
\boldsymbol{h}_{TM}^{I} &= \frac{Pj\omega\varepsilon}{k_c}\left(\frac{n}{k_c}\frac{J_n(k_c r)}{r}\cos n\phi\hat{\boldsymbol{i}}_r - J_n'(k_c r)\sin n\phi\hat{\boldsymbol{i}}_\phi\right) = \sqrt{Y_{TM}}\cdot\tilde{\boldsymbol{h}}_{TM}^{I}
\end{aligned} \tag{5.5b}$$

where $J_n'(k_c r) = \dfrac{\partial J_n(k_c r)}{\partial r}$.

$$\begin{aligned}
\boldsymbol{e}_{TE}^{II} &= \frac{Qj\omega u}{k_c^2}\left(k_y\cos k_x x\sin k_y y\hat{\boldsymbol{i}}_x - k_x\sin k_x x\cos k_y y\hat{\boldsymbol{i}}_y\right) = \sqrt{Z_{TE}}\cdot\tilde{\boldsymbol{e}}_{TE}^{II} \\
\boldsymbol{h}_{TE}^{II} &= \frac{Q\gamma}{k_c^2}\left(k_x\sin k_x x\cos k_y y\hat{\boldsymbol{i}}_x - k_y\cos k_x x\sin k_y y\hat{\boldsymbol{i}}_y\right) = \sqrt{Y_{TE}}\cdot\tilde{\boldsymbol{h}}_{TE}^{II} \\
\boldsymbol{e}_{TM}^{II} &= \frac{Q\gamma}{k_c^2}\left(-k_x\cos k_x x\sin k_y y\hat{\boldsymbol{i}}_x - k_y\sin k_x x\cos k_y y\hat{\boldsymbol{i}}_y\right) = \sqrt{Z_{TM}}\cdot\tilde{\boldsymbol{e}}_{TM}^{II} \\
\boldsymbol{h}_{TM}^{II} &= \frac{Qj\omega\varepsilon}{k_c^2}\left(k_y\sin k_x x\cos k_y y\hat{\boldsymbol{i}}_x - k_x\cos k_x x\sin k_y y\hat{\boldsymbol{i}}_y\right) = \sqrt{Y_{TM}}\cdot\tilde{\boldsymbol{h}}_{TM}^{II}
\end{aligned} \tag{5.6}$$

$$Z_{TE} = \frac{1}{Y_{TE}} = \frac{j\omega\mu}{\gamma} \quad \text{and} \quad Z_{TM} = \frac{1}{Y_{TM}} = \frac{\gamma}{j\omega\varepsilon}$$

Note that all the frequency information is contained in the impedance and admittance parts of (5.6). The constants P and Q are such that the power in each mode is normalised. According to [43] the normalisation is

$$\int_s \boldsymbol{e}_t \times \boldsymbol{h}_t^* \cdot \hat{\boldsymbol{i}}_z ds = \begin{cases} 1 & \text{Propagating mode} \\ 1\text{j} & \text{Non-propagating TE-mode} \\ -1\text{j} & \text{Non-propagating TM-mode} \end{cases}$$

The orthogonality properties of the modes over the cross section of each guide are standard and shown in equation (5.7).

$$\left.\begin{matrix} \int_s \tilde{\boldsymbol{e}}_{t_i}^I \times \tilde{\boldsymbol{h}}_{t_j}^I \cdot \hat{\boldsymbol{i}}_z ds \\ \int_s \tilde{\boldsymbol{e}}_{t_i}^{II} \times \tilde{\boldsymbol{h}}_{t_j}^{II} \cdot \hat{\boldsymbol{i}}_z ds \end{matrix}\right\} = \delta_{ij} \qquad , \delta_{ij} = \text{Kronecker delta} \tag{5.7}$$

Matching the transverse fields at the interface ($z = 0$) requires the following relations to hold:

$$\begin{aligned} \boldsymbol{E}_t^I &= \begin{cases} \boldsymbol{E}_t^{II} & \text{on } \mathrm{S^{II}} \\ 0 & \text{on } \mathrm{S^I - S^{II}} \end{cases} \\ \boldsymbol{H}_t^I &= \boldsymbol{H}_t^{II} \quad \text{on } \mathrm{S^{II}} \end{aligned} \tag{5.8}$$

By applying these boundary conditions and the orthogonality properties, and rewriting (5.1) the following relation can be derived [71]:

$$\begin{aligned} \boldsymbol{E}_t^I &= \sum_i \tilde{\boldsymbol{e}}_{t_i}^I \sqrt{Z_i^I}\,(a_i^I e^{-\gamma_i^I z} + b_i^I e^{+\gamma_i^I z}) = \sum_i \tilde{\boldsymbol{e}}_{t_i}^I V_i^I \\ \boldsymbol{H}_t^I &= \sum_i \tilde{\boldsymbol{h}}_{t_i}^I \sqrt{Y_i^I}\,(a_i^I e^{-\gamma_i^I z} - b_i^I e^{+\gamma_i^I z}) = \sum_i \tilde{\boldsymbol{h}}_{t_i}^I V_i^I \\ \boldsymbol{E}_t^{II} &= \sum_j \tilde{\boldsymbol{e}}_{t_j}^{II} \sqrt{Z_j^{II}}\,(a_j^{II} e^{+\gamma_j^{II} z} + b_j^{II} e^{-\gamma_j^{II} z}) = \sum_j \tilde{\boldsymbol{e}}_{t_j}^{II} V_j^{II} \\ \boldsymbol{H}_t^{II} &= \sum_j \tilde{\boldsymbol{h}}_{t_j}^{II} \sqrt{Y_j^{II}}\,(a_j^{II} e^{+\gamma_j^{II} z} - b_j^{II} e^{-\gamma_j^{II} z}) = \sum_j \tilde{\boldsymbol{h}}_{t_j}^{II} V_j^{II} \end{aligned} \tag{5.9}$$

$$\mathbf{V}^I = [\mathbf{W}]\mathbf{V}^{II} \quad , \text{with } W_{ij} = \iint_{S^{II}} \tilde{\boldsymbol{e}}_{t_j}^{II} \times \tilde{\boldsymbol{h}}_{t_i}^I \cdot \hat{\boldsymbol{i}}_z ds \tag{5.10}$$

Since both $\tilde{\boldsymbol{e}}$ and $\tilde{\boldsymbol{h}}$ are frequency independent, the resulting **W**-matrix is also frequency independent.

Equation (5.11) gives the expression of the GSM in terms of the modal amplitudes

$$\begin{bmatrix} \mathbf{b}^{I} \\ \mathbf{b}^{II} \end{bmatrix} = \begin{bmatrix} \mathbf{S}^{I,I} & \mathbf{S}^{I,II} \\ \mathbf{S}^{II,I} & \mathbf{S}^{II,II} \end{bmatrix} \begin{bmatrix} \mathbf{a}^{I} \\ \mathbf{a}^{II} \end{bmatrix} \tag{5.11}$$

The GSM entries can be found in terms of the **W**-matrix and the modal impedances and admittances from the following [71]:

$$\begin{aligned} [\mathbf{R}] &= diag\left(\sqrt{\mathbf{Y}^{I}}\right) \cdot [\mathbf{W}] \cdot diag\left(\sqrt{\mathbf{Z}^{II}}\right) \\ [\mathbf{T}] &= diag\left(\sqrt{\mathbf{Z}^{II}}\right) \cdot [\mathbf{W}]^{T} \cdot diag\left(\sqrt{\mathbf{Y}^{I}}\right) \end{aligned} \tag{5.12}$$

$$\begin{aligned} \left[\mathbf{S}^{I,I}\right] &= \left([\mathbf{R}][\mathbf{T}]+[\mathbf{I}]\right)^{-1} \cdot \left([\mathbf{R}][\mathbf{T}]-[\mathbf{I}]\right) \quad \left[\mathbf{S}^{I,II}\right] = 2\left([\mathbf{R}][\mathbf{T}]+[\mathbf{I}]\right)^{-1} \cdot [\mathbf{R}] \\ \left[\mathbf{S}^{II,I}\right] &= [\mathbf{T}]\left([\mathbf{I}]-\left[\mathbf{S}^{I,I}\right]\right) \qquad \left[\mathbf{S}^{II,II}\right] = [\mathbf{I}]-[\mathbf{T}]\left[\mathbf{S}^{I,II}\right] \end{aligned} \tag{5.13}$$

5.2.2 FINITE MODE SET AND CONVERGENCE

In practice the number of modes used in each mode set has to be truncated to a finite number with *N* modes retained in *I* and *M* modes in *II*. With the modes on each side of the junction ordered according to increasing wavenumber k_c, the assumption can be made that the effects of very high order modes (high values of k_c) can be discarded. The uniqueness of the GSM determined using either the finite or the infinite mode sets can be verified [72]. This truncation results in a residual error of the complete solution that can be controlled by increasing or decreasing the number of modes used in the analysis. While increasing the number of modes will always result in a more accurate solution, this also increases the computation time drastically. A compromise must therefore be made to find an acceptable solution with minimum computation time spent. Convergence of the solution must be monitored by evaluating the Mode-Matching solution while increasing the number of modes on both sides of the junction.

A very important relation *N*:*M* between the numbers of modes retained on either side of the junction can also be observed. When the number of modes on each side of the juction is large enough, the choice of mode ratio seems to have little effect. With a reduced mode set, however, an equal amount of modes may violate boundary conditions, resulting in inaccurate solutions [73, 72]. Literature provides some ratios for this purpose, including that the ratio *N*:*M* be the same as the ratio of the area of

region *I* to the area of region *II* [73]. Another method [74] suggests that for a cylindrical to rectangular junction the ratio $N{:}M = 2R{:}a$ should be used. Accatino [76], however shows that wavenumber of the highest order mode in the cylindrical guide should be equal to the highest wavenumber in the rectangular guide and in a convergence test this criterion clearly outperforms the method proposed in [74]. This corresponds to the requirement that the maximum field variation should be almost equal in both regions. Although convergence is found to be dependent on the rectangular aperture position in the cylindrical guide [74], in this work sufficient convergence is obtained by retaining the first 80 modes in the rectangular guide and then using the equality of wavenumbers criterion to set the number of modes in the cylindrical guide.

In most cases the **W**-matrices and GSM matrices contain many entries that are zero or close to zero. This means that a lot of numerical computation is done on matrices containing relatively little information. Vale [75] proposes a reduced **W**-matrix formulation derived from an equivalent circuit representation of the Mode-Matching equations. In this equivalent circuit the entries of the **W**-matrix represent transformer turn ratios of ideal transformers linking modes in the two waveguide regions. As a **W**-matrix entry (or specific transformer turn ratio) tends to zero, the transformer will look increasingly like a short circuit to a mode in region one, and an open circuit to a mode in region two. In the limit where the transformer turn ratio becomes zero, the modes are completely decoupled.

Applying this method to the problem of a centred rectangular aperture in a cylindrical waveguide, automatically extracts subsystems of decoupled W-matrices. These subsystems contain coupling information of independent coupling mode sets. The result is exactly the same as that reported by Accatino [76] where mode subsets are chosen beforehand on the basis of structural symmetry. The reduced size of the **W**-matrix and resulting matrices in (5.12) increases the speed of the calculation of the GSM entries in (5.13) significantly, while retaining the accuracy of the full **W**-matrix formulation.

In cylindrical to rectangular waveguide junction problems, the coupling integrals in (5.12) require surface integrals of Bessel functions that are not known analytically. The greatest computational effort is therefore in the numerical calculation of the **W**-

matrix. Since the reduced **W**-matrix formulation proposed by Vale [75] is applied on the complete **W**-matrix, this computational burden is not diminished as it would be by starting off with a reduced mode set. This mode set can be found by using the structural symmetry of the problem and by placing either a horizontal magnetic wall and vertical electric wall, or vertical magnetic wall and horizontal electric wall through the centre of the structure. In the cylindrical waveguide this amounts to retaining only either the $\cos(n\phi)$ or $\sin(n\phi)$ solutions in (5.3) with n odd.

With off-centred apertures, though, the structural symmetry vanishes, the **W**-matrices become less sparse as more cross-coupling between modes occurs, and the complete mode sets and **W**-matrices must be retained. This would also explain why more higher order modes are required for convergence of the Mode-Matching technique for off-centred apertures than for centred apertures [74].

5.2.3 FORMULATIONS FOR MULTIGUIDE JUNCTIONS AND CASCADED JUCTIONS

Dai [73] presents a simple expansion of the existing Mode-Matching formulation for the inclusion of a junction of one waveguide to a number of waveguides. The transverse electric and magnetic fields are expanded in terms of the eigenmodes in each waveguide. The modes in each guide are again normalised to carry unity complex power. Matching the transverse components of the fields on the junction at z=0 and using the orthogonality properties of the modes, an equation similar to (5.10) is found with K the number of multiguide junctions:

$$\mathbf{V}^I = [\mathbf{W}]\begin{bmatrix}\mathbf{V}^{II}\\ \mathbf{V}^{III}\\ .\\ .\\ \mathbf{V}^{K}\end{bmatrix}, \text{ with } \quad [\mathbf{W}] = \begin{bmatrix}\mathbf{W}^{I,II} & \mathbf{W}^{I,III} & . & . & \mathbf{W}^{I,K}\end{bmatrix}$$

$$W_{ij}^{I,II} = \iint_{S^{II}} \tilde{\boldsymbol{e}}_{t_j}^{II} \times \tilde{\boldsymbol{h}}_{t_i}^{I} \cdot \hat{\boldsymbol{i}}_z ds$$

$$W_{ij}^{I,III} = \iint_{S^{III}} \tilde{\boldsymbol{e}}_{t_j}^{III} \times \tilde{\boldsymbol{h}}_{t_i}^{I} \cdot \hat{\boldsymbol{i}}_z ds \qquad (5.14)$$

$$W_{ij}^{I,K} = \iint_{S^{IV}} \tilde{\boldsymbol{e}}_{t_j}^{K} \times \tilde{\boldsymbol{h}}_{t_i}^{I} \cdot \hat{\boldsymbol{i}}_z ds$$

This expanded coupling matrix together with (5.13) and (5.15) (the expanded version of (5.12)), results in a new GSM including scattering information for the eigenmodes in all the waveguides at the junction.

$$[\mathbf{R}] = diag\left(\sqrt{\mathbf{Y}^{I}}\right)\cdot[\mathbf{W}]\cdot diag\left(\left[\sqrt{\mathbf{Z}^{II}}\quad\sqrt{\mathbf{Z}^{III}}\quad\cdot\quad\cdot\quad\sqrt{\mathbf{Z}^{K}}\right]\right)$$
$$[\mathbf{T}] = diag\left(\left[\sqrt{\mathbf{Z}^{II}}\quad\sqrt{\mathbf{Z}^{III}}\quad\cdot\quad\cdot\quad\sqrt{\mathbf{Z}^{K}}\right]\right)\cdot[\mathbf{W}]^{T}\cdot diag\left(\sqrt{\mathbf{Y}^{I}}\right) \tag{5.15}$$

$$\begin{bmatrix}\mathbf{b}^{I}\\ \mathbf{b}^{II}\end{bmatrix} = \begin{bmatrix}\mathbf{S}^{I,I} & \mathbf{S}^{I,II}\\ \mathbf{S}^{II,I} & \mathbf{S}^{II,II}\end{bmatrix}\begin{bmatrix}\mathbf{a}^{I}\\ \mathbf{a}^{II}\end{bmatrix} \tag{5.16}$$

With the GSM entries as follows:

$$\begin{aligned}
&\left[\mathbf{S}^{I,I}\right] = \left([\mathbf{R}][\mathbf{T}]+[\mathbf{I}]\right)^{-1}\cdot\left([\mathbf{R}][\mathbf{T}]-[\mathbf{I}]\right), && \text{an } N\times N \text{ matrix}\\
&\left[\mathbf{S}^{I,II}\right] = 2\left([\mathbf{R}][\mathbf{T}]+[\mathbf{I}]\right)^{-1}\cdot[\mathbf{R}], && \text{a } (K\,.\,M)\times N \text{ matrix}\\
&\left[\mathbf{S}^{II,I}\right] = [\mathbf{T}]\left([\mathbf{I}]-\left[\mathbf{S}^{I,I}\right]\right), && \text{an } N\times (K\,.\,M) \text{ matrix and}\\
&\left[\mathbf{S}^{II,II}\right] = [\mathbf{I}]-[\mathbf{T}]\left[\mathbf{S}^{I,II}\right], && \text{a } (K\,.\,M)\times (K\,.\,M) \text{ matrix.}
\end{aligned} \tag{5.17}$$

In order to create waveguide structures such as irises and coupled cavity systems, the GSMs of the junctions and waveguide sections must be cascaded. This is achieved by progressively cascading GSM sections until the GSM of the complete structure remains. The derivation of the cascading equations of two GSMs *A* and *B* is available in literature [77] and only the resulting formulas are given in (5.18)

$$\begin{aligned}
\left[\mathbf{S}^{I,I}\right] &= \left[\mathbf{S}_{A}^{I,I}\right]+\left[\mathbf{S}_{A}^{I,II}\right]\left([\mathbf{I}]-\left[\mathbf{S}_{B}^{I,I}\right]\left[\mathbf{S}_{A}^{II,II}\right]\right)^{-1}\left[\mathbf{S}_{B}^{I,I}\right]\left[\mathbf{S}_{A}^{II,I}\right]\\
\left[\mathbf{S}^{I,II}\right] &= \left[\mathbf{S}_{A}^{I,II}\right]\left([\mathbf{I}]-\left[\mathbf{S}_{B}^{I,I}\right]\left[\mathbf{S}_{A}^{II,II}\right]\right)^{-1}\left[\mathbf{S}_{B}^{I,II}\right]\\
\left[\mathbf{S}^{II,I}\right] &= \left[\mathbf{S}_{B}^{II,I}\right]\left([\mathbf{I}]-\left[\mathbf{S}_{A}^{II,II}\right]\left[\mathbf{S}_{B}^{I,I}\right]\right)^{-1}\left[\mathbf{S}_{A}^{II,I}\right]\\
\left[\mathbf{S}^{II,II}\right] &= \left[\mathbf{S}_{B}^{II,II}\right]+\left[\mathbf{S}_{B}^{II,I}\right]\left([\mathbf{I}]-\left[\mathbf{S}_{A}^{II,II}\right]\left[\mathbf{S}_{B}^{I,I}\right]\right)^{-1}\left[\mathbf{S}_{A}^{II,II}\right]\left[\mathbf{S}_{B}^{I,II}\right]
\end{aligned} \tag{5.18}$$

Although a large number of modes are required at the junctions, only a few higher order modes are required in the homogeneous waveguide sections connecting the junctions. This is due to the strong attenuation of the non-propagating higher order modes. Arndt [65] reports that as few as two higher order modes are required in some cases.

5.2.4 TRANSFORMING THE COUPLING INTEGRALS TO LINE INTEGRALS

The coupling integrals derived in the above formulation require surface integrals of Bessel functions that are not known analytically. As the number of cylindrical modes increases, so does the complexity of the surface to be integrated, increasing the computation time of numerical integration exponentially. Gentili [70] presents a technique, also employed by [76] and [65], whereby the surface integrals can be transformed to line integrals, significantly reducing the computation time of the coupling integrals. While the same result as in [70] is obtained, a more direct derivation is presented here, starting from the familiar equation (5.10).

Noticing that the frequency independent parts of (5.3) can be found from

$$\begin{aligned} \tilde{\boldsymbol{e}}_{TE}^{I} &= \nabla\Phi^{I} \times \hat{\boldsymbol{i}}_z & \tilde{\boldsymbol{e}}_{TE}^{II} &= \nabla\Phi^{II} \times \hat{\boldsymbol{i}}_z \\ \tilde{\boldsymbol{h}}_{TE}^{I} &= \nabla\Phi^{I} & \tilde{\boldsymbol{h}}_{TE}^{II} &= \nabla\Phi^{II} \\ \tilde{\boldsymbol{e}}_{TM}^{I} &= \nabla\Psi^{I} & \tilde{\boldsymbol{e}}_{TM}^{II} &= \nabla\Psi^{II} \\ \tilde{\boldsymbol{h}}_{TM}^{I} &= \nabla\Psi^{I} \times \hat{\boldsymbol{i}}_z & \tilde{\boldsymbol{h}}_{TM}^{II} &= \nabla\Psi^{II} \times \hat{\boldsymbol{i}}_z \end{aligned} \tag{5.14}$$

the coupling integrals can be rewritten:

$$W_{ij} = \iint_{S^{II}} \tilde{\boldsymbol{e}}_{t_j}^{II} \times \tilde{\boldsymbol{h}}_{t_i}^{I} \cdot \hat{\boldsymbol{i}}_z ds = \iint_{S^{II}} \left(\nabla\Phi_j^{II} \times \hat{\boldsymbol{i}}_z\right) \times \nabla\Phi_i^{I} \cdot \hat{\boldsymbol{i}}_z ds \qquad \text{TE}^{\text{I}} - \text{TE}^{\text{II}} \qquad (5.15a)$$

$$= \iint_{S^{II}} \nabla\Psi_j^{II} \times \left(\nabla\Psi_i^{I} \times \hat{\boldsymbol{i}}_z\right) \cdot \hat{\boldsymbol{i}}_z ds \qquad \text{TM}^{\text{I}} - \text{TM}^{\text{II}} \qquad (5.15b)$$

$$= \iint_{S^{II}} \left(\nabla\Phi_j^{II} \times \hat{\boldsymbol{i}}_z\right) \times \left(\nabla\Psi_i^{I} \times \hat{\boldsymbol{i}}_z\right) \cdot \hat{\boldsymbol{i}}_z ds \qquad \text{TM}^{\text{I}} - \text{TE}^{\text{II}} \qquad (5.15c)$$

$$= \iint_{S^{II}} \nabla\Psi_j^{II} \times \nabla\Phi_i^{I} \cdot \hat{\boldsymbol{i}}_z ds \qquad \text{TE}^{\text{I}} - \text{TM}^{\text{II}} \qquad (5.15d)$$

Letting σ be the boundary of S^{II}, $\hat{\boldsymbol{n}}$ the unit vector defined along σ pointing outward, and $\hat{\boldsymbol{s}}$ the unit vector in the direction tangent to σ (taken counter-clockwise), the following Green's first identities hold [70]:

$$\begin{aligned}\int_{S^{II}} \nabla\Phi\cdot\nabla\Psi ds &= \oint_{\sigma} \Phi\nabla\Psi\cdot\hat{\boldsymbol{n}}dl - \int_{S^{II}} \Phi\nabla\cdot\nabla\Psi ds \\ &= \oint_{\sigma} \Psi\nabla\Phi\cdot\hat{\boldsymbol{n}}dl - \int_{S^{II}} \Psi\nabla\cdot\nabla\Phi ds\end{aligned} \tag{5.16}$$

$$\iint_{S^{II}} \nabla\Phi\cdot\nabla\Psi\times\hat{\boldsymbol{i}}_z ds = \oint_{\sigma} \Phi\nabla\Psi\cdot\hat{\boldsymbol{s}}dl = -\oint_{\sigma} \Psi\nabla\Phi\cdot\hat{\boldsymbol{s}}dl \tag{5.17}$$

and the Helmholtz equation gives

$$\begin{aligned}\nabla\cdot\nabla\Phi_n &= -k_n^2\Phi_n \\ \nabla\cdot\nabla\Psi_n &= -\kappa_n^2\Psi_n\end{aligned} \tag{5.18}$$

Together with the vector identity $\mathbf{A}\times(\mathbf{B}\times\mathbf{C}) = -(\mathbf{B}\times\mathbf{C})\times\mathbf{A} = \mathbf{B}(\mathbf{A}\cdot\mathbf{B}) - \mathbf{C}(\mathbf{A}\cdot\mathbf{B})$, equation (15a) can be rewritten as:

$$\iint_{S^{II}} \left(\nabla\Phi_j^{II}\times\hat{\boldsymbol{i}}_z\right)\times\nabla\Phi_i^{I}\cdot\hat{\boldsymbol{i}}_z ds = \iint_{S^{II}} \left(\hat{\boldsymbol{i}}_z\left(\nabla\Phi_j^{II}\cdot\nabla\Phi_i^{I}\right) - \nabla\Phi_i^{I}\left(\nabla\Phi_j^{II}\cdot\hat{\boldsymbol{i}}_z\right)\right) \tag{5.19}$$

where the second term on the right vanishes. Using (5.16) and (5.17) two equations are derived from (5.19)

$$\begin{aligned}\iint_{S^{II}} \left(\nabla\Phi_j^{II}\cdot\nabla\Phi_i^{I}\right) ds &= \oint_{\sigma} \Phi_j^{II}\nabla\Phi_i^{I}\cdot\hat{\boldsymbol{n}}ds + \iint_{S^{II}} \Phi_j^{II}k_i^{I^2}\Phi_i^{I} da \\ &= \oint_{\sigma} \Phi_i^{I}\nabla\Phi_j^{II}\cdot\hat{\boldsymbol{n}}ds + \iint_{S^{II}} \Phi_i^{I}k_j^{II^2}\Phi_j^{II} da\end{aligned} \tag{5.20}$$

From these two equations the surface integral can be eliminated leaving:

$$W_{ij}^{TE-TE} = \frac{k_i^{I^2}\oint_{\sigma}\Phi_i^{I}\nabla\Phi_j^{II}\cdot\hat{\boldsymbol{n}}ds - k_j^{II^2}\oint_{\sigma}\Phi_j^{II}\nabla\Phi_i^{I}\cdot\hat{\boldsymbol{n}}ds}{k_i^{I^2} - k_j^{II^2}} \tag{5.21}$$

As (5.15b) is very much of the same form as (5.15a), the derivation for (5.15b) follows the same principle resulting in:

$$W_{ij}^{TM-TM} = \frac{\kappa_i^{I^2}\oint_{\sigma}\Psi_i^{I}\nabla\Psi_j^{II}\cdot\hat{\boldsymbol{n}}ds - \kappa_j^{II^2}\oint_{\sigma}\Psi_j^{II}\nabla\Psi_i^{I}\cdot\hat{\boldsymbol{n}}ds}{\kappa_i^{I^2} - \kappa_j^{II^2}} \tag{5.22}$$

The derivation for (5.15c) uses the following vector identitiy:

$(\mathbf{A}\times\mathbf{B})\times(\mathbf{C}\times\mathbf{D}) = (\mathbf{A}\times\mathbf{B}\cdot\mathbf{D})\mathbf{C} - (\mathbf{A}\times\mathbf{B}\cdot\mathbf{C})\mathbf{D}$ to find (5.23) where the second term on the right again vanishes.

$$\begin{aligned}&\iint_{S^{II}}\left(\nabla\Phi_j^{II}\times\hat{\boldsymbol{i}}_z\right)\times\left(\nabla\Psi_i^{I}\times\hat{\boldsymbol{i}}_z\right)\cdot\hat{\boldsymbol{i}}_z ds = \\ &\iint_{S^{II}}\left(\left(\nabla\Phi_j^{II}\times\hat{\boldsymbol{i}}_z\cdot\nabla\Psi_i^{I}\right)\hat{\boldsymbol{i}}_z - \left(\nabla\Phi_j^{II}\times\hat{\boldsymbol{i}}_z\cdot\hat{\boldsymbol{i}}_z\right)\nabla\Psi_i^{I}\right)\cdot\hat{\boldsymbol{i}}_z ds\end{aligned} \tag{5.23}$$

Using equation (5.17) now directly leaves:

$$\begin{aligned}W_{ij}^{TM-TE} &= -\oint_{\sigma}\Psi_i^{I}\nabla\Phi_j^{II}\cdot\hat{s}ds \\ &= \oint_{\sigma}\Phi_j^{II}\nabla\Psi_i^{I}\cdot\hat{s}ds\end{aligned} \tag{5.24}$$

Examination of (5.15d) reveals that the integrand vanishes over the area resulting in

$$W_{ij}^{TE-TM} = 0 \tag{5.25}$$

Equations (5.22) to (5.25) can now be used to determine the **W**-matrix entries. The line integrals require much less computational effort than the original surface integrals.

5.3 ADAPTIVE SAMPLING AND RATIONAL INTERPOLATION

The main purpose of rational interpolation and adaptive sampling techniques is to reduce the number of EM-evaluations required for the analysis of microwave structures [68]. The function of rational interpolation is to interpolate between the evaluation points chosen by the sampling method (support points), with the resulting approximation in the form of a ratio of two polynomials. The adaptive sampling algorithm determines the optimal positions for the support points at which to perform an electromagnetic evaluation (EM-evaluation), thereby minimising the number of evaluations required to approximate the response accurately.

5.3.1 RATIONAL INTERPOLATION

The rational interpolation formulation defines a function $\Re$ of variable f as a ratio of polynomials:

$$\Re(f)=\frac{\sum_{k=0}^{\xi} p_k f^k}{\sum_{k=0}^{\upsilon} q_k f^k}=\frac{N_\xi(f)}{D_\upsilon(f)} \tag{5.26}$$

with ξ the order of the numerator and υ the order of the denominator polynomials, and p_k and q_k the polynomial coefficients. Assuming that $\Re(f)$ exists and choosing q_0 arbitrarily, leaves $\xi + \upsilon + 1$ unknown coefficients that can only be determined from a set of $M+1=\xi+\upsilon+1$ support points with coordinates (f_i, S_i). Once determined, $\Re(f)$ will be a curve passing through the support point coordinates with $i = 0, 1, 2, \ldots, M$. The interpolation function can be calculated by means of a three-term recursion formula [68].

$$\left.\begin{aligned} N_k(\gamma)&=\varphi_k(\gamma_k,\gamma_{k-1},\cdots,\gamma_0)N_{k-1}(\gamma)+(\gamma-\gamma_{k-1})N_{k-2}(\gamma)\\ D_k(\gamma)&=\varphi_k(\gamma_k,\gamma_{k-1},\cdots,\gamma_0)D_{k-1}(\gamma)+(\gamma-\gamma_{k-1})D_{k-2}(\gamma)\end{aligned}\right\} \quad k=2,3,\cdots,N$$
$$\Re_k(\gamma)=\frac{N_k(\gamma)}{D_k(\gamma)} \qquad k=0,1,\cdots,N \tag{5.27}$$

The inverse differences $\varphi_k(\gamma_k,\gamma_{k-1},\cdots,\gamma_0)$, determined recursively from the support points (equation 5.28), are the partial denominators of a continued fraction that represents $\Re_k(\gamma)$.

$$\varphi_k(\gamma_i,\gamma_0)\equiv\frac{\gamma_i-\gamma_0}{S_i-S_0}\ , \quad i=1,2,\cdots,N$$
$$\varphi_k(\gamma_k,\gamma_{k-1},\cdots,\gamma_0)\equiv\frac{\gamma_i-\gamma_{k-1}}{\varphi_{k-1}(\gamma_i,\gamma_{k-2},\cdots,\gamma_0)-\varphi_{k-1}(\gamma_{k-1},\gamma_{k-2},\cdots,\gamma_0)} \tag{5.28}$$

where $i = k, k+1, \ldots, N$ and $k = 2, 3, \ldots, N$.

The calculation of roots of characteristic functions is a problem often encountered in the design of microwave structures. Lehmensiek [68] applied adaptive sampling to the problem of calculating the propagation constants of two- and three-layer shielded planar structures, where the existence of poles in the characteristic equation creates significant problems for most root-finding algorithms. The use of rational interpolation, though, results in $\Re(f)$ being defined as a ratio of polynomials. In order to find the roots of $\Re(f)$, only the roots of the numerator polynomial must be

calculated. This is a trivial problem and can be obtained by using any available root-finding algorithm.

5.3.2 ERROR ESTIMATION AND ADAPTIVE SAMPLING

In general, rational interpolation can be used to approximate $\Re(f)$ accurately over the frequency range (f_1, f_2) if enough support points are used. In order to calculate the optimal position of these support points, and thereby minimise their number, an adaptive sampling algorithm must be able to estimate the error over the interval of interest.

The rational interpolation formulation as used in [68] shows a natural residual term

$$E_k(f) = \frac{\left|\Re_k(f) - \Re_{k-1}(f)\right|}{1 + \left|\Re_k(f)\right|} \tag{5.29}$$

that can be used to estimate the interpolation error. This error function decreases as the order of the interpolation function increases, and is zero at the support points. The procedure by which the adaptive sampling algorithm works is as follows: Support points at f_1, f_2, and an arbitrary f_3 in the interval (f_1, f_2) are chosen. Equations (5.26) to (5.29) are used to calculate $\Re(f)$ and the estimated error for a large number of frequency points over the range (f_1, f_2). The next support point can now be placed at the maximum of the estimated error, and the procedure is repeated until the estimated error has been reduced to a sufficiently low value.

This is a very efficient procedure since the error is estimated in a natural way. The adaptive algorithm automatically selects and minimises the number of unequally spaced support points without any *a priori* knowledge of the function it is modelling.

In the calculation of coupling coefficients in coupled cavity structures, this has proven to be of great benefit. Because of the greatly decreased computation time, very small coupling coefficients in a multi-mode environment can now be calculated accurately. Methods that have previously almost exclusively been used for measurement and tuning can be used in EM analysis and design.

5.4 THE SPACE MAPPING TECHNIQUE

The concept of space mapping [69] has become a well-known method for minimising the number of EM-evaluations required in the optimisation phase of microwave design. Different models, a "coarse" model and a "fine" model, of the same microwave structure can often be found. The "coarse" model (typically an EM-simulator) is assumed to be very accurate, but computationally very expensive. The "coarse" model is not as accurate, but very simple, fast to compute and well suited to iterative optimisation techniques. A "coarse" model can be an equivalent circuit description, an empirical model or a less accurate EM-solution. The space mapping technique provides a link between the different models and thereby combines the computational efficiency of empirical models and the accuracy of EM-simulators. In some cases, an optimal design solution is found with less CPU effort than is usually required for one detailed frequency response EM-simulation [78].

The initial formulation of the method [69] requires a number of EM-evaluations to achieve an optimal starting point by gaining upfront information of the EM-model. This was found to be redundant and an improved technique "aggressive space mapping" where each EM-simulation is used to update the link between the models, was later presented [78]. This method is used extensively in this work and will now be discussed in more detail.

5.4.1 AGGRESSIVE SPACE MAPPING

Let the optimisation space and the associated coarse model input parameters be denoted by $\mathbf{X}_{os}$ and $\boldsymbol{x}_{os}$ respectively, with the EM-space and the fine model input parameters denoted by $\mathbf{X}_{em}$ and $\boldsymbol{x}_{em}$ respectively. The response vectors of the two vector spaces as a result of the input vectors are then defined as $\mathbf{R}_{os}(\boldsymbol{x}_{os})$ and $\mathbf{R}_{em}(\boldsymbol{x}_{em})$. $\boldsymbol{x}_{os}^{*}$ is the input vector that produces the optimal response in the optimisation space and is determined by means of conventional optimisation techniques. The task of the optimisation procedure is to find a non-linear vector function $\mathbf{P}$ that maps the input parameters of the fine model onto the input parameters of the coarse model

$$\boldsymbol{x}_{os} = \mathbf{P}(\boldsymbol{x}_{em}) \tag{5.30}$$

so that the responses of the two models are the same

$$\mathbf{R}_{os}(\mathbf{P}(\boldsymbol{x}_{em})) \approx \mathbf{R}_{em}(\boldsymbol{x}_{em}) \tag{5.31}$$

P is not known analytically and is found through a recursive procedure using a quasi-Newton iteration in conjunction with first-order derivative approximations updated by the classic Broyden formula. The basic procedure is as follows [78]:

Define a set of non-linear equations:

$$\mathbf{f}(\boldsymbol{x}_{em})=\mathbf{P}(\boldsymbol{x}_{em})-\boldsymbol{x}_{os}^{*} \tag{5.32}$$

After each new EM-analysis conventional optimisation on the coarse model finds the optimal input parameter vector producing the same response vector from the coarse model as was determined by the fine model analysis. This is called the parameter extraction phase of the routine. From (5.30) it is clear that $\mathbf{f}(\boldsymbol{x}_{em})$ becomes progressively smaller or $\mathbf{f}\left(\boldsymbol{x}_{em}^{j+1}\right)\rightarrow 0$. A quasi-Newton iteration is used to solve the set of non-linear equations. Assuming that f can be linearised locally, the next iteration will leave:

$$\boldsymbol{x}_{em}^{j+1}=\boldsymbol{x}_{em}^{j}+\mathbf{h}^{j} \tag{5.33}$$

where $\mathbf{h}^{j}$ solves the linear system in (5.34). This follows from a Taylor expansion of **f** about $\boldsymbol{x}_{em}^{j}$.

$$\mathbf{B}^{j}\mathbf{h}^{j}=-\mathbf{f}\left(\boldsymbol{x}_{em}^{j}\right) \tag{5.34}$$

B approximates the Jacobian matrix (5.35) and is updated using the Broyden formula in (5.36):

$$\mathbf{J}\left(\boldsymbol{x}_{em}^{j}\right)=\left[\frac{\partial \mathbf{f}^{T}(\boldsymbol{x}_{em})}{\partial \boldsymbol{x}_{em}}\right]^{T}\Bigg|_{\boldsymbol{x}_{em}=\boldsymbol{x}_{em}^{j}} \tag{5.35}$$

$$\mathbf{B}^{j+1}=\mathbf{B}^{j}+\frac{\mathbf{f}\left(\boldsymbol{x}_{em}^{j+1}\right)\left[\mathbf{h}^{j}\right]^{T}}{\left[\mathbf{h}^{j}\right]^{T}\mathbf{h}^{j}} \tag{5.36}$$

The recursive procedure can then be implemented as follows:

Initialisation

$$\boldsymbol{x}_{em}^{1}=\boldsymbol{x}_{os}^{*}$$

$\mathbf{B}^1 = \mathbf{I}$ (identity matrix)

$\mathbf{f}\left(\boldsymbol{x}_{em}^1\right) = \mathbf{P}(\boldsymbol{x}_{em}^1) - \boldsymbol{x}_{os}^*$

$j = 1$

Stop if $\left\|\mathbf{f}\left(\boldsymbol{x}_{em}^1\right)\right\| \leq \delta$

Iteration j

Solve $\mathbf{B}^j\mathbf{h}^j = -\mathbf{f}\left(\boldsymbol{x}_{em}^j\right)$ for $\mathbf{h}^j$

Set $\boldsymbol{x}_{em}^{j+1} = \boldsymbol{x}_{em}^j + \mathbf{h}^j$

Compute $\mathbf{f}$ from $\mathbf{f}\left(\boldsymbol{x}_{em}^{j+1}\right) = \mathbf{P}\left(\boldsymbol{x}_{em}^{j+1}\right) - \boldsymbol{x}_{os}^*$

Stop if $\left\|\mathbf{f}\left(\boldsymbol{x}_{em}^1\right)\right\| \leq \delta$

Update $\mathbf{B}^j$ to $\mathbf{B}^{j+1}$

Set $j = j + 1$ and go to next iteration

Some assumptions made are critical to the success of this procedure:

- $\mathbf{X}_{os}$ and $\mathbf{X}_{em}$ have the same dimensionality
- $\boldsymbol{x}_{os}$ and $\boldsymbol{x}_{em}$ describe the same physical parameters
- $\mathbf{P}$ exists and for a given $\boldsymbol{x}_{em}$, $\boldsymbol{x}_{os}$ can always be extracted using conventional optimisation techniques in the $\mathbf{X}_{os}$ space.

In the scope of this work, the aggressive space mapping optimisation routine is extensively used for the design of coupling and input-output irises. During this process, though, some failures of the method have been observed with the last assumption being the main culprit. Care must be taken to ensure that the initial response vectors of the fine and coarse models do not differ too much. This will result in very bad starting positions for the consequent optimisations of the coarse model, leading to non-optimal solutions of the parameter extraction phase. More information regarding the different coarse and fine models used in various applications and increase of design efficiency using the aggressive space mapping technique will be presented where used in specific applications.

5.5 CONCLUSION

This chapter presented the three main numerical tools used in this thesis. The mode-matching routine was introduced for cylindrical to rectangular waveguide discontinuities. This formulation makes use of a frequency independent coupling integral matrix that is only calculated once for a given geometry. Since the coupling integral must be calculated numerically, the faster surface- to line-integral conversion was also adopted.

The adaptive sampling algorithm was shown to be very useful in reducing the number of EM-evaluations over a frequency band of interest. The advantage of a rational interpolation model will also be used in the following chapter to find the natural resonant frequencies of coupled cavity structures in a very efficient way.

Aggressive space mapping was introduced for optimisation of microwave structures. The use of this method minimises the number of EM-evaluations required in the optimisation phase of CAD procedures.

The following chapter presents the development of CAD procedures for iris design in multi-modal coupled cavity applications. This chapter is the crux of the thesis where three new efficient CAD algorithms are presented for specific classes of iris design problems. These algorithms are used extensively in later chapters for the design of a quadruple-mode diplexer and new triple-mode cavity filter without coupling screws.

Chapter 6

CAD Procedures for Iris Design

6.1 INTRODUCTION

As discussed in chapter 1, the current techniques for iris design have a number of problems and limitations. This chapter brings together all the techniques discussed in the preceding sections, to present the development of three new integrated CAD procedures for the design of irises in a multi-mode waveguide environment. These procedures constitute the main thrust of this work, and form the basis with which the novel structures of the following chapters are designed.

The first CAD procedure is an enhancement of the standard numerical iris design technique whereby the natural resonant frequencies of a coupled cavity structure is used to determine the coupling coefficients [20]. This procedure presents an efficient solution to the design of irises separating identical cavities, where no cross-coupling between propagating modes is observed. In this work, the term 'cross-coupling' is used to denote coupling between modes of unequal indices, as well as coupling between TE and TM modes.

A second CAD procedure is developed for design of irises where cross-coupling between propagating modes exists, and resonant frequencies of cross-coupled modes are in close proximity. The complete iris structure is analysed and the equivalent circuit coupling matrix description, introduced in chapter 2, is optimised to fit the mode-matching response. The non-uniqueness problem often encountered in the optimisation phase is overcome by iteratively updating the direct coupling coefficient terms to match those determined from the iris equivalent reactance. This process ensures that all coupling coefficients and resonator frequencies are extracted accurately.

The third CAD procedure is for the design of irises separating non-identical or asynchronously tuned cavities. This procedure can also be used in the presence of cross-coupling, providing that the modes are not resonant at the same frequency. The

basis of this technique is the measurement method whereby the coupling coefficients and resonant frequencies are determined from the phase of the reflection coefficient.

6.2 CAD PROCEDURE 1: IRIS DESIGN FOR IDENTICAL CAVITIES WITH NO CROSS-COUPLING

The derivation of the standard procedure follows from the analysis of the equivalent circuit of two identical coupled cavities as shown in figure 6.1.

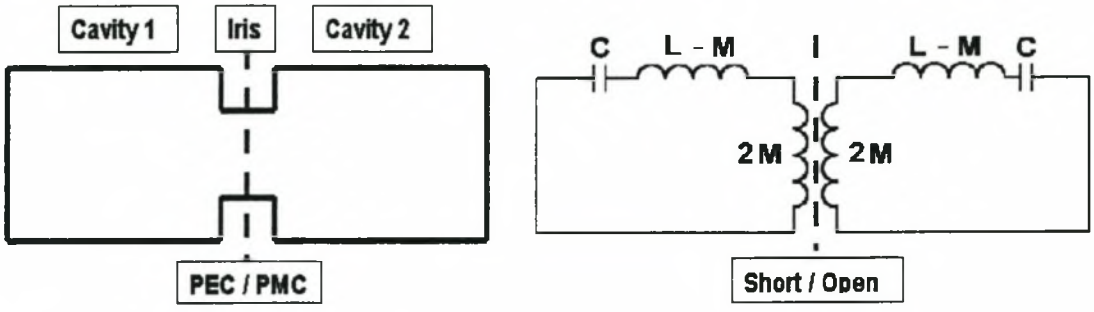

Figure 6.1: Equivalent circuit of two coupled cavities

Placing either a perfect electric (PEC) or magnetic conductor (PMC) in the centre of the iris, at the symmetry plane of the structure, corresponds to either a short circuit or an open circuit in the symmetry plane of the equivalent circuit. Solving for the resonant frequencies of the circuit with either the short or open circuit in place, results in two natural resonant frequencies of the coupled resonator structure.

$$f_e = \frac{1}{2\pi\sqrt{C(L-M)}}$$
$$f_m = \frac{1}{2\pi\sqrt{C(L+M)}} \qquad (6.1)$$

where f_e corresponds to the electric wall or short circuit and f_m corresponds to the magnetic wall or open circuit. f_e is the higher of the two and is only slightly lower than the resonant frequency of the unperturbed cavity. With the coupling coefficient defined as $K = \frac{M}{L}$, the equations in (6.1) can be manipulated to obtain a relation between the resonant frequencies and the coupling coefficient:

$$K = \frac{f_e^2 - f_m^2}{f_e^2 + f_m^2} \tag{6.2}$$

For small coupling coefficients, the centre frequency of the coupled resonator circuit can be approximated by equation (6.3) where a coupling coefficient of 0.1 results in an error of 0.25%.

$$\begin{aligned} f_0 &= \frac{1}{2\pi\sqrt{LC}} \simeq \sqrt{f_e \cdot f_m} \\ &= \frac{1}{2\pi\sqrt{LC\sqrt{1-K^2}}} \end{aligned} \tag{6.3}$$

6.2.1 CALCULATION OF RESONANT FREQUENCIES

Equation (6.2) is a well-known expression for the coupling coefficient between identical cavities and has been used extensively in iris design [76, 17, 16]. The procedure for finding the natural resonant frequencies is also standard, but no information on mode identification in a multi-mode environment, i.e. what mode does a specific $f_{e/m}$ pertain to, is readily available. The GSM of the complete coupled cavity structure of figure 6.1 is built up by cascading the aperture junctions, the aperture waveguide length and the cavity lengths as in figure 6.2.

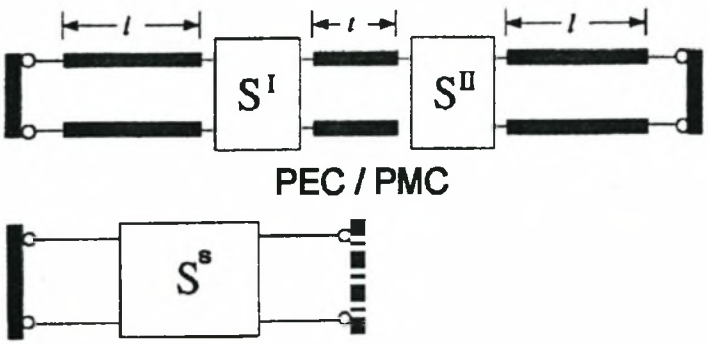

Figure 6.2: Mode-matching model of symmetrical coupled cavity structure

For each propagating mode in the cavities, two natural resonant frequencies can again be found separately by inserting either a PEC or a PMC at the symmetry plane in the centre of the iris. Applying the boundary conditions results in the following equations:

$$\begin{bmatrix} -\mathbf{a}_1 \\ \mp\mathbf{a}_2 \end{bmatrix} = \begin{bmatrix} \mathbf{s}_{11}^s & \mathbf{s}_{12}^s \\ \mathbf{s}_{21}^s & \mathbf{s}_{22}^s \end{bmatrix} \begin{bmatrix} \mathbf{a}_1 \\ \mathbf{a}_2 \end{bmatrix}$$
$$0 = \begin{bmatrix} \left[\mathbf{s}_{11}^s\right] + [\mathbf{I}] & \left[\mathbf{s}_{12}^s\right] \\ \left[\mathbf{s}_{21}^s\right] & \left[\mathbf{s}_{ss}^s\right] \pm [\mathbf{I}] \end{bmatrix} \begin{bmatrix} \mathbf{a}_1 \\ \mathbf{a}_2 \end{bmatrix} \tag{6.4}$$

where $+[\mathbf{I}]$ corresponds to the PEC and $-[\mathbf{I}]$ to the PMC. The system of equations in (6.4) has a nontrivial solution only if $\begin{bmatrix} \left[\mathbf{s}_{11}^s\right] + [\mathbf{I}] & \left[\mathbf{s}_{12}^s\right] \\ \left[\mathbf{s}_{21}^s\right] & \left[\mathbf{s}_{ss}^s\right] \pm [\mathbf{I}] \end{bmatrix}$ is singular, so that the natural resonant frequencies f_e and f_m can be found from equation (6.5):

$$\Re(f) = \det \begin{bmatrix} \left[\mathbf{s}_{11}^s\right] + [\mathbf{I}] & \left[\mathbf{s}_{12}^s\right] \\ \left[\mathbf{s}_{21}^s\right] & \left[\mathbf{s}_{ss}^s\right] \pm [\mathbf{I}] \end{bmatrix} = 0 \tag{6.5}$$

This is the standard method for the calculation of coupling coefficients from the natural resonant frequencies of the structure. Very little information is available in literature on how resonant frequencies are linked to propagating modes. Accatino [76] uses symmetry properties of the iris structures to isolate coupling and natural resonant frequencies of specific propagating modes. This requires different mode sets for each propagating mode, which is impractical for general CAD procedures.

In the new CAD procedure, the natural resonant frequencies are determined by analysing the complete structure of figure 6.3. This is not usually done, because the complexity of the analysis is increased, but using the complete structure allows for the calculation of both natural resonant frequencies of a propagating mode in one analysis. Equation (6.5) then becomes:

$$\Re(f) = \det\left[\mathbf{S}^c + \mathbf{I}\right] = 0 \tag{6.6}$$

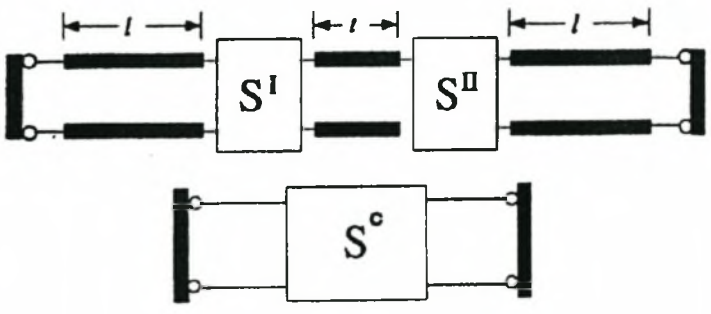

Figure 6.3: Mode-matching model of complete coupled cavity structure

After adding the cylindrical cavity lengths, all non-propagating modes can be discarded and only the s-parameters of the propagating modes are retained. In order to identify and link each root of equation (6.6) to a particular resonant mode, the source of the singularity must be found. Examination of the form of $\left[\mathbf{S}^c + \mathbf{I}\right]$ shows that at resonance of a specific mode i (of n resonant modes), the i^{th} and the $(n+i)^{th}$ rows and columns are the same, causing the singularity. This procedure can be used to link all natural resonant frequencies found to specific propagating modes in the cavities. As an example of this analysis method, a triple-mode iris will be investigated.

6.2.2 EXAMPLE OF A TRIPLE-MODE IRIS ANALYSIS USING COMPLETE COUPLED CAVITY STRUCTURE

A typical iris for use in a triple-mode environment is shown in figure 6.4. Three resonant modes exist in the cavities on either sides of the aperture with the physical dimensions as follows:

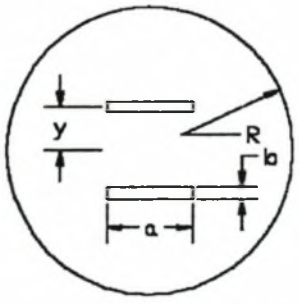

- Resonant Modes: TE_{113} – sin /cos, TM_{012}
- Resonant frequency 10GHz
- Cavity radius: 13.24mm
- Cavity lengths: 60mm

Figure 6.4: Typical triple-mode iris

The GSM of the complete coupled cavity structure is determined by the mode-matching method and equation (6.6) is used to determine the six natural resonant frequencies; two for every propagating mode. Since $\Re(f)$ is a complex valued function of frequency, the roots of both the real and the imaginary parts of $\Re(f)$ must be calculated. A typical response over the frequency band of interest is given in figure 6.5(a). In the frequency range 9.9GHz to 10GHz both the real and imaginary parts $\Re(f)$ have six zeros. Figures 6.5(b) and (c) show more detail of the imaginary axis where the proximity of some of these roots is clearly visible. The hatched area of figure 6.5(c) includes three more roots to be distinguished with the scale on the y-axis already 10^{-9}. For this example, thousands of EM-evaluations are required to determine the roots accurately and uniquely.

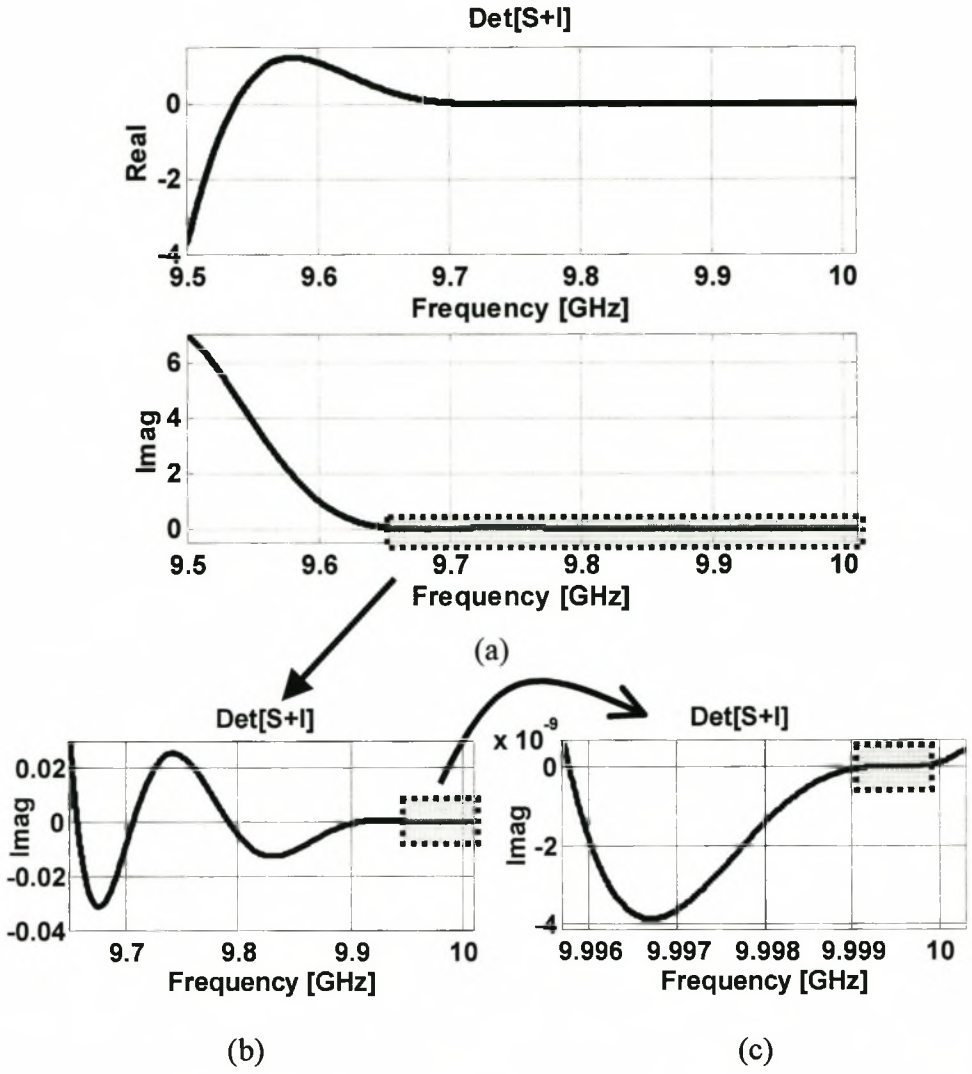

Figure 6.5 (a): Typical Det[**S**+**I**] of triple-mode iris in frequency band of interest.

(b) and (c): Im(Det[**S**+**I**]) of the same iris showing cluster of roots.

Once all six the natural resonant frequencies have been determined, the specific mode that is at resonance must be identified using the procedure introduced above. This requires a single EM-evaluation of the coupled cavity structure at each of the natural frequencies. Table 6.1 summarises the calculated coupling coefficients and resonant frequencies.

Table 6.1: Summary of coupling coefficients and resonant frequencies of triple-mode iris example				
Propagating Mode	Natural Resonant Frequency [GHz]		Coupling Coefficient	Centre Frequency [GHz]
	f_m	f_e	K	f_0
$TE_{113-cos}$	9.70600	9.99936	0.02978	9.8516
$TE_{113-sin}$	9.99578	9.99965	0.000387	9.9977
TM_{012}	9.79150	9.99947	0.02100	9.8949

The biggest problem clearly lies in determining the four roots situated close to 10GHz. Some of the existing options for solving the problem are:

- Use the symmetry properties to calculate f_e and f_m separately. This would simplify the calculation of f_m but would not really affect the complexity of calculating f_e.
- Some authors use reduced mode sets based on symmetry properties to isolate different coupling modes [76]. While this is a valid option, it is not suited to use in general CAD procedures.

To solve this problem, two procedures are proposed here:

- A rational interpolation model of the characteristic function can be constructed. By using an adaptive sampling algorithm, such a model can be constructed from a minimum number of points. This number depends on the complexity of the characteristic equation as will be shown in the following sections. Once constructed, the model offers a fast evaluation of the function at any point. In addition, the specific use of a rational function as interpolant, results in a ration of polynomials, one containing zeros and the other poles. The use of only the numerator, reduces the root-finding to the trivial problem of determining the roots of the numerator polynomial.
- The propagating modes can be isolated by reducing the number of entries in the GSM. This reduces the complexity of the characteristic equation (6.6) and thereby the number of EM-evaluations significantly.

6.2.3 EXAMPLE OF A TRIPLE-MODE IRIS DESIGN WITH ADAPTIVE SAMPLING ALGORITHM

The adaptive sampling algorithm introduced in chapter 5.3 minimises the number of EM-evaluations required to approximate equation (6.6) within a pre-determined error over a given frequency range. Figure 6.6 shows how this technique was used to approximate det[S+I] for the same triple-mode example as in the previous section. Only twenty-three support points (indicated by the crosses) were needed to reduce the estimated error over the desired frequency range to below –250dB. This very low error was required to resolve the roots uniquely.

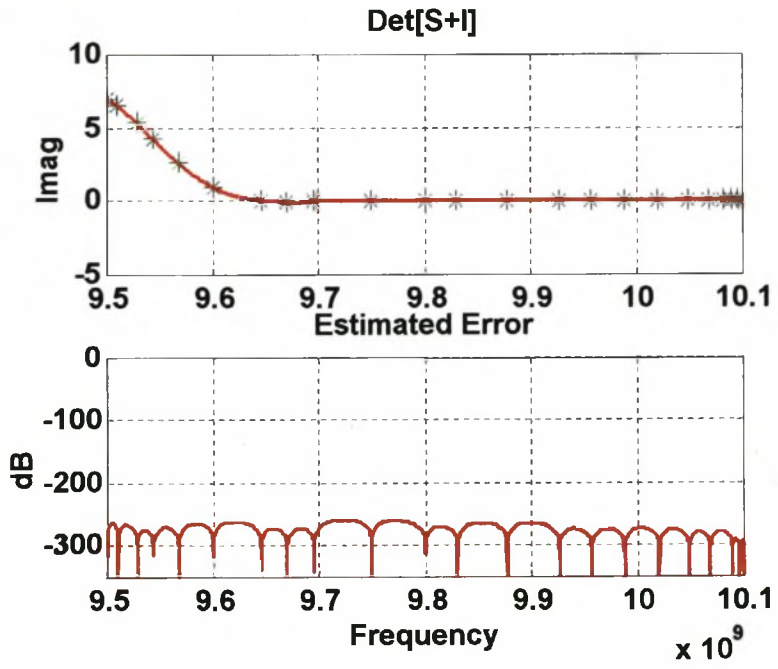

Figure 6.6: Det[S+I] using ASA with 23 support points

Rational interpolation is used to interpolate between the support points, which means that the interpolant is in the form of the ratio of two polynomials.

$$\Re(f) = \frac{\sum_{k=0}^{\xi} p_k f^k}{\sum_{k=0}^{\upsilon} q_k f^k} = \frac{N_\xi(f)}{D_\upsilon(f)} \tag{6.7}$$

In determining the natural resonant frequencies only the roots of the numerator polynomial, which can be found very efficiently with any available root-finding algorithm, must be determined. The total number of EM-evaluations required to

calculate the three coupling coefficients in this case is twenty-nine: twenty-three for the evaluation of $\Re(f)$ and six for mode identification.

6.2.4 EXAMPLE OF A TRIPLE-MODE IRIS DESIGN WITH REDUCTION OF GSM ENTRIES

When no cross-coupling between modes exists, i.e. $s_{21}^{c}(i,j) \approx 0,\ i \neq j$, two modes can be isolated by adding short circuits to their ports and terminating the remaining modes in their respective wave impedances as is shown in figure 6.7. The reduced scattering matrix for determining the coupling coefficient between modes 'a' becomes:

$$\mathbf{GSM}^{c}_{\text{reduced}} = \begin{bmatrix} s_{11}(a,a) & s_{12}(a,a) \\ s_{21}(a,a) & s_{22}(a,a) \end{bmatrix} \tag{6.8}$$

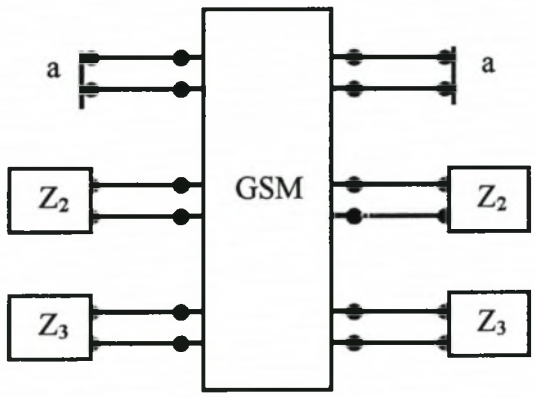

Figure 6.7. Isolation and termination of modes for reduced GSM

Isolating the TE_{11}-cos mode in the triple-mode example in this way and using the ASA to approximate $\Re(f)$, resulted in figure 6.8 where only eight support points were used.

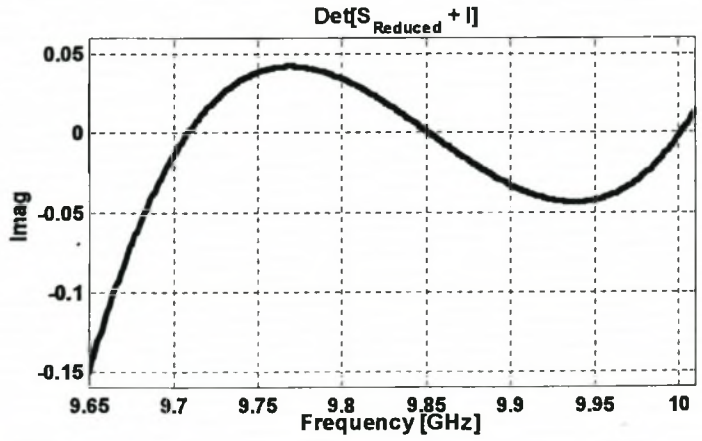

Figure 6.8: Det [$S_{reduced}$ + I] of triple-mode iris in frequency band of interest.

The reduction in complexity can be seen clearly with an estimated error of −120dB resulting in a sufficiently accurate approximation. Two roots of $\Re(f)$ can be found for each isolated propagating mode in the band of interest and f_e and f_m calculated with the reduced GSM are exactly the same as that calculated with the complete GSM. The imaginary part of $\Re(f)$ also includes a third root that corresponds to the centre frequency of the coupled cavity structure. From another equivalent circuit in figure 9, the imaginary part of the input impedance can be used to give further insight into this result.

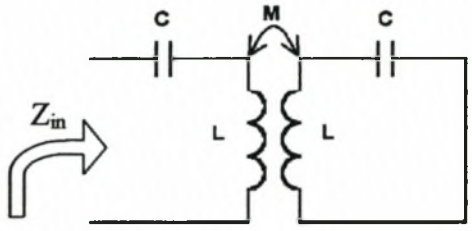

(a)

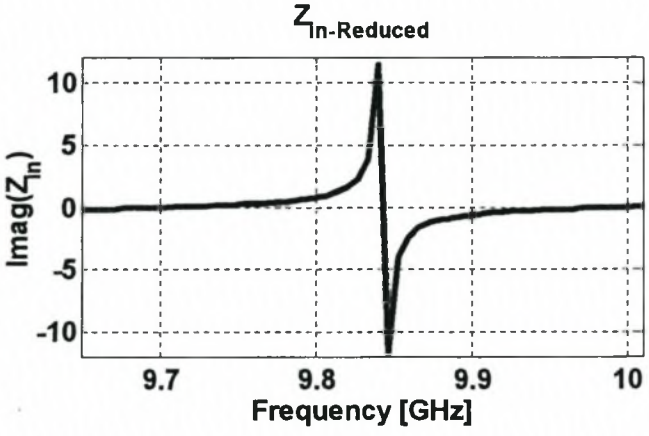

(b)

Figure 6.9: Input impedance of equivalent circuit showing resonant frequencies

From network theory the natural resonant frequencies of the coupled resonator circuit occurs at the zeros of Im(Z_{in}) and the centre frequency, which is the actual frequency of coupling f_0 from equation (3), occurs where $\mathrm{Im}(Z_{in}) = \pm\infty$. The zeros correspond exactly to f_e and f_m, and the position of $\pm\infty$ corresponds to within less than 0.5% to the centre root of figure 8. It is therefore possible to determine the coupling coefficient and the frequency of coupling from only the imaginary part of $\mathrm{Det}[\mathbf{S}_{Reduced} + \mathbf{I}]$ for every propagating mode. The total number of EM-evaluations required to determine all the coupling coefficients for this triple-mode example was

twenty-four (three times eight) for the ASA interpolation. Since the modes are isolated in the reduced GSM no further analyses are required to identify the resonant modes.

6.2.5 OPTIMISATION WITH AGGRESSIVE SPACE MAPPING

Once an efficient analysis technique has been developed, an optimisation routine is required for a complete CAD procedure. The Aggressive Space Mapping (ASM) procedure introduced in chapter 5.4 has proven to be a very efficient optimisation routine where the number of EM-evaluations are minimised by performing iterative optimisation on a simpler model of the physical structure. EM-evaluations are only performed to find and validate a map between the EM-model and the simple model.

While small aperture theory has been used extensively in the design of multiple-coupled cavity filters, there are some limitations that cause inaccuracies in a multi-mode environment. Some comparative studies performed by Yao [17] (using mode-matching) and Couffignal [62], show that for small coupling coefficients such as are typically used in narrow bandwidth filters, errors of not more than 10% can be expected.

Because small aperture theory is relatively accurate, describes the same physical parameters as the EM-analysis and is very fast to compute, it can be used as a very good coarse model in an ASM procedure. For the application of iris design the optimisation space $\mathbf{X}_{os}$ is a gradient-based optimisation routine where the small aperture theory coupling coefficient and frequency of coupling are optimised by minimising the least square error. The frequency of coupling is best determined by using equation (6.3), where f_e is approximately equal to the resonant frequency of the unperturbed cavity, and f_m can be determined from equation (6.2). The EM-space $\mathbf{X}_{em}$ is the coupling coefficient technique using mode-matching, adaptive frequency sampling and GSM reduction as described above. Two case studies are presented where the number of EM-evaluations required to achieve the same optimisation error for the ASM technique and direct gradient-based optimisation where the least square error is minimised, is compared.

For direct optimisation using the mode-matching technique, small discontinuities may occur in the optimisation function, leading to an unnecessary number of function evaluations in the final stages of the optimisation routine. This is as a result of a

change in the number of modes used as the size of the apertures change. This problem can be overcome by using a two-stage optimisation technique. The first stage allows the number of modes to vary until a relatively small error remains. At this point the optimal number of modes required for the evaluation can be determined and the optimisation completed with this fixed number of modes.

6.2.5.1 Case I: Optimising triple-mode iris for TE_{113}-cos coupling of 0.01 at 10GHz

For this case only two input parameters, the length of the aperture and the cavity length, are used. For the direct optimisation procedure small aperture theory is used to obtain a good starting position and the two-stage optimisation technique described above, requires twenty-five coupling coefficient calculations to produce an error of less than 0.1%. The same design using the ASM procedure required only four coupling coefficient calculation for the same optimisation error. In both instances an average of seven point five EM-evaluations were used in each coupling coefficient calculation. Figure 6.10 summarises the results for this test case.

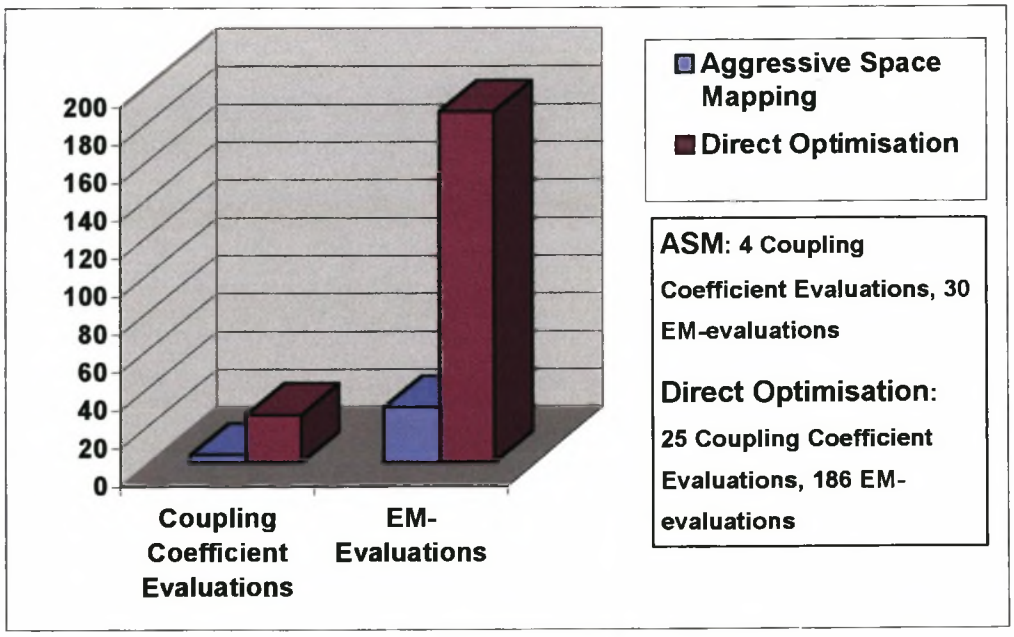

Figure 6.10: Comparison between number of EM-evaluations required by ASM and Direct Optimisation: 2 input variables, 2 optimisation targets

6.2.5.2 Case II: Optimising triple-mode iris for TE_{113}-cos coupling of 0.01 and TM_{012} coupling of 0.007 both at 10GHz

In order to achieve both coupling coefficients simultaneously the y-offset of the aperture must also be allowed to change. The correct frequency of coupling will only be obtained by allowing both the cavity radius and length to be varied. This problem therefore has four input variables. The comparative results are shown in figure 6.11 where the direct optimisation routine required one hundred and twenty-two coupling coefficient calculations compared to the twelve used by the ASM procedure. This is a remarkable result when one compares the number of EM-evaluations: ninety for the ASM procedure and nine hundred and sixty for direct optimisation.

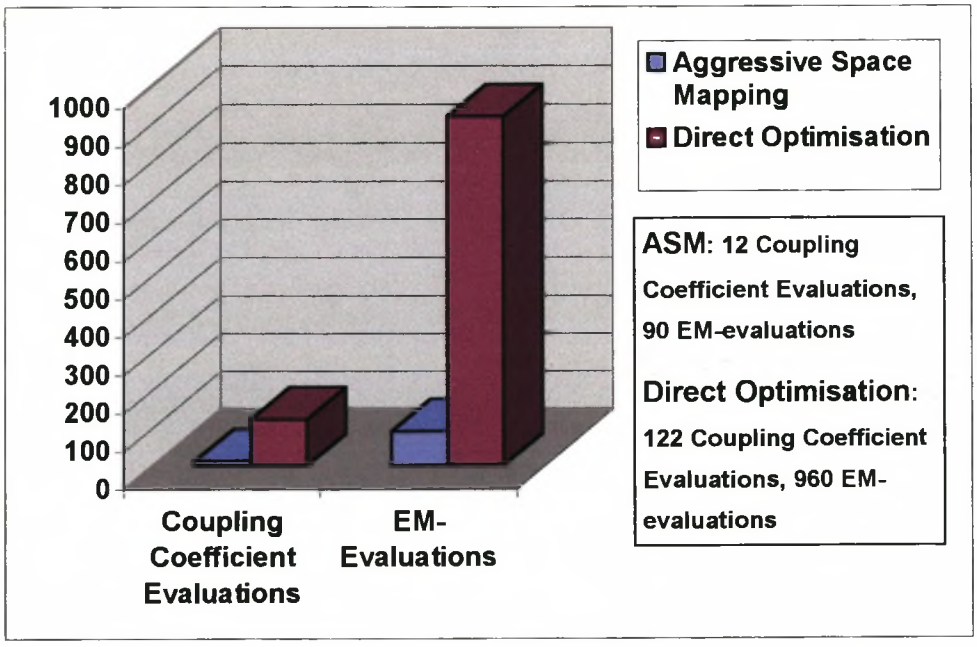

Figure 6.11: Comparison between number of EM-evaluations required by ASM and Direct Optimisation: 4 input variables, 4 optimisation targets

From these two test cases it is clear that even when using an adaptive sampling algorithm and the reduced GSM technique, numerical design of complex irises can be very time-consuming. However, the incorporation of the aggressive space mapping technique, results in a very efficient CAD design procedure that uses the minimum number of EM-evaluations required for a specific design.

6.3 CAD PROCEDURE 2: DESIGN OF IRISES WITH CROSS-COUPLING

6.3.1 PROBLEMS WITH EXISTING TECHNIQUES

The CAD procedure presented in the previous section is limited to the design of irises where no cross-coupling between propagating modes exists. This means that the above technique is limited to a small number of applications. In the case of centred irises, the first cross-coupling will occur between the TE_{11} and TM_{11} modes. For symmetrical pairs of off-centred irises (such as in figure 6.4) the first unavoidable cross-coupling will be found between TM_{01} and TE_{21} modes. These are the third and fourth propagating modes. In the case of a single off-centred iris, which is the classical problem in cylindrical waveguide, cross-coupling will occur when both the TE_{11} and the TM_{01} modes are propagating. Since these two modes are the two lowest order modes it is a problem that is often encountered. A typical off-centred iris with the individual mode tangential magnetic field distributions, is shown in figure 6.12.

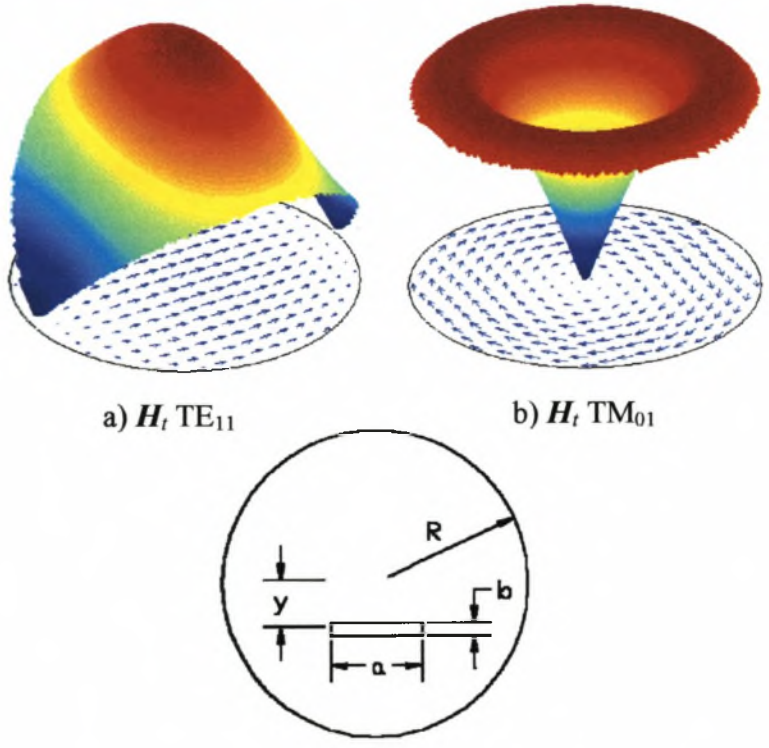

Figure 6.12: Tangential magnetic fields of the TE_{11} and TM_{01} modes incident on a typical iris with rectangular iris offset in the y-direction

When the iris is placed in the centre there is magnetic field coupling between the TE-modes on both sides of the iris and electric field coupling between the TM-modes. If the iris is displaced in the y-direction, there will be added magnetic field coupling between the TM-modes and magnetic field coupling between the TE-and TM-modes

through the aperture. This type of iris was first introduced by Rosenberg [45, 7] to realise novel filter topologies but no analysis of the coupling coefficients of the structure is given. An analysis of the TE-TE coupling of such an iris was attempted by Yao [17] where the mode-matching technique was used to calculate the natural resonant frequencies of the structure. The results of this analysis were compared to the results obtained from small aperture theory and are given in figure 6.13.

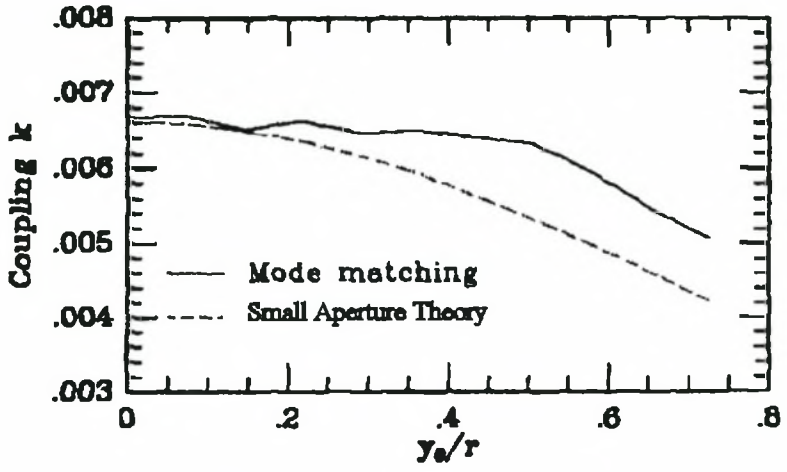

Figure 6.13: Comparison of off-centred iris TE-TE coupling coefficients and small aperture theory [17]

The mode-matching analysis clearly shows unexpected behaviour. The reason for this is that the analysis was performed on a cylindrical cavity with radius $R = 0.3638\lambda_{111}$ where λ_{111} is defined as the guide wavelength of the TE_{111} mode. At 10GHz this corresponds to a radius of 14mm and the cut-off frequency of the TM_{01} mode in such a waveguide is 8.196GHz. The cavity would therefore also support the propagation of the TM_{01} mode and cross-coupling between the TE and TM modes would occur. The technique employed, cannot be used for irises where cross-coupling occurs because the equivalent circuit of the structure has changed and the method is no longer applicable. Figure 6.14 shows all the roots of $\Re(f) = \det\left[\mathbf{S}^c + \mathbf{I}\right]$ required by equation (6.2) to determine the coupling coefficients of a similar structure with the TE_{113} and TM_{012} modes resonant at 10GHz. The roots around 9.8GHz should be the f_m natural resonant frequencies, with f_e approximately 10GHz. This graph shows the same type of uneven curve for the TE-TE coupling as was reported by Yao [17]. Also lacking from the

figure is the expected increase of the TM-TM coupling coefficient, and no extra information regarding TE-TM coupling is available.

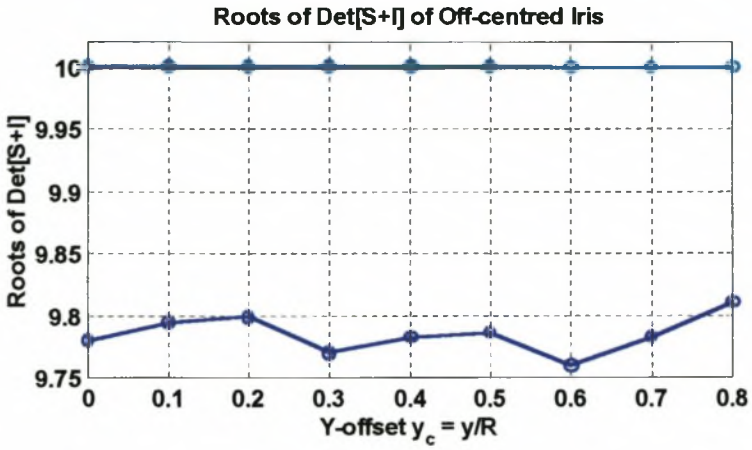

Figure 6.14: Roots of $\Re(f) = \det\left[\mathbf{S}^c + \mathbf{I}\right]$ for offset iris structure

An equivalent circuit of the complete problem given in figure 6.15 shows that for off-centred irises four resonant circuits and all possible couplings between them exist. These extra couplings are not accounted for in the preceding analysis. When a perfect electric conductor is inserted in the symmetry plane of the iris to calculate the f_e resonant frequencies, for example, the magnetic field perturbation caused by the iris will result in coupling between the TE and TM modes in the same cavity. This property is used in chapter 8 to design novel coupling structures for multi-mode filters without coupling screws. The roots of $\Re(f) = \det\left[\mathbf{S}^c + \mathbf{I}\right]$ can now no longer be used to determine the inter-cavity coupling coefficients.

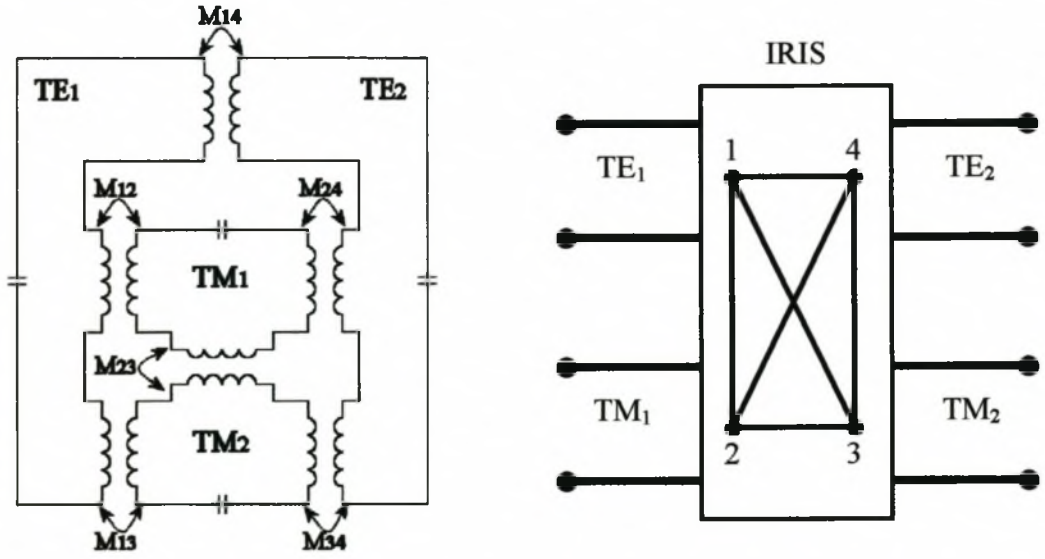

Figure 6.15: Equivalent circuit of off-centred iris structure

In the equivalent circuit $M_{12} = M_{34}$ and $M_{13} = M_{24}$ leaving four independent coupling coefficients.

The off-centred iris problem was also investigated by Guillot [18] where the cross-coupling between the TE_{113} and TM_{012} modes is used to design an in-line elliptic filter. The method used for determining the coupling coefficients is the weak input-coupling method described in the measurement technique chapter 4.4.1. The results from their analysis are given by figure 6.16a for the TE-TE coupling and figure 6.16b for the TE-TM coupling. The coupling coefficients are determined from the coupling bandwidths as:

$$K = \frac{\text{Coupling Bandwidth}}{f_0} \tag{6.9}$$

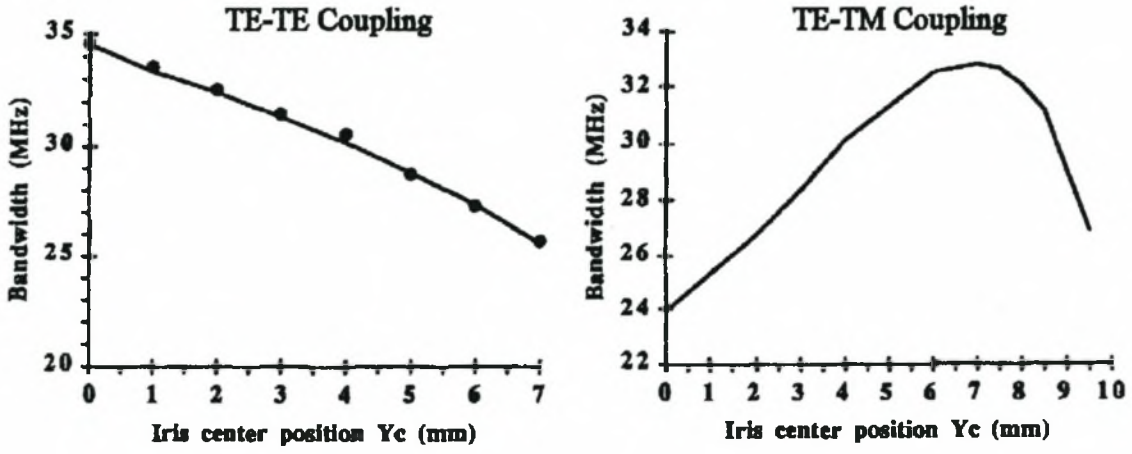

(a) (b)

Figure 6.16: a) TE-TE coupling bandwidth from [18]

b) TE-TM coupling bandwidth from [18]

While this method can be used to determine the TE-TE couplings accurately, it is not clear how the TE-TM coupling was determined. The first problem is that Guillot uses centred irises for the weak input and output coupling. Since there can be no input coupling to the TM-mode from such an iris, the TE-TM coupling bandwidths must have been determined in some other way. It is also not explained how the peaks in the transmission response (see chapter 4.4) were identified in a structure where four independent coupling bandwidths exist. A possible effect of this problem can be seen in figure 16b where a relatively large TE-TM coupling bandwidth is shown for a centred iris. Since the TM_{01} mode has no tangential H-component in the direction of

the length of the iris and TE-modes have no perpendicular E-field, the coupling between the two modes for a centred iris must be zero, and the results in figure 16b cannot be valid at $Y_c = 0$.

6.3.2 NEW CAD PROCEDURE FOR OFF-CENTRED IRISES

For the analysis of the complete fourth order system of an offset iris problem, the simultaneous use of two methods introduced earlier in this work, is proposed. The first method covered in the measurement techniques chapter 4.2 identifies the coupling coefficients and resonant frequencies of multiple-coupled cavity resonator filters by optimising the equivalent network coupling matrix to fit a transmission and reflection response. This method is portrayed as being the only method available to determine coefficients of cross-coupling of both synchronously and asynchronously tuned resonators. Some of the shortcomings of the method, such as the non-uniqueness problem and the occurrence of local minima are overcome by comparing the results to those found from using the equivalent reactances and impedance inverter description as presented in the classical filter design chapter 3.3.4. This method can be used to determine the direct couplings for TE-TE and TM-TM modes, as well as the change in resonant frequency as a result of the coupling. Ensuring that these values are correctly determined by the optimisation routine can assist in the correct calculation of the cross-coupling terms.

To verify this technique, the coupled cavity structure of figure 6.17 was designed. The cavities support the TE_{113} and TM_{012} modes at 10GHz. This results in a cavity radius of 13.24mm. An iris of 0.1mm thickness giving a TE-TE coupling coefficient of 0.03 at 10GHz at the $y = 0$ position was used.

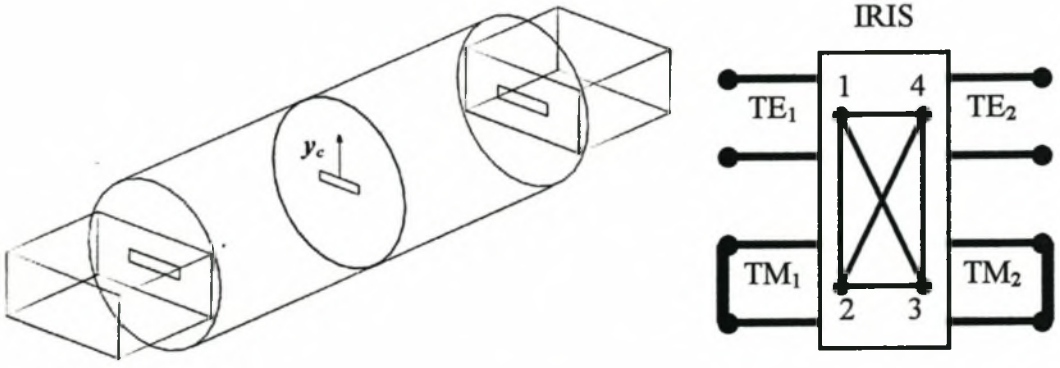

Figure 6.17: Coupled cavity structure for analysis of off-centred iris coupling

Centred input and output irises were used for excitation of the TE_{113} modes in the cavity. The mode-matching technique and adaptive sampling algorithm were used to find the transmission and reflection response of the complete structure with a minimum number of EM-evaluations. The analysis procedure was repeated for iris offset positions $y = y_c \cdot R$, with y_c ranging from 0 to 0.8. After each analysis the 4x4 coupling matrix was optimised with a gradient-based optimisation technique to produce the same response, thereby extracting the coupling coefficients and resonator frequencies. A typical optimised response is shown in figure 6.18 for $y_c = 0.3$.

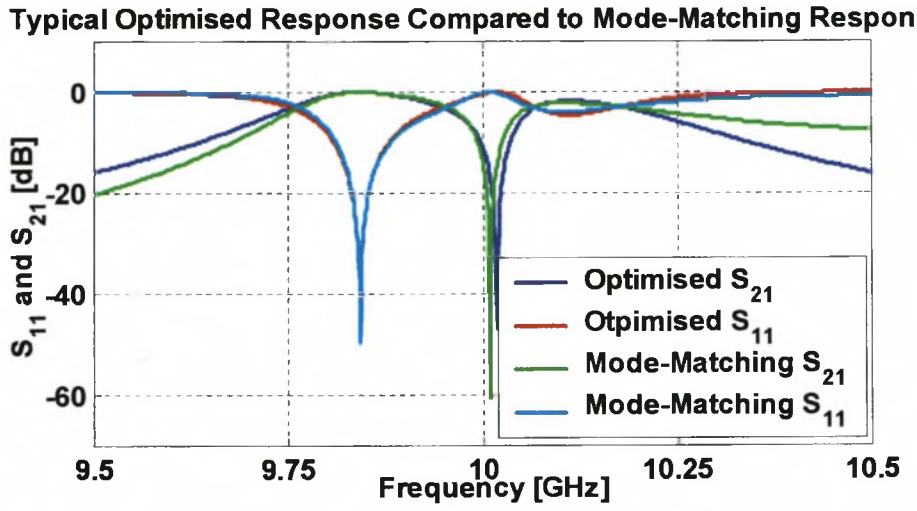

Figure 6.18: Typical optimised response compared to mode-matching response

It is clear from the figure that it is very difficult to obtain a perfect match of the equivalent circuit and mode-matching responses through optimisation. The same problems of local minima and non-uniqueness found when applying this procedure to measured data (chapter 4.3) are encountered here. The coupling coefficient results of the first optimisation iteration are given in figure 6.19.

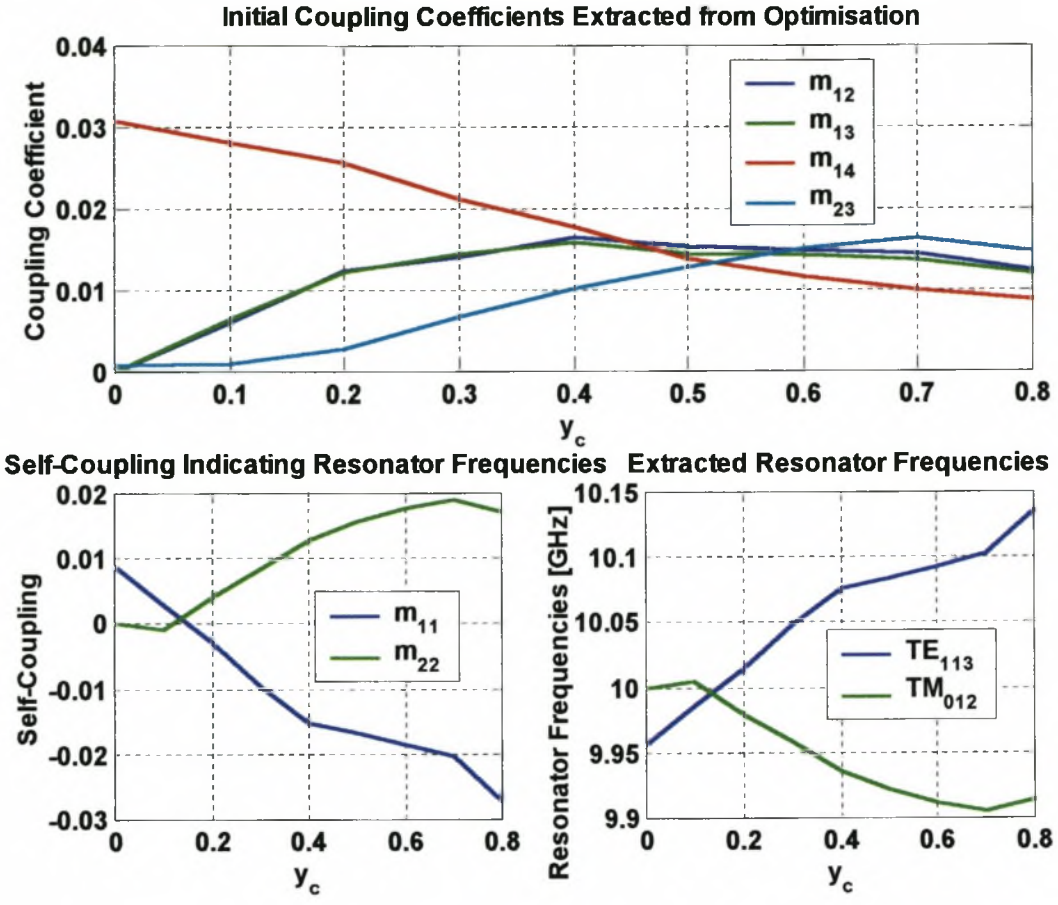

Figure 6.19: Initial coupling coefficients and resonator frequencies extracted by optimisation (refer to figure 6.17 for m_{ij} designations)

Some preliminary observations can be made:

- Although these results cannot be taken as completely accurate as a result of the non-uniqueness of the optimisation process, the shapes of direct coupling coefficient curves for TE-TE (m_{14}) and TM-TM (m_{23}) couplings are as expected. The TE-TE curve follows the tangential magnetic field distribution curve of the TE_{11} mode at the iris junction as given in figure 6.12. The TM-TM curve starts at a small non-zero value as a result of electric field coupling and then follows the corresponding TM_{01} tangential magnetic field distribution of figure 6.12.

- Couplings m_{12} and m_{13}, which are the TE-TM couplings in the same cavity and through the iris to the coupled cavity, are almost equal. This is also to be expected: when an equivalent source description of the infinitely thin iris case is examined, the source of the TM-mode transmitted through the iris and the source

of the reflected TM-mode must be equal. Since the iris used is very thin the constraint that $m_{12} \approx m_{13}$ can be used to simplify the optimisation procedure.

- The self-coupling values follow the curves of the direct TE-TE and TM-TM coupling coefficients. The resonant frequencies can be determined from these values as shown in the chapter dealing with measurement techniques.

$$f_{res} = \frac{-m_{ii} + \sqrt{m_{ii}^2 + 4}}{2} \cdot f_0 \tag{6.10}$$

where f_0 is the centre frequency at which the equivalent circuit is evaluated. The TE_{113} resonant frequency starts slightly below 10GHz and increases as the effect of the iris on the resonant frequency diminishes. The TM_{012} resonance starts at 10GHz and first increases as a result of smaller electric field coupling before the effects of magnetic coupling become dominant.

The direct TE-TE and TM-TM coupling coefficients can also be calculated from the equivalent *T*-circuits of the iris, with shunt and series reactances X_p and X_s respectively, as shown in chapter 3.3.4. The normalised reactances can be determined from the scattering parameters of the iris [47].

$$\begin{aligned} jX_s &= Z_0 \frac{1 - S_{12} + S_{11}}{1 - S_{11} + S_{12}} \\ jX_p &= Z_0 \frac{2S_{12}}{(1 - S_{11})^2 - S_{12}^2} \end{aligned} \tag{6.11}$$

The TE-TE and TM-TM coupling coefficients were determined according to this method by analysing the iris structure with the mode-matching technique at the frequencies determined with the initial optimisation procedure. Since the s-parameters do not vary appreciably with frequency, these approximate frequencies can be used. Figure 6.20 shows the comparison between these results and those determined with the optimisation procedure.

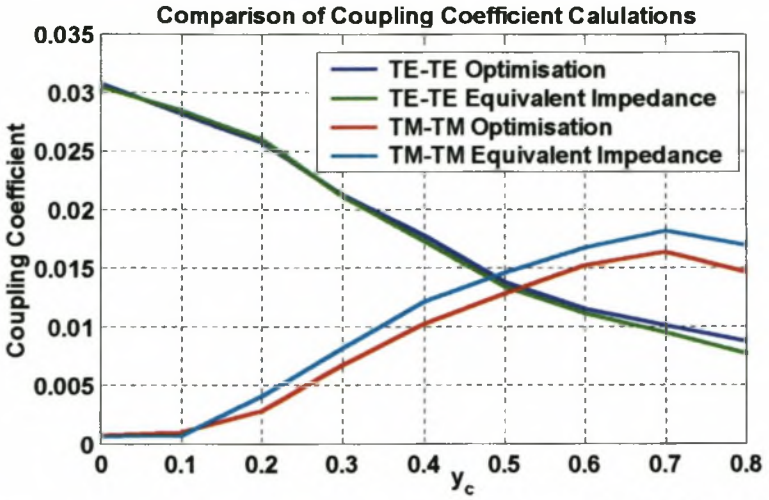

Figure 6.20: Comparison of coupling coefficients: determined using optimisation and equivalent impedances

Although the results are in good agreement, some discrepancies are observed and can be ascribed to the non-uniqueness of the optimisation procedure and the occurrence of local minima. These problems can be overcome by fixing the TE-TE and TM-TM coupling coefficients in the optimisation routine to those determined by the equivalent impedance method. With the further constraint that $m_{12} \approx m_{13}$ the correct values for the TE-TM coupling coefficient terms can be extracted. The final results for all the coupling coefficients and resonator frequencies are shown in figure 6.21.

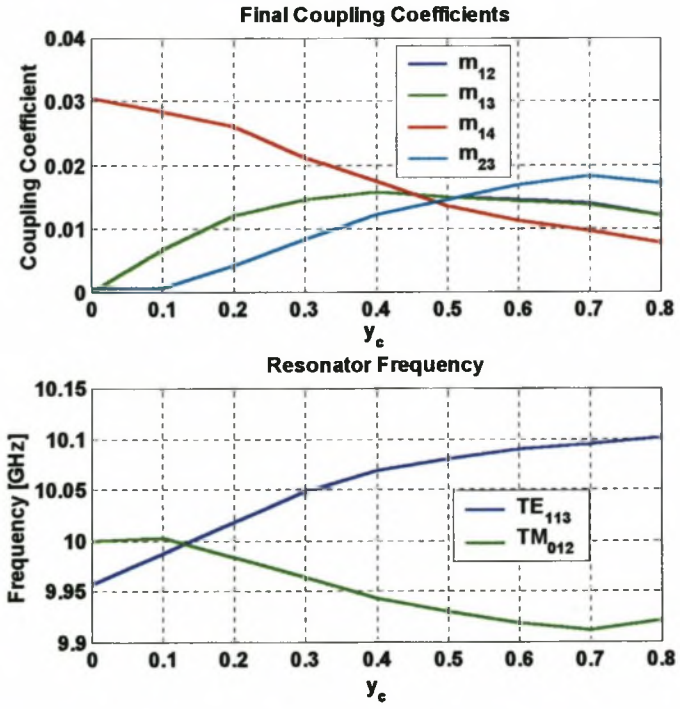

Figure 6.21: Final coupling coefficients and resonator frequencies of off-centred iris

The TE-TM coupling coefficients are almost identical and follow the product of the TE-TE and TM-TM coupling coefficient curves and not that of the TM-TM curve as was suggested by Guillot [18] in figure 6.16(b).

With the ability to determine all the coupling coefficients and resonator frequencies of structures that allow cross-coupling between propagating modes, a complete CAD procedure can be obtained by including an optimisation routine. Since the small aperture theory technique described in chapter 3 does not include the calculation of coefficients of cross-coupling, and no other suitable coarse models could be found, direct optimisation was preferred to the use of aggressive space mapping. While less accurate EM-analyses (fewer modes used in the mode-matching technique) can also be used as space mapping coarse models, direct optimisation was found to be more efficient for this application.

6.4 CAD PROCEDURE 3: COUPLING BETWEEN NON-IDENTICAL CAVITIES

The first CAD procedure presented in section two was developed specifically for coupling between identical cavities. In many cases coupling between non-identical cavities, or different modes in identical or non-identical cavities, is desired. Riblet [79] showed how the use of different cavity sizes can improve the spurious response of a coupled cavity filter. In order to reduce the physical size of the filter or facilitate tuning, triple-mode cavities supporting TE_{111}, TM_{010} and TE_{113}, TM_{012} modes can be cascaded. While the CAD procedure for off-centred iris design problems can be used for this purpose, a more general and efficient technique is developed in this section.

6.4.1 PROBLEMS WITH USING NATURAL RESONANT FREQUENCIES OF NON-IDENTICAL CAVITIES

The natural resonant frequencies of two non-identical resonators can be found by examining the equivalent circuit of figure 6.22.

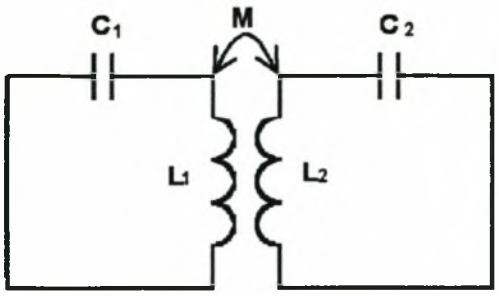

Figure 6.22: Equivalent circuit of non-identical coupled cavities

For this equivalent circuit, two resonant frequencies can again be found:

$$f_h^2 = \left(\frac{1}{2\pi}\right)^2 \frac{L_1C_1 + L_2C_2 + \sqrt{\left(L_2C_2 - L_1C_1\right)^2 + 4M^2C_1C_2}}{2C_1C_2\left(L_1L_2 - M^2\right)} \tag{6.12a}$$

$$f_l^2 = \left(\frac{1}{2\pi}\right)^2 \frac{L_1C_1 + L_2C_2 - \sqrt{\left(L_2C_2 - L_1C_1\right)^2 + 4M^2C_1C_2}}{2C_1C_2\left(L_1L_2 - M^2\right)} \tag{6.13b}$$

Substitution of this result into equation (6.2) leaves:

$$K = \frac{f_h^2 - f_l^2}{f_h^2 + f_l^2} \tag{6.14}$$

$$= \frac{\sqrt{\left(L_1C_1 - L_2C_2\right)^2 + 4M^2C_1C_2}}{L_1C_1 + L_2C_2}$$

This as such, is not a very useful result, but by setting $L_1C_1 = L_2C_2$ the general equation for the coupling coefficient is obtained:

$$K = \frac{M}{\sqrt{L_1L_2}} \tag{6.15}$$

This means that the two natural resonant frequencies of any coupled cavity structure can be used to determine the coupling coefficient, on condition that the resonant frequencies of the two separate resonators are equal:

$$\omega_0 = \frac{1}{\sqrt{L_1C_1}} = \frac{1}{\sqrt{L_2C_2}} \tag{6.20}$$

In practical coupled cavity design, though, this is very difficult to enforce, since the unperturbed resonant frequency of a cavity is approximately the same as f_e and not the desired coupling frequency f_0.

6.4.2 CAD PROCEDURE USING THE PHASE OF THE REFLECTION COEFFICIENT

A more general method of determining the coupling coefficients between dissimilar coupled cavities was introduced as a measurement technique in chapter 4.2.3. The complete structure that can be analysed using this method, is shown in figure 6.23.

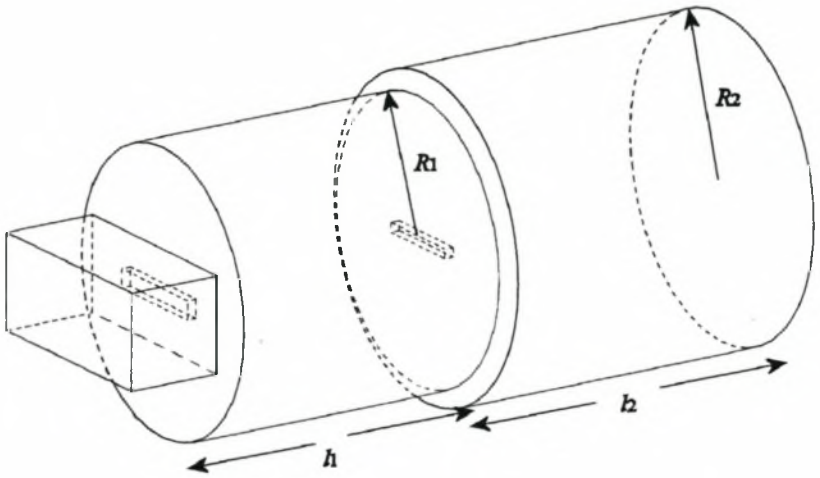

Figure 6.23: Non-identical coupled cavity structure to be analysed by determining the phase of the input reflection coefficient

The ±180° and 0° phase crossings correspond to the zeros and the poles of the input impedance and using the equations of Yao and Atia [56], the two resonator frequencies and the coupling coefficient can be determined. For only two resonators, the equations given previously can be simplified. The resonant frequencies are determined from:

$$f_1 = \frac{f_{z1} f_{z2}}{f_p}$$
$$f_2 = f_{z1} \tag{6.21}$$

The coupling bandwidth is given by $m_{12} = 2\pi\sqrt{f_{z1} + f_{z2} - f_p - f_1}$ so that the coupling coefficient becomes:

$$K_{12} = \left(\frac{f_{z1} + f_{z2} - f_p - f_1}{f_1 f_2} \right)^{\frac{1}{2}} \tag{6.22}$$

The frequency at which the phase response goes through 90° is used to determine the input resistance:

$$R = \frac{\left(f_{90°}^2 - f_{z1}^2\right)\left(f_{90°}^2 - f_{z2}^2\right)}{f_1 f_{90°}\left(f_{90°}^2 - f_p^2\right)} \tag{6.23}$$

A typical phase response of two non-identical resonators is given in figure 6.24. The length of rectangular waveguide that must be present to allow the evanescent modes excited by the input iris to die away, adds unwanted phase to the analysis. The reference plane is shifted in the same way as proposed in the measurement chapter so that the peaks of the group delay of the reflection coefficient coincide with the ±180° positions of the phase.

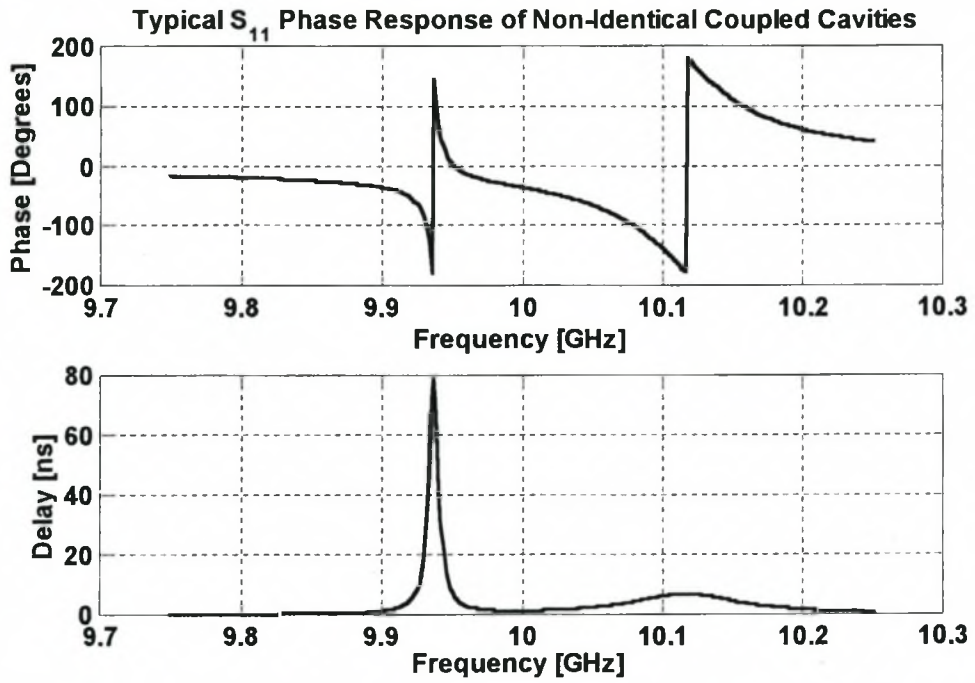

Figure 6.24: Typical phase of reflection coefficient and delay response of two non-identical coupled cavities

The resonant frequencies, coupling coefficient and input resistance calculated from this response are:

$$f_1 = 10.102\text{GHz}, \quad f_2 = 9.95\text{GHz}$$
$$K = 0.01, \qquad R = 0.0102\Omega$$

From the first resonance in figure 6.24, it is clear that a high frequency resolution will be required for the analysis of structures with small input terminations and small inter-cavity coupling. This problem and the finite Q-values of physical cavities are two of the shortcomings of this method as a measurement technique. The use of loss-less waveguide in the mode-matching technique and adaptive frequency sampling

solve both these problems. For a typical analysis the ASA will require ten to fourteen support points to approximate the model with an estimated error of less than –150dB. Once the ASA creates the model, it can be used to evaluate the structure at a very large number of frequency points.

This method can also be used for iris design where cross-coupling between propagating modes exists, but the mode resonant frequencies are not the same. In an off-centred iris structure, as presented in the previous section, where resonator frequencies are almost identical, phase properties of specific resonators cannot be identified by this method.

Optimisation of coupling irises using this method can again be accomplished by direct optimisation or aggressive space mapping, depending on the type of problem. Even though the equations presented in the classical iris design chapter do not hold for non-identical cavities, small aperture theory can still be used as a coarse model in a space mapping routine. The coarse model does not have to be accurate and any approximation can be used as long as a map linking the coarse model to EM-analysis can be found. Care must be taken to ensure that the coarse model is not too inaccurate as this will lead to bad starting positions for the parameter extraction phase and may cause failure of the method.

In both the direct optimisation and ASM techniques, the biggest cause of failure is the wrong choice of frequency span for the EM-analysis. Constraints must be placed on the input parameters to ensure that all the relevant ±180° and 0° phase crossings can be determined. In many cases it will be sufficient to increase the frequency span, but for a structure supporting higher order resonant modes increasing the frequency span may also introduce the phase response of these spurious modes. Since this is a general method for determining resonant frequencies and coupling coefficients it will not be possible to distinguish between the wanted and the unwanted parts of the response.

An important aspect of the optimisation of iris structures using this method, is that the calculated coupling coefficient will always be defined between two asynchronously tuned resonators offset from the target resonant frequencies. It would therefore be strictly correct to optimise the cavity lengths to find the correct cavity resonant frequencies at each optimisation step, so that the coupling coefficient error function is

correctly defined. This is a very tedious process and since the optimisation procedure does find a valid minimum, this technicality can be ignored.

6.5 CONCLUSION

This chapter introduced the development of three new CAD procedures for the design of different categories of iris structures. These structures include single centred and off-centred irises and symmetrically and asymmetrically placed multiple aperture irises. Such irises are used for coupling between identical and non-identical cavities and cavity modes.

In the following two chapters some of the CAD procedures developed in this chapter will be used to design multi-mode cavity filter components. Measurements of these prototypes clearly validate the feasibility of the CAD procedures.

Chapter 7

Diplexer Design

7.1 INTRODUCTION

The principle of using multi-mode cavities for the design of diplexers was first introduced in 1990 by Rosenburg, who proposed two prototypes. The first realised two second order Chebyschev filter channels in a single quadruple-mode cavity [80], and the second comprised two fourth order elliptical function filter channels in two quadruple-mode cavities [19]. Since parts of both filter channels are realised in the same physical structure, the size and weight of the diplexer are reduced. In such a scheme, the component normally used as a T-junction for connecting the separate filters, now becomes an integral part of the filter structures.

Some problems with such a configuration can be foreseen. Design of quadruple-mode filter structures is very complex since it can only be achieved using higher order modes. The use of higher order modes usually results in decreased spurious free frequency bands. Quadruple-mode structures are also not temperature stable and not suited for use in satellite applications [81]. The biggest problem in this case lies in achieving the desired channel isolation in such a complex structure.

In the fourth order diplexer presented by Rosenberg, the first channel is realised entirely by orthogonal TE_{112} modes and the second by TM_{110} modes. The measured transmission response of the second diplexer is shown in figure 7.1.

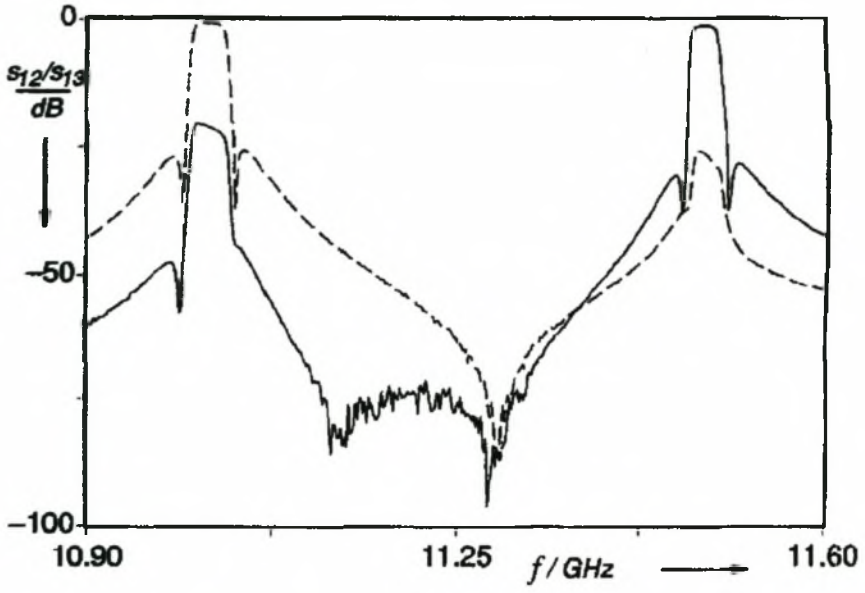

Figure 7.1: Measured transmission response selectivity of Rosenberg diplexer [19]

The measured response clearly shows that the isolation between the bands is in the order of 25dB. This is also found for the first diplexer and is unacceptable in most multiplexer applications. The author suggests that this is a result of interaction between input and output coupling apertures that are used in the same cavity. While this would certainly lead to unwanted coupling between the two filter channels, the effects of unwanted iris coupling must also be investigated, as Rosenberg does not explicitly state where the apertures in [19] are placed. The basic iris topology used, together with the modes incident on the iris, is shown in figure 7.2.

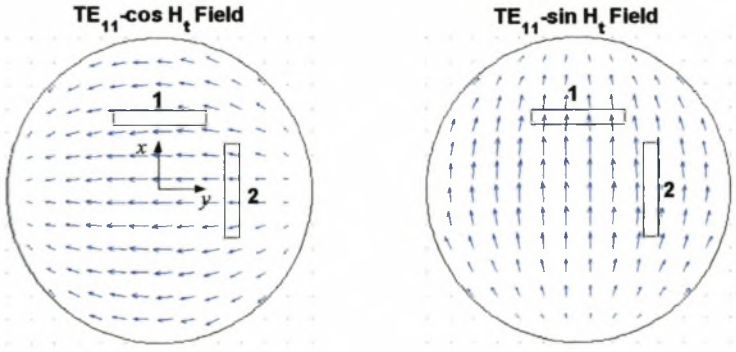

(a)

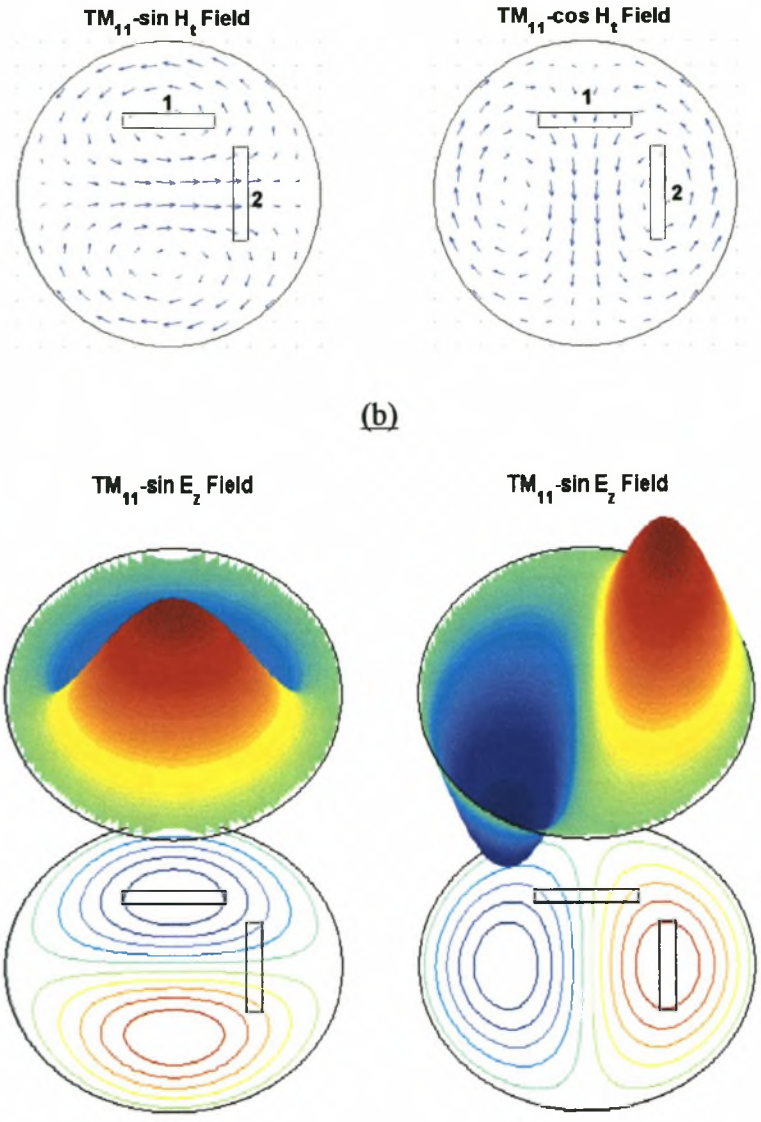

Figure 7.2: Mode fields incident on Rosenberg iris [19]

In figure 7.2 the apertures are offset by $y = x = 0.4808R$, where R is the radius of the cylinder. Each mode showed, is used as a cavity resonator on either side of the iris. From the figure it is clear that if the apertures are not placed at the zeros of the TM_{11} magnetic field there will be coupling between the TE and TM filter channels, leading to bad channel isolation. The coupling coefficients to be realised are as follows: $TE_{23} = 0.001911$, $TE_{14} = 0.000641$, $TM_{23} = 0.00142$, $TM_{14} = 0.000353$. According to Rosenberg each aperture controls one TE-TE and one TM-TM coupling. With the apertures positioned as in figure 7.2, relatively large apertures will be required for the larger TM-TM coupling, resulting in a very large TE-TE coupling. It can therefore be

assumed that in order to realise the required coupling coefficients, the apertures could not be placed so that the channel isolation is optimal.

In actual fact each aperture does not only control one TM or TE coupling. In figure 7.2a the main TE-cos coupling will be through aperture 1, while aperture 2 dominates the TE-sin coupling. For the TM-sin and TM-cos couplings in figures 7.2b and 7.2c there will be small amounts of electric and magnetic field coupling through both apertures. This is a complex iris problem that is not well suited to design with small aperture theory. One assumption that is made in small aperture theory, is that the maximum of the incident field is at the centre of the aperture. This is not the case for the TM_{11} magnetic fields as zeros are located at the centres of the apertures.

7.2 DIPLEXER DESIGN

A new diplexer structure employing quadruple-mode cavities is presented here; utilising the numerical techniques introduced in chapter 6. This diplexer realises two fourth order Chebyschev filter channels in three cavities with the basic flow diagram shown in figure 7.3. The structure is not as compact as that of Rosenberg [19], but allows more freedom in the design of irises as only one coupling is realised per iris. This allows correct positioning of apertures for optimal channel isolation. The input and output coupling elements are each placed in a separate cavity to reduce direct coupling between the filter channels. These structural changes result in significant performance improvement over the Rosenberg prototype.

In the input cavity the two filter channels are isolated by using the TE_{113} modes for the 10GHz channel and the TM_{112} modes for the 10.3GHz channel. These modes were chosen to facilitate the use of tuning and coupling elements on the sidewall of the cavity. A single iris realises coupling of the 10.3GHz channel to cavity one where the degenerate TM_{112} modes are again used. The radius of this cavity is the same as that of the input cavity. A single iris also allows coupling of the 10GHz channel to cavity three. This cavity uses degenerate TE_{113} and TM_{112} modes and the cavity radius is changed accordingly.

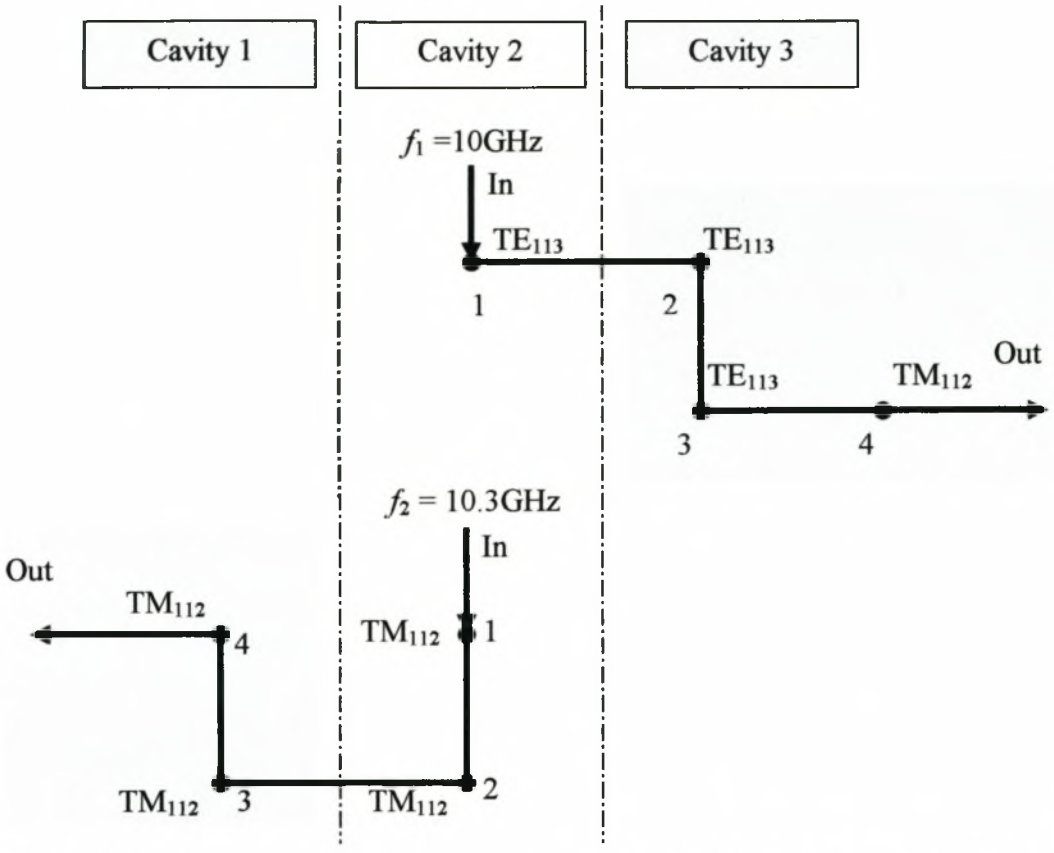

Figure 7.3: Basic coupling structure of fourth order Chebyschev channel diplexer in three cavities

The two fourth order Chebyschev filter channels are identical and designed to have a relative bandwidth of 0.8% at 10GHz and 10.3GHz respectively. For –20dB in-band reflection loss the coupling matrix required is:

$$M = \begin{bmatrix} 0 & 0.89675 & 0 & 0 \\ 0.89675 & 0 & 0.69249 & 0 \\ 0 & 0.69249 & 0 & 0.89675 \\ 0 & 0 & 0.89675 & 0 \end{bmatrix}, R_1 = R_2 = 1.043 \qquad (7.1)$$

A simulated transmission and reflection response of the diplexer is given in figure 7.4 where channel isolation of more than 70dB can be observed at the channel centre frequencies. The simulation was performed using the equivalent circuit of the input structure presented in figure 7.7 and will be discussed later in this chapter. This equivalent circuit allows for coupling between the first resonators of the two filter channels. The remaining resonators were added without allowing coupling between them.

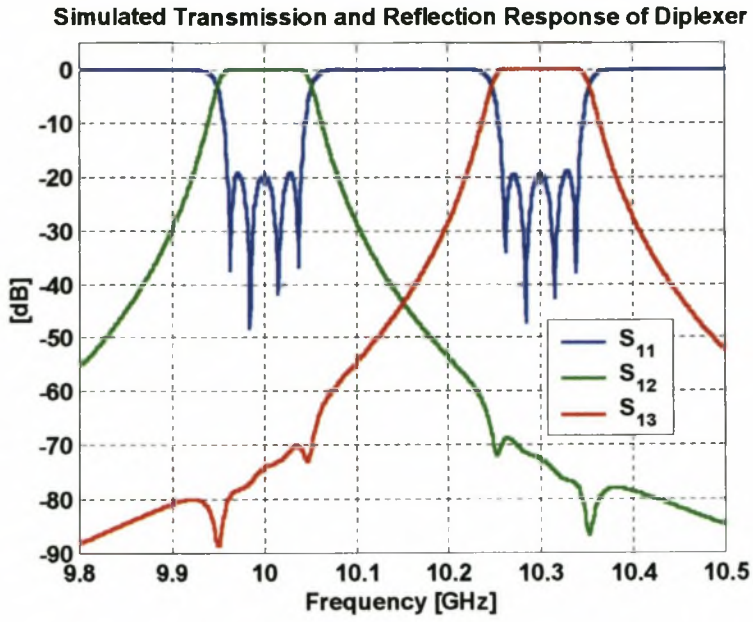

Figure 7.4: Simulated transmission and reflection response of diplexer

7.2.1 CAVITY DESIGN

The input cavity supports the orthogonal TE_{113} modes at 10GHz and the TM_{112} modes at 10.3GHz. Using a mode chart for the TE_{113} mode (figure 7.5) the diameter to length ratio of the cavity can be calculated. Cavity one (figure 7.3) uses only TM_{112} modes at 10.3GHz and therefore has the same dimensions as the input cavity. Cavity three supports both TE_{113} and TM_{112} modes at 10GHz, resulting in cavity dimensions that differ from cavities one and two.

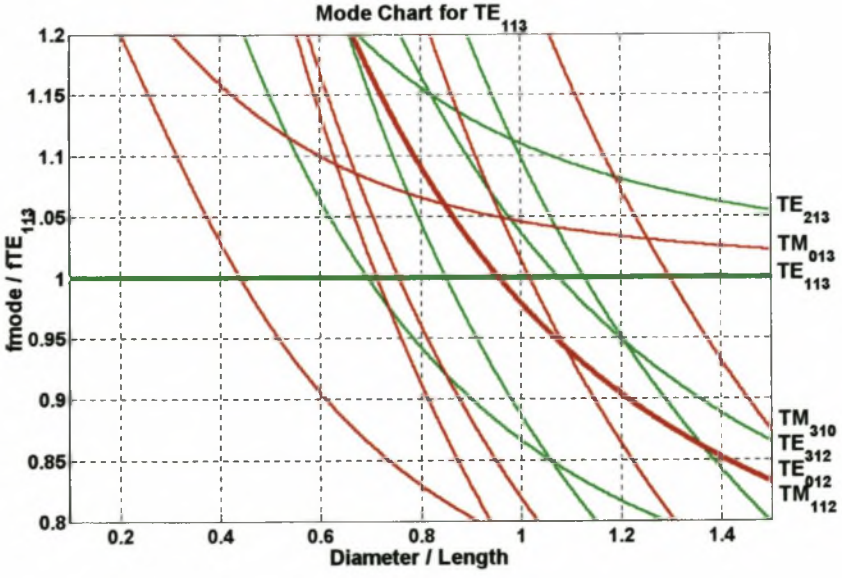

Figure 7.5: Mode chart of TE_{113} mode

From the mode chart it is clear that the TM_{11n} and TE_{01n} modes are always degenerate. Since the TE_{01} modes have only E_ϕ and H_r transverse fields there should be no coupling between this unwanted mode and the other modes. The mode chart also shows that the first spurious response can be expected form the TM_{013} mode, which will be resonant around 10.5GHz.

7.2.2 INPUT/OUTPUT COUPLING DESIGN

As described in chapter 3, input/output coupling can be achieved by using apertures in the sidewalls or end-walls of a cavity. For the input cavity an end-wall iris was preferred. Figure 7.6 shows the positioning of the iris respective to the two input modes.

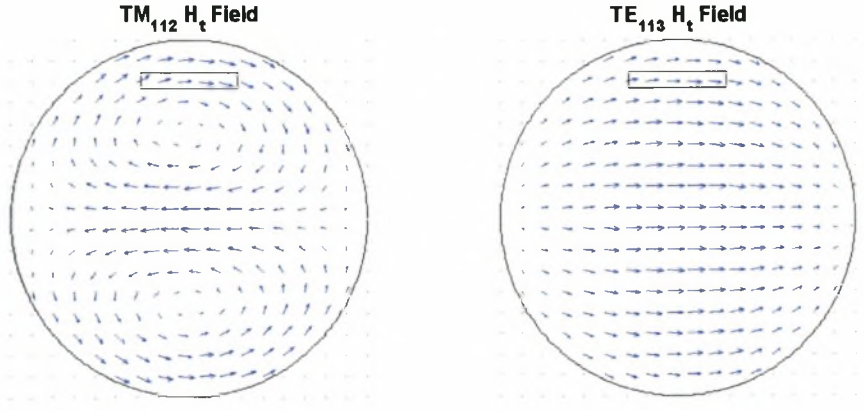

Figure 7.6: Positioning of input coupling iris

The zeros in the tangential magnetic field of the TM_{11} mode occur at $y = 0.4808R$. While the input aperture could also be placed at $y < 0.4808$, placing it close to the side leaves enough for the optimal positioning of a coupling aperture in the same iris, as will be seen shortly.

An equivalent circuit of such a structure, where the terminating resistance of both channels is equal, is shown in figure 7.7.

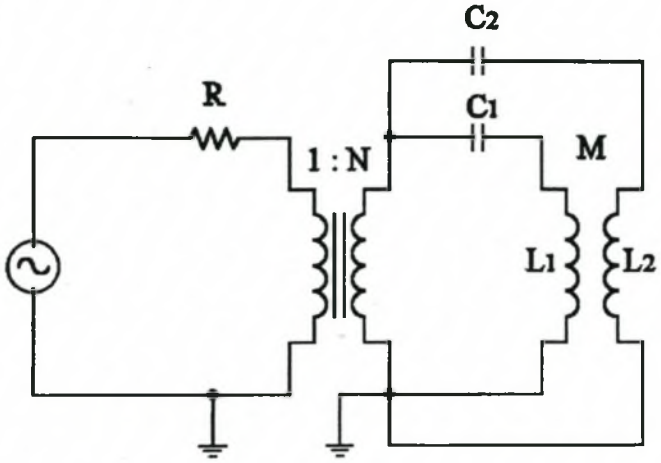

Figure 7.7: Equivalent circuit of input coupling to 2 resonant modes

The circuit shows one input coupling element exciting two resonant modes in the cavity. The resonant frequencies of the modes are given by $\omega_1 = 1/\sqrt{L_1 C_1}$ and $\omega_2 = 1/\sqrt{L_2 C_2}$. There will also be a small amount of coupling between the modes as a result of the mode field perturbation by the input iris. A typical plot of the reflection coefficient phase and group delay is given in figure 7.8.

This circuit can also be analysed with the phase of reflection coefficient technique presented in chapter 6.4, this time treating the two resonances as isolated responses. The resonant frequencies of the two resonant modes are given by the ±180° phase crossings. The external Q of the two modes can be determined by using the frequencies at which the reflection coefficient phase equals 90°, using a simplification of the equations presented by Yao and Atia [56]. For the first resonator:

$$R = \frac{f_{90°_1}^2 - f_1^2}{f_{90°_1}^2 f_1^2} \tag{7.2}$$

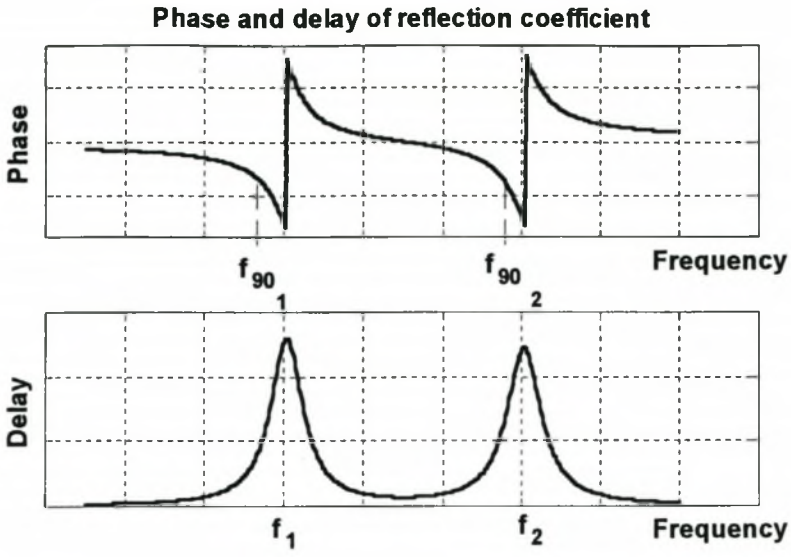

Figure 7.8: Typical phase and delay of reflection coefficient

For this structure the amount of coupling between the two modes cannot be determined using the methods described above, but can be evaluated by changing the amount of coupling in the equivalent circuit of figure 7.7 and matching the response to that in figure 7.8.

The Aggressive Space Mapping routine was used for optimisation of the input iris. The coarse model is the small aperture theory derivation of the external Q of the loaded cavity, where the input terminations of the two input modes are determined separately, and the effects on the resonant frequencies of these modes are taken into account. The fine model is the phase of reflection coefficient method using the mode matching technique as described above.

For the output coupling, apertures along the side-walls of cavities one and three were used. In both filter channels the mode used for the fourth resonator is the TM_{112} mode. This mode has two half-wavelength variations in the z-direction and no z-directed magnetic field. The TE_{113} modes have z-directed magnetic fields and three half-wavelength variations in the z-direction. For no coupling to the TE_{113} modes, the apertures must therefore be placed at the position of maximum TM_{112} H_ϕ field ($r = R$) and zeros of the TE_{113} H_ϕ field, which is in the centre of the cavity length as is shown in figure 7.9.

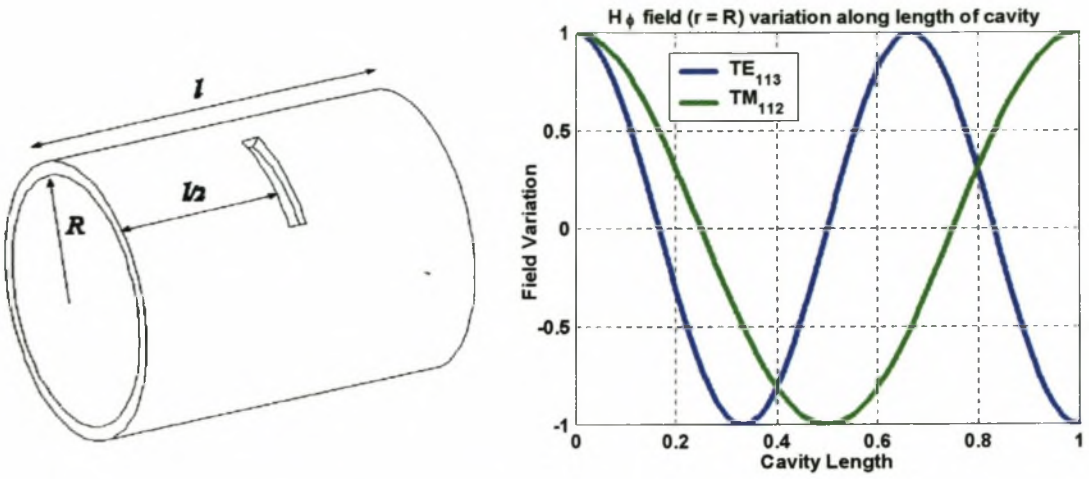

Figure 7.9: Position of output coupling apertures

While some mode-matching techniques for the analysis of such structures have been published [82, 83], small aperture theory was used here to design the output apertures, with the curvature of the cavity side-walls ignored.

7.2.3 INTER-CAVITY IRIS DESIGN

For coupling between cavities one and two, an iris coupling the two TM_{112}-cos modes on either side of the iris is required. In this case a centred rectangular aperture is used to control the coupling coefficient. Such an iris will also excite TE_{11}-sin modes in each cavity and since both cavities allow the propagation of the these modes, they will coexist in the cavities. These modes are not used as resonators in any of the diplexer filter channels and if care is taken not to allow coupling to any used resonators, they will not influence the diplexer performance. This cross-coupling does mean that the natural resonant frequencies of the structure can not be used to determine the coupling coefficients. If the coupling coefficients of the entire coupled cavity structure must be determined, the coupling matrix optimisation method introduced in chapter 6.3 must be used. In this case, though, only the TM-TM coupling coefficients are of interest and since the TM-resonators at 10.3GHz are removed from the TE-resonators at 10GHz, the phase of reflection coefficient method as described in chapter 6.4 can be used for coupling coefficient evaluation. The iris was designed with the aggressive space mapping routine, using small aperture theory as coarse model and the phase of reflection coefficient method as fine model.

The iris between the second and third cavities must allow coupling between the TE_{113}-cos modes while preventing TM_{11}-sin coupling and TE_{11}-TM_{11} coupling. This can be achieved by placing a rectangular aperture at a position of zero tangential magnetic

field of the TM_{11}-sin mode that occur at $r = 0.4808R$. Unfortunately a small amount of magnetic field coupling can be expected between the TM_{112}-cos modes used on either side of the iris, leading to reduced isolation of the two channels. Since the aperture is placed at the position of zero TM_{11}-sin magnetic field and TM_{11}-cos and TE_{11} coupling results in zero, there will be no TE_{11}-TM_{11} coupling.

Such an iris will excite TM_{01} modes that will propagate in the cavities again causing failure of the natural resonant frequency method for calculating coupling coefficients. The TM_{01n} resonances are not within the frequency band of interest and the phase of reflection coefficient method can be used. Figure 7.10 shows the position of this aperture along with the input coupling aperture on the same iris. Also shown is the rotation of the third cavity to allow simultaneous use of input and inter-cavity coupling elements.

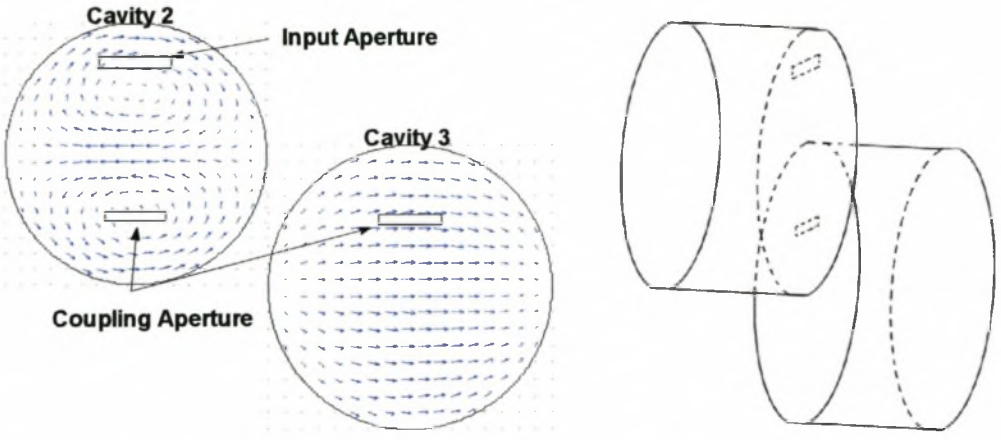

Figure 7.10: Placement of coupling aperture for iris separating cavities 2 and 3

7.2.4 COUPLING AND TUNING SCREWS

In order to control the coupling between degenerate modes and the resonant frequency of each resonator, a large number of tuning and coupling screws is required. The placement of the twelve screws (one tuning screw for each resonator and four coupling screws) is very important, especially in the input cavity where isolation of the TE and TM modes is crucial. All degenerate mode coupling and tuning will be achieved by perturbing electric fields of the modes in the cavity from the side-walls.

Figure 7.11 shows the variation of the transverse electric fields of the TE_{113} and TM_{112} modes.

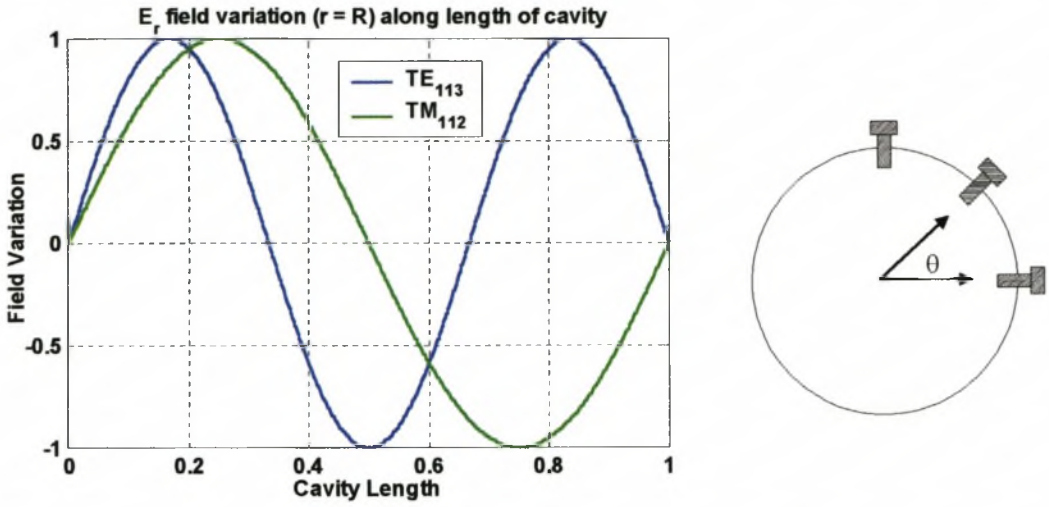

Figure 7.11: Placement of tuning and coupling screws

From this figure it is clear that placing screws at $z = 1/2l$ where the TM_{112} mode E_r field vanishes will only affect TE_{113} modes. Screws placed at $z = 1/3l$ will perturb TM_{112} mode electric fields only. Coupling between degeneracies of the same mode can be controlled by using screws at $\theta = 45°$. Cavity three requires coupling between the TM_{112} and the TE_{113} modes. This can be achieved by placing a coupling screw at $z = 0.6l$ so that the transverse electric field of both modes is perturbed.

7.3 DIPLEXER MEASUREMENT

Figures 7.12 and 7.13 show the diplexer that was constructed and measured.

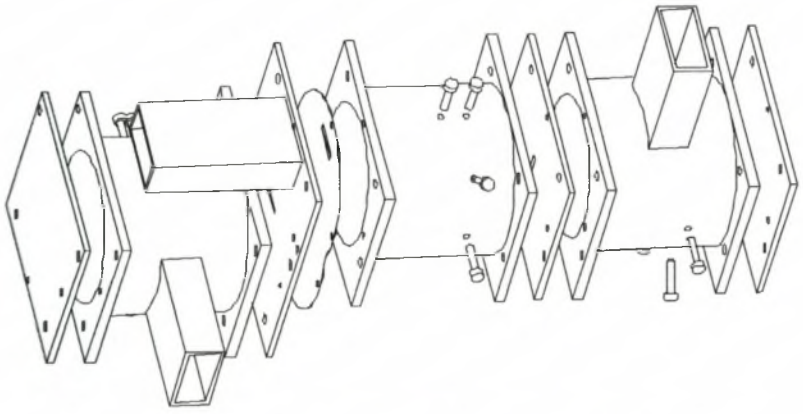

Figure 7.12: Manufactured diplexer

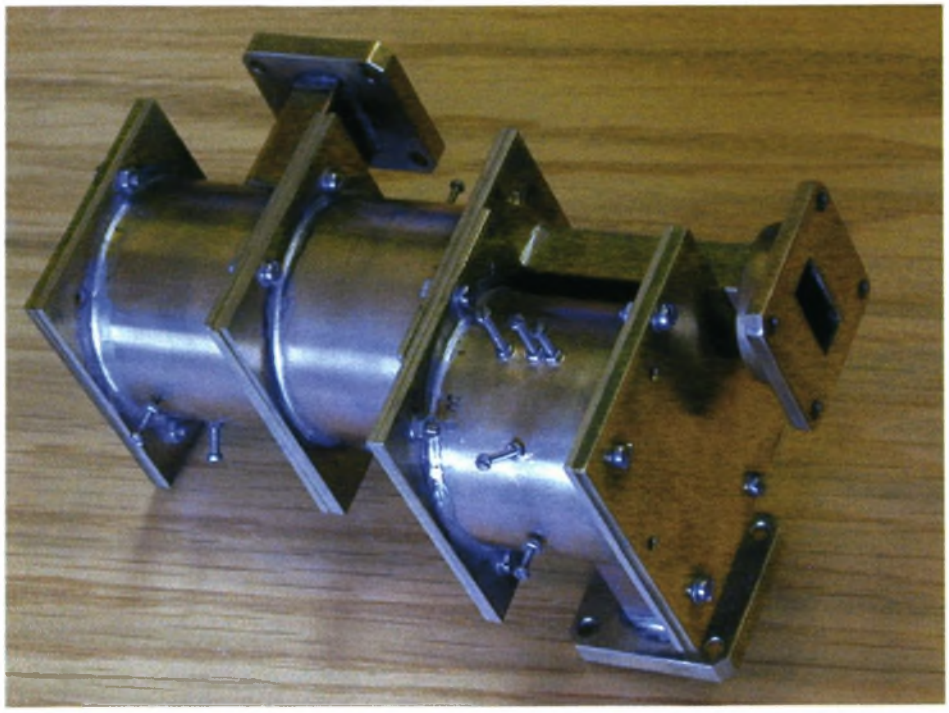

Figure 7.13: Photograph of constructed diplexer

In figure 7.12 the input port feeding the centre cavity is denoted as port one with the left and right output ports denoted as ports two and three respectively. The transmission and reflection responses of this device were measured and the results are given in figure 7.14 and summarised in table 7.1.

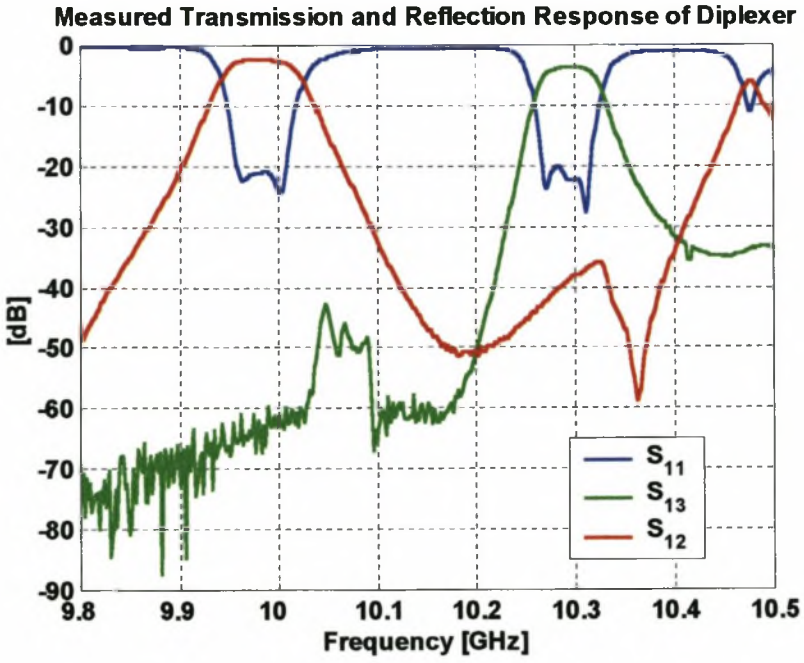

Figure 7.14: Measured transmission and reflection response of diplexer

Table 7.1: Summary of measured diplexer properties		
Diplexer Property	Designed	Measured
Centre frequency channel 1	10GHz	9.983GHz
Channel 1 bandwidth	0.8%	0.68%
Channel 1 insertion loss (BW=0.68%)	0.4dB	2.37dB
Inband isolation 10GHz	70dB	60dB
Centre frequency channel 2	10.3GHz	10.292GHz
Channel 2 bandwidth	0.8%	0.61%
Channel 2 insertion loss (BW=0.61%)	0.7dB	4.05dB
Inband isolation 10.3GHz	70dB	37dB

From figure 7.14 the two filter channels can be clearly identified. The centre frequencies are correct to within 0.15% while the channel bandwidths are slightly too small in both cases. This can be attributed to inaccuracies of the two output coupling irises that were designed with small aperture theory without adding corrections for the curvature of the cavity side-walls. This should have the effect of decreasing the length of the apertures, thereby reducing the coupling to the cavities.

The most important feature of the diplexer is the channel isolation. The isolation at 10GHz is below the measurement noise floor and therefore at least 60dB while at 10.3GHz the isolation is 37dB. This constitutes an improvement of 35dB for the one and 12dB for the other channel over the results published by Rosenberg [19]. The slightly poorer result for the isolation at 10.3GHz is as a result of the expected TM_{11}-cos coupling at the iris separating cavities two and three. These results clearly validate the correct placement and the design procedure of the coupling irises.

The expected insertion loss was derived using 50% of the theoretical unloaded Q-values of the modes in the cavities. These are 15600 and 11400 for the TE_{113} and the TM_{113} modes respectively. The discrepancy between the measured and the predicted values is as a result of manufacturing problems where the cavity flanges tended to buckle causing energy leakage from the cavities.

The first spurious resonance of the TM_{013} mode can be clearly seen at 10.47GHz as part of the S_{12} response. This is also to be expected form the mode chart (figure 7.5), because cavity three supports both TE_{113} and TM_{112} modes at 10GHz, leading to a lower resonant frequency for the TM_{013} mode. For the S_{13} trace the TM_{013} resonance is expected above 10.5GHz.

7.4 CONCLUSION

A new diplexer structure realising two fourth order Chebyschev filter channels in three quadruple-mode cavities was presented.

While this structure is larger than that presented by Rosenberg [19], more flexibility in iris placement could be achieved. This structure also allowed for the separation of input/output coupling elements into three separate cavities.

The complex problem of iris design in this multi-mode environment was overcome by using the CAD procedures developed in chapter 6. Difficulties in achieving the desired channel isolation were solved through correct placement and accurate design of inter-cavity and input irises.

Measurements of the diplexer clearly show the effectiveness of the CAD procedures in producing high-performance multi-mode coupled cavity filter components. Although the in-band insertion loss is significantly higher than that designed for, the performance of this diplexer was deemed sufficient as it validates the iris design algorithms. As these algorithms form the heart of the dissertation, their validation constitutes a successful experiment.

Chapter 8

Novel Multi-Mode Coupling Mechanism for Replacing Coupling and Tuning Screws

8.1 INTRODUCTION

The use of coupling and tuning screws has always been an integral part of the realisation of multi-mode waveguide filters. Generally, coupling between degenerate modes in a cavity is achieved by perturbation of the cavity by means of a coupling screw at positions of strong E-field distribution. While this is a simple solution to the coupling problem, a number of negative aspects can be observed:

- Filter tuning using coupling and tuning screws is usually a lengthy process and requires a lot of skill. This also makes the process expensive.
- Any intrusion into the cavity introduces loss that could have a significant impact on the insertion loss of the filter [51].
- Tuning and coupling screws reduce the power handling capability and increases the risk of passive intermodulation generation of the filter as a result of strong electric field concentration around the screws [50].
- The spurious response of the filter can be degraded as a result of unwanted coupling caused by tuning and coupling elements.

It would therefore be advantageous to be able to design multi-mode waveguide filters with fixed coupling elements and no tuning elements. A number of structures have been proposed to realise this. For rectangular dual-mode cavities the "square corner cut" type method was presented by Liang [84] and is shown in figure 8.1a. The cut in the square waveguide corner is used to control the coupling coefficient and the resonant frequencies of the degenerate modes. Initially the cut was applied along the full length of the cavity, but was later replaced by only a section at the position of a conventional tuning screw [85]. Recently the "square corner cut" method was also successfully applied to a rectangular triple-mode cavity design [86]. An alternative

concept introduced by Orta [87], figure 8.1b, uses rotated rectangular cavities to accomplish the desired coupling.

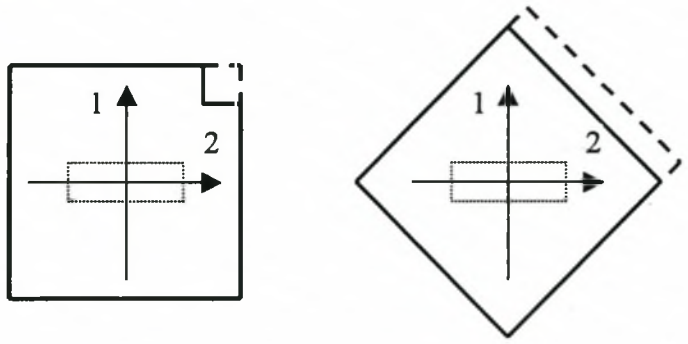

(a) (b)

Figure 8.1: Dual-mode coupling structures without coupling or tuning screws

For cylindrical dual-mode cavities a number of proposed coupling structures can be seen in figure 8.2 with the conventional coupling and tuning screws in figure 8.2a. The first attempt was to replace the screws with short rectangular posts inserted into the waveguide [88, 89]. The region including screws is solved using the Finite Elements Method (FEM), while the remainder of the structure is analysed by the mode-matching method. For very narrow bandwidths, the FEM was found not to be accurate enough [47]. A further development was the use of cylindrical ridge waveguide [figure 8.2c] where the coupling elements can be described in cylindrical coordinates.

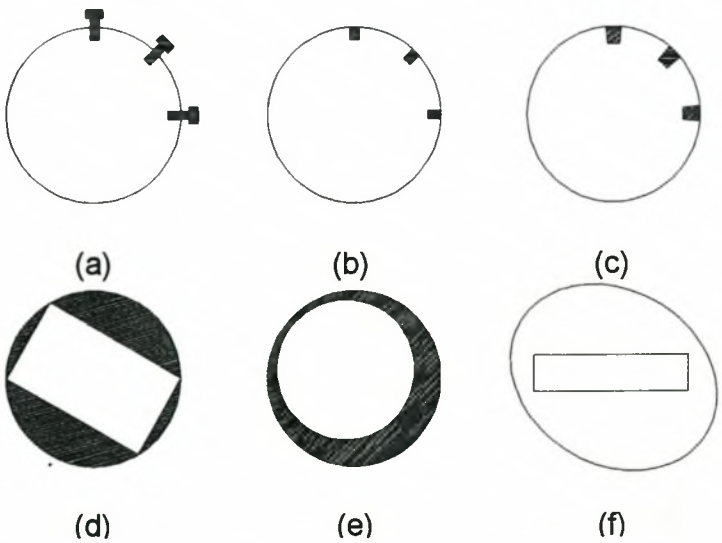

Figure 8.2: Dual-mode coupling structures in cylindrical waveguide

Two novel methods shown in figure 8.2d and 8.2e use rotated rectangular waveguide sections [90, 50] and offset circular waveguide sections [47] to control the coupling between the orthogonal degenerate modes in a dual-mode cavity. Accatino [91] has shown that the coupling characteristics of scattering from a rectangular to elliptical waveguide junction can also be used to achieve coupling in dual-mode cavities. The slight deviation from the cylindrical waveguide allows the control of both the coupling coefficient and the individual resonant frequencies of the degenerate modes. An advantage of the last three cases presented in figure 8.2, is that these structures can be analysed very efficiently with the mode-matching method and the coupling coefficients and resonant frequencies can be determined by using the methods described in the analysis chapters.

In all but the last method described above, coupling is still achieved by means of cavity perturbation at positions of strong electric field distribution along the length of the cavity. The same effect can be obtained by perturbing the magnetic fields of the degenerate modes in the cavity. A new coupling structure using magnetic field coupling is presented in this chapter. This structure allows for the design of dual-mode as well as the first triple-mode cavities without coupling screws.

8.2 NOVEL COUPLING STRUCTURE

TE_z and TM_z cavity modes have maximum tangential magnetic fields at the end walls of the cavities. If modes possess magnetic field components in the same direction, perturbation of the cavity end walls will result in magnetic field coupling between the modes. In chapter 6.4 it was shown that coupling between TE_{11} and TM_{01} modes in a single cavity occurs when a perfect electric conductor is placed in the centre of an off-centred iris. This type of structure can be used to design multi-mode cavity filters without coupling screws. Since the coupling element is placed in the end walls of the cavity and does not protrude into the cavity, degradation of the cavity Q-value is minimised.

8.2.1 TRIPLE-MODE CAVITY COUPLING ELEMENT

The basic proposed structure for coupling in triple-mode cavities supporting TE_{11} and TM_{01} modes is presented in figure 8.3. The coupling element is a length of short-circuited rectangular waveguide (stub) placed at an off-centred position at the top or

bottom wall of the cavity. With this structure, coupling between the TM_{01} and one of the orthogonal degenerate TE_{11} modes is achieved. A similar structure rotated by 90° placed at the other end of the cavity can be used to couple from the TM_{01} mode to the other TE_{11} mode.

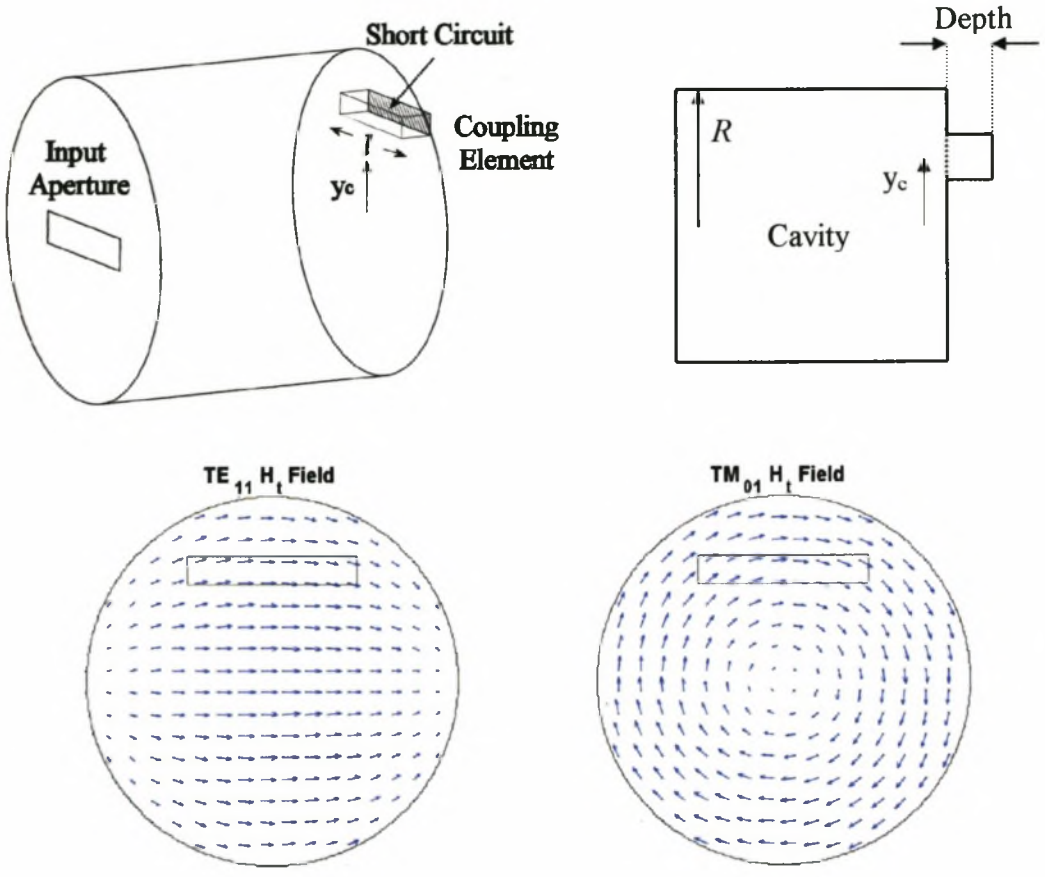

Figure 8.3: Basic coupling element for triple-mode cavities

Since the coupling structure is basically a short-circuited iris structure, the GSM can be calculated with the mode-matching technique. The TE_{11} and TM_{01} resonant frequencies will not be equal, therefore the natural resonant frequencies f_e and f_m can not be used to determine the coupling coefficients. With the addition of the input aperture in figure 8.3 the phase of reflection coefficient method can be used to find the coupling coefficient and resonant frequencies. By optimising the length and the radius of the cavity the resonators can be synchronously tuned without use of extra tuning elements.

The value of the coupling coefficient can be controlled by the offset position $y = y_c R$, the cross-sectional dimensions and the depth of the coupling stub. Figure 8.4 shows an example analysis of coupling coefficient variation with stub y-offset, length and

depth with resonator frequencies optimised to 10GHz. The variation as a result of y-offset of the stub corresponds well to the TE-TM coupling found for the offset iris problem examined in chapter 6.4.

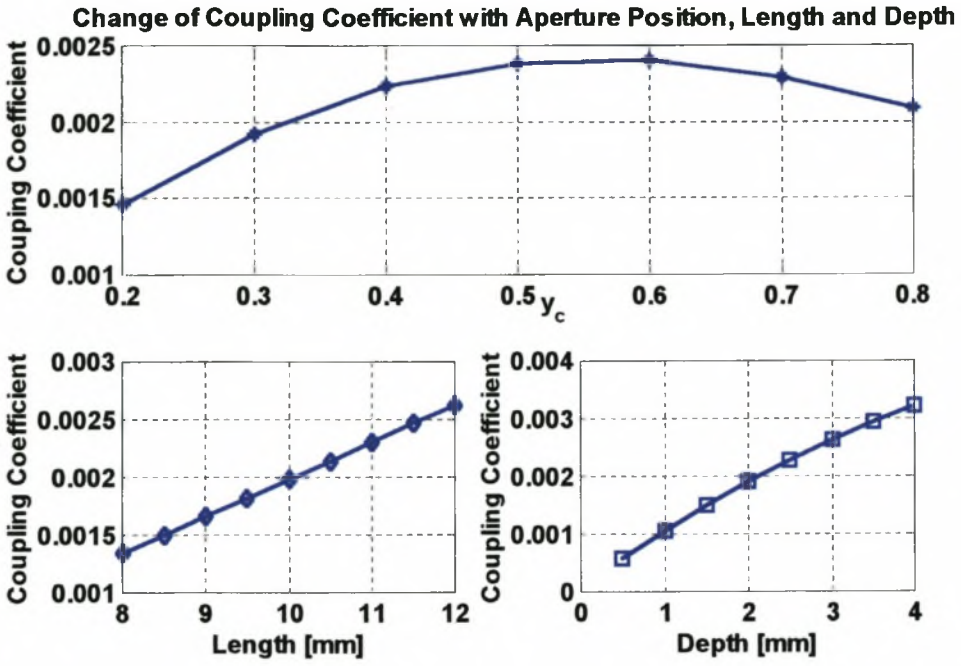

Figure 8.4: Variation of coupling coefficient with variation of coupling stub position, length and depth

8.2.2 DUAL-MODE CAVITY COUPLING ELEMENT

A similar structure shown in figure 8.5 can be used to obtain dual-mode coupling between the two orthogonal degenerate TE_{11} modes in cylindrical waveguide.

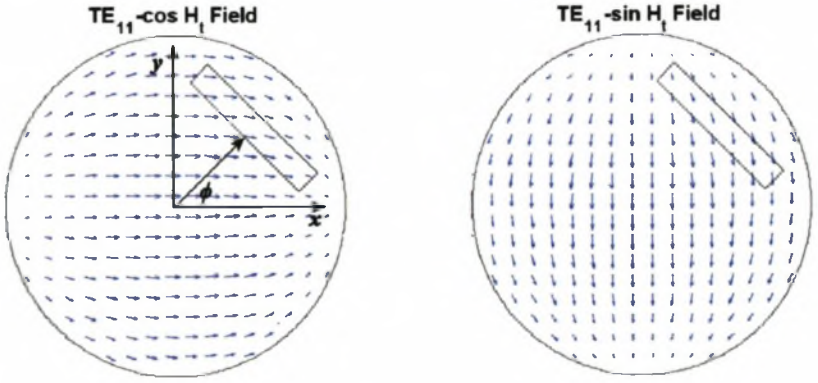

Figure 8.5: Coupling stub position for dual-mode coupling

Such a coupling structure will also allow for coupling between the TE_{11} and TM_{01} modes if both are propagating. It could therefore be used as a coupling element for

both dual- and triple-mode cavities, but can only be used for dual-mode coupling if the TM_{01} mode does not propagate. For the dual-mode case the coupling element can be placed at an angle of $\phi = 45°$ so that coupling between the modes is 1:1. This will also ensure that the resonant frequencies of the modes are equal and that the natural resonant frequencies f_e and f_m can be used to determine the coupling coefficient. The mode-matching technique can be used to determine the GSM of the cavity and coupling element. Since the coupling element is basically an off-centred iris structure rotated by ϕ degrees, the scattering parameters of the cylindrical-rectangular junction can be found by merely rotating the cylindrical mode fields through ϕ degrees when evaluating the coupling integrals in the mode-matching routine.

The value of the coupling coefficient can again be controlled by the offset position $y = y_c R$, the cross-sectional dimensions and the depth of the coupling stub. Figure 8.6 shows an analysis example where the depth of a dual-mode coupling stub was varied.

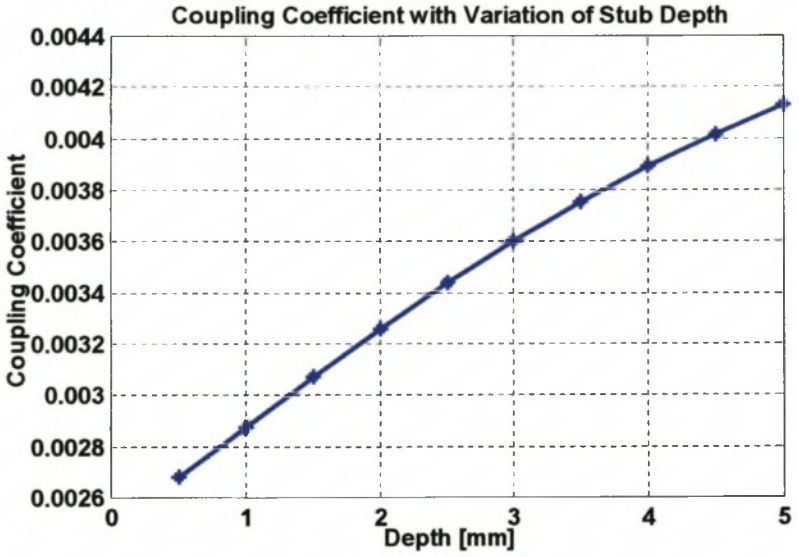

Figure 8.6: TE_{11}-cos TE_{11}-sin coupling coefficient with variation of stub depth

8.2.3 THIRD ORDER TRIPLE-MODE CAVITY FILTER EXAMPLE

In order to verify the use of this new coupling element a third order Chebyschev response filter was designed in a single triple-mode cavity without the use of coupling or tuning screws. The cavity supports both TE_{113} orthogonal modes as well as the TM_{012} mode at 10GHz. For a relative bandwidth and reflection loss of 0.5% and –23dB respectively, an input/output termination of $R_{in/out} = 0.00691$ and coupling coefficient $M_{12} = M_{23} = 0.005767$ are required.

The filter was designed in two stages. The input coupling and the first coupling coefficient were designed by using the phases of reflection coefficient method as described earlier. The triple-mode coupling element was designed by fixing the position and cross-sectional dimensions of the coupling element and optimising the depth to produce the desired coupling. The length and the radius of the cavity are optimised to fix both resonant frequencies to 10GHz. Since the filter structure is symmetrical, the final filter can be achieved by rotating the optimised structure found in stage one through 90°, cascading the two halves of the complete filter structure and optimising the filter response to fit the desired response. Figure 8.7 shows the reflection response of a Monte Carlo analysis of the final filter structure, where the optimised cavity and coupling element dimensions were perturbed by a random error not exceeding 50μm. This value corresponds to the manufacturing tolerances. The best response is shown by the thick black trace.

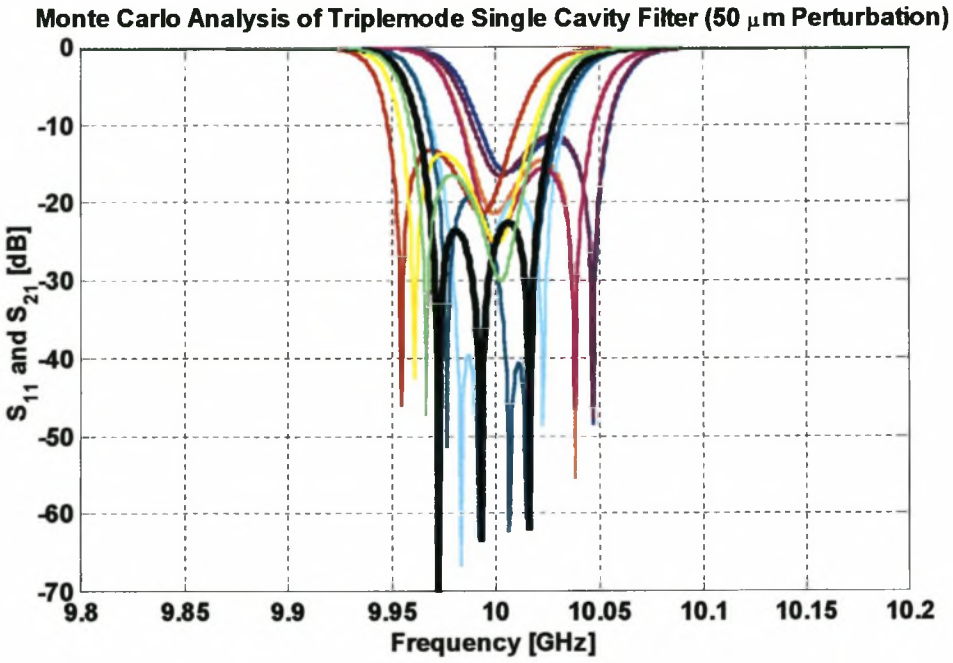

Figure 8.7: Reflection coefficient of Monte Carlo analysis of triple-mode filter

8.3 MEASUREMENT OF FILTER WITH NEW COUPLING STRUCTURE

The triple-mode filter without coupling or tuning screws was manufactured and a schematic drawing and photograph of the completed filter can be seen in figures 8.8 and 8.9.

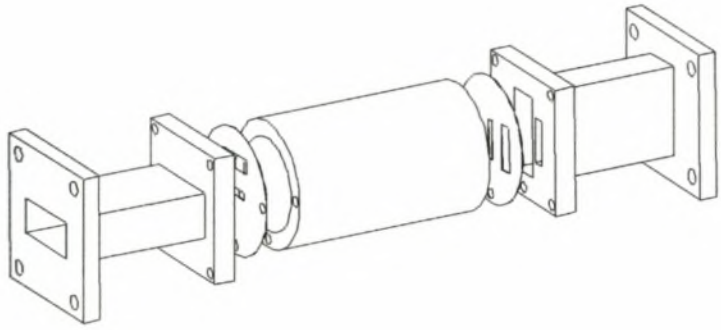

Figure 8.8: Triple-mode single cavity filter without coupling or tuning screws

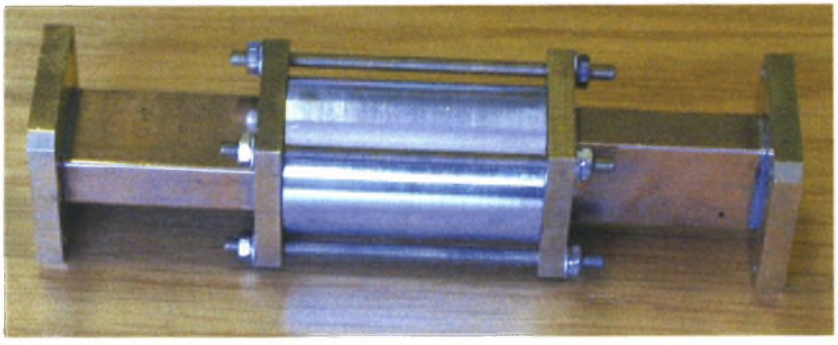

Figure 8.9: Photograph of constructed filter without screws

Initial measurements of this filter, presented in figure 8.10, shows a slight deviation from the designed centre frequency and detuning of some of the resonators. Even though the response is not perfect, it clearly validates the feasibility of both the new coupling element and the CAD procedure. It should also be noted that manufacturing tolerances of higher the 50μm were measured on the manufactured filter.

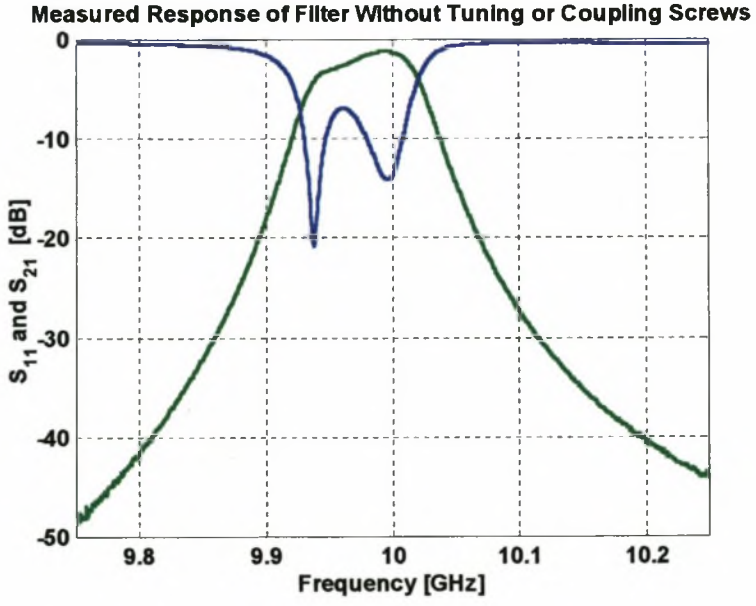

Figure 8.10: Initial measurements of triple-mode cavity without tuning screws

In order to verify the accuracy of the input iris and coupling element CAD procedure further, two tuning screws were added for independent control of the two TE_{113} resonator frequencies. The cavity length was shortened by 0.3mm, fixing the frequency of the TM_{012} mode at 10GHz, and the filter was measured using the two tuning screws to obtain the response presented in figure 8.11.

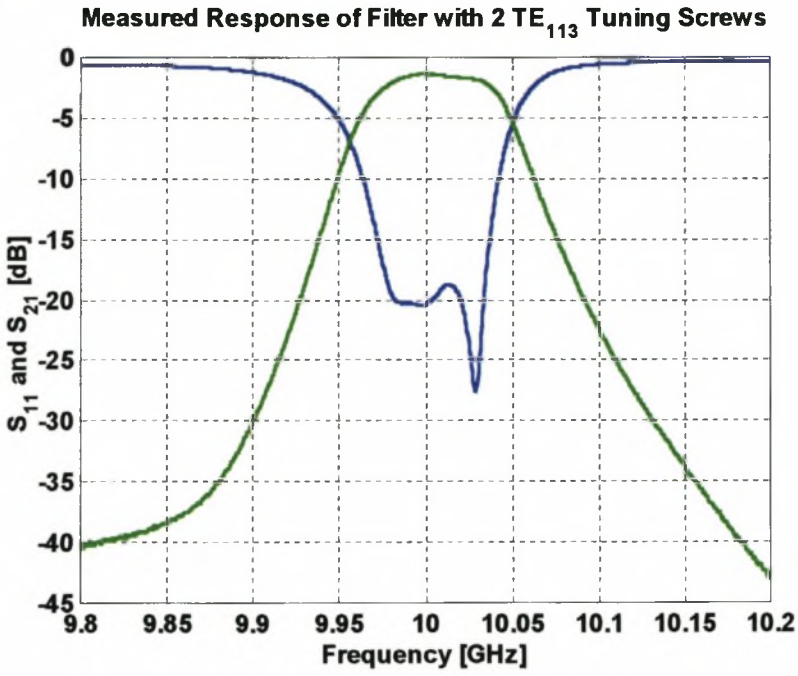

Figure 8.11: Measured response of triple-mode filter using two tuning screws

This response agrees very well with the theoretical predictions. Table 8.1 summarises the comparison between expected and measured filter parameters.

Table 8.1

Comparison of Measured Response and Design Specifications

	Desired	Measured
F_0	10 GHz	10.01 GHz
Bandwidth	0.5 %	0.505 %
Reflection Loss in Passband	-23 dB	-18 dB
Insertion Loss	0.45 dB	1.36 dB

The centre frequency and filter bandwidth are in very good agreement with the designed values. A small error in the input/output irises, or slight detuning of the TM_{012} resonator, which could not be controlled in this case, may be the cause of the error in reflection loss. The expected insertion loss was calculated using 50% of the mean of the unloaded Q-values of the TE_{113} and TM_{012} modes in the aluminium

cavity. The use of the high order modes results in low insertion loss, even for very narrow-band filters. Most of the unexpected measured insertion loss can be ascribed to surface roughness inside the cavity, with a small contribution added by the two tuning screws. From figure 8.10 it can also be seen that the insertion loss is lower when no tuning screws are used.

The performance of the final filter is still remarkable. In the case of traditional triple mode cavity filters, two coupling screws and three tuning screws would be required. In this filter, the new coupling element completely replaced coupling screws, and the number of tuning screws was reduced to two. While some improvement in insertion loss could be expected from the reduction of screws penetrating into the cavity body, the biggest effect can be seen in the time spent on the tuning of the filter. For the filter without any screws, a relatively good result was obtained without any tuning, while in the second case, only the tuning of two resonator frequencies was required.

8.4 CONCLUSION

A new coupling element for the replacement of coupling screws and reduction of tuning screws was presented.

The coupling element is basically a shorted rectangular waveguide stub placed in the end-walls of a cavity. Correct positioning can result in dual-mode and triple-mode coupling. Since this element can be treated as an off-centred iris structure, the CAD procedures developed in chapter 6 can be used for the efficient design of filter structures.

The first triple-mode cavity filter without coupling screws was designed and manufactured. Measurements of this filter without any screws showed the feasibility of the coupling structure and the design algorithms. The addition of two tuning screws resulted in a simple filter structure that required minimal tuning effort and matched the predicted filter response very closely.

Chapter 9

Conclusion and Future Work

With the ever-increasing complexity of multi-mode coupled cavity filter structures and the strain on existing design techniques, the aim of this dissertation was the development of efficient CAD-based iris design procedures for multi-mode coupled cavity devices. Three CAD procedures, each aimed at a different class of iris design problem, were developed and presented. Their design capabilities include iris structures with centred and off-centred, single and multiple aperture irises, for coupling between synchronous and asynchronously tuned identical and non-identical cavity resonators.

The first CAD procedure was based on the existing EM-technique for the calculation of coupling coefficients from the natural resonant frequencies. These frequencies are obtained from the roots of a characteristic equation. This method was enhanced by firstly applying an Adaptive Sampling Algorithm with Rational Interpolation to minimise the number of frequency evaluations over the band of interest. The isolation of specific coupling modes by reducing the entries in the Generalised Scattering Matrix of the structure, was shown to reduce the complexity and increase coupling coefficient computation speed. Optimisation with Aggressive Space Mapping, which minimises the number of EM coupling coefficient calculations, produces an efficient design procedure for the design of irises in many filter applications where cross-coupling between modes does not occur.

A second CAD procedure was developed to account for the effects of cross-coupling between modes in coupled cavity systems. This technique allows for the accurate evaluation of all coupling coefficients, including cross-coupling, as well as resonant frequencies of modes. While it was shown that the direct coupling coefficients can be obtained from an equivalent reactance description of an iris, this is not yet possible for the cross-coupling terms. The development of a technique whereby all coupling coefficients are determined directly from the scattering parameters of an iris will be of great value and should be pursued in future work.

For applications where coupling between asynchronous resonators is desired, or where cross-coupling between modes at different resonant frequencies does occur, a third CAD procedure was developed. The use of this procedure for iris design in a multi-mode environment was validated by the design and manufacture of a diplexer realising two fourth order Chebyschev filter functions in three quadruple-mode cavities. Using the CAD procedure the channel isolation was greatly improved by correct placement and accurate design of the coupling irises. The flexibility and robustness of the CAD procedure allows for a large amount of future work on complex applications such as this. A next iteration in diplexer design should certainly include elliptical filter channels and better suppression of the spurious modes, which lie within the capabilities of the CAD procedures.

This thesis also presented the development of a new coupling structure that can replace coupling screws and reduce the number of tuning screws in multi-mode waveguide filters. Since the coupling structure is very similar to an iris structure the CAD techniques presented here can also be used for CAD of degenerate mode coupling inside a single cavity. A third order triple-mode Chebyschev filter without coupling or tuning screws was designed and manufactured and good agreement between measured and theoretical prediction is observed. Future work in this area would include the extension of the design to more than one cavity for more practical filter applications. This coupling element should also be included in other applications such as the diplexer design in order to reduce the number of coupling screws. Coupling screws do not only control coupling but also influence resonant frequencies. The replacement of a coupling screw by a fixed coupling element therefore reduces the complexity of the tuning process considerably.

The CAD procedures presented in this dissertation allow for the design of a wide range of high performance passive microwave components and are certainly not limited to the applications detailed here. It is hoped that these procedures will be enhanced by future researchers and applied beyond the borders of this thesis.

References

[1] G. L. Ragan, Ed. Microwave Transmission Circuits, M.I.T. Rad. Lab. Series, Vol. 9, New York, McGraw Hill, 1948.

[2] H. A. Bethe, "Theory of Diffraction by small holes", *Phys. Rev.*, Vol. 66, pp. 163 - 182, Oct. 1944.

[3] S. B. Cohn, "Determination of Aperture Parameters by Electrolytic-Tank Measurements", *Proceedings of the IRE*, Vol. 39, pp. 1416 - 1421, November 1951.

[4] W. G. Lin, "Microwave Filters Employing a Single Cavity Excited in More Than One Mode", *Journal of Applied Physics*, Vol. 22, No. 8, pp. 989 - 1001, August 1951.

[5] A. E. Williams, "A Four-Cavity Elliptic Waveguide Filter", *IEEE Transactions on Microwave Theory and Techniques*, Vol. MTT-18, No. 12, pp. 1109 - 1114, December 1970.

[6] A. E. Atia, A. E. Williams, "New Types of Waveguide Bandpass Filters for Satellite Transponders", *COMSAT Technical Review*, Vol. 1, No. 1, 1971.

[7] U. Rosenberg, D. Wolk, "Filter Design Using In-Line Triple-Mode Cavities and Novel Iris Couplings", *IEEE Transactions on Microwave Theory and Techniques*, Vol. 37, No. 12, pp. 2011 - 2019, December 1989.

[8] R. R. Bonetti, A. E. Williams, "Quadruple-Mode Filters", *IEEE MTT-S Int. Microwave Symp. Digest*, pp. 145 - 147, 1987.

[9] A. Chatterjee, J. M. Jin, J. L. Volakis, "Computation of Cavity Resonances Using Edge-Based Finite Elements", *IEEE Transactions on Microwave Theory and Techniques*, Vol. 40, No. 11, pp. 2106 - 2108, November 1992.

[10] R. Yang, S. S. Omar, "Rigorous Analysis of Iris Coupling Problem in Waveguide", *IEEE Transactions on Microwave Theory and Techniques*, Vol. 41, No. 2, pp. 349 - 352, February 1993.

[11] P. H. Harms, J. Lee, R. Mittra, "A Study of Nonorthogonal FDTD Methods Versus the Conventional Technique for Computing Resonant Frequencies of Cylindrical Cavities", *IEEE Transactions on Microwave Theory and Techniques*, Vol. 40, No. 4, pp. 741 - 746, April 1992.

[12] A. B. Omar, K, Schünemann, "Transmission Matrix Representation of Finline Discontinuities", *IEEE Transactions on Microwave Theory and Techniques*, Vol. 33, No. 9, pp. 765 - 770, September 1985.

[13] J. D. Wade, R. H. Macphie, "Scattering at Circular-to-Rectangular Waveguide Junctions", *IEEE Transactions on Microwave Theory and Techniques*, Vol. MTT-34, No. 11, pp. 1085 - 1091, November 1986.

[14] C. Sabatier, "Scattering at an Offset Circular Hole in a Rectangular Waveguide", *IEEE Transactions on Microwave Theory and Techniques*, Vol. 40, No. 3, pp. 587 - 592, March 1992.

[15] F. Alessandri, M. Mongiardo, R. Sorrentino, "Computer-Aided Design of Beam Forming Networks for Modern Satellite Antennas", *IEEE Transactions on Microwave Theory and Techniques*, Vol. 40, No. 6, pp. 1117 - 1127, June 1992.

[16] H. Chang, K. A. Zaki, "Evanescent-Mode Coupling of Dual-Mode Rectangular Waveguide Filters", *IEEE Transactions on Microwave Theory and Techniques*, Vol. 39, No. 8, pp. 1307 - 1312, August 1991.

[17] Hui-Wen Yao, Ji-Fuh Liang, and Kawthar A. Zaki, "Accuracy of Coupling Computations and its Application to DR Filter Design", *IEEE MTT-S Symposium Digest*, pp. 723 - 726, 1994.

[18] P. Guillot, H. Baudrand, S. Vigneron, B. Theron, "Complete Design for Five-Pole In Line Elliptic Filter", *IEEE MTT-S Int. Microwave Symp. Digest*, pp. 505 - 508, 1995.

[19] U. Rosenburg, "Multiplexing and Double Band Filtering with Common-Multimode Cavities", *IEEE Transactions on Microwave Theory and Techniques*, Vol. 38, No. 12, pp. 1862 - 1871, December 1990.

[20] W. Steyn, R. Lehmensiek, P. Meyer, "Integrated CAD Procedure for Iris Design in a Multi-Mode Waveguide Environment", *MTT-S International Microwave Symposium Digest*, May 2001.

[21] A. E. Atia, A. E. Williams, R. W. Newcomb, "Narrow-Band Multi-Coupled Cavity Synthesis", *IEEE Transactions on Circuits and Systems*, Vol. CAS-21, No. 5, pp. 649 - 655, September 1974.

[22] A. E. Atia, "Narrow-Bandpass Waveguide Filters", *IEEE Transactions on Microwave Theory and Techniques*, Vol. MTT-20, No. 4, pp. 258 - 265, April 1972.

[23] R. J. Cameron, "General Coupling Matrix Synthesis Methods for Chebyshev Filtering Functions", *IEEE Transactions on Microwave Theory and Techniques*, Vol. 47, No. 4, pp.433 - 442, April 1999.

[24] H. C. Bell, "Canonical Asymmetric Coupled-Resonator Filters", *IEEE Transactions on Microwave Theory and Techniques*, Vol. MTT-30, No. 9, pp. 1335 - 1340, September 1982.

[25] J. D. Rhodes, I. H. Zabalawi, "Synthesis of Symmetrical Dual Mode Inline Prototype Networks", *Circuit Theory and Applications*, Vol. 8, pp. 145 - 160, 1980.

[26] R. J. Cameron, "Dual-Mode Realisations for Asymmetric Filter Characteristics", *ESA Journal*, Vol. 6, pp. 339 - 356, 1982.

[27] R. J. Cameron, J. D. Rhodes, "Asymmetric Realisations for Dual-Mode Bandpass Filters", *IEEE Transactions on Microwave Theory and Techniques*, Vol. MTT-29, No. 1, pp. 51 - 58, January 1981.

[28] J. D. Rhodes, "The Generalised Direct-Coupled Cavity Linear Phase Filter", *IEEE Transactions on Microwave Theory and Techniques*, Vol. MTT-18, No. 6, pp. 308 - 313, June 1970.

[29] S. Darlington, "Synthesis of Reactance 4-Poles which Produce Prescribed Insertion Loss Characteristics", *Journal of Mathematics and Physics*, Vol. 18, No. 4, pp. 257 - 353, 1939.

[30] M. E. Van Valkenburg, Introduction to Modern Network Synthesis, New York: Wiley, 1960.

[31] J. D. Rhodes, Theory of Electrical Filters, Wiley - Interscience, 1976.

[32] J. A. Frame, "Matrix Functions and Applications", *IEEE Spectrum*, Vol. 1, No. 6, pp. 123 - 131, June 1964.

[33] W. A. Atia, K. A. Zaki, and A. E. Atia, "Synthesis of general topology multiple coupled resonator filters by optimisation", *IEEE Microwave Theory and Techniques International Symposium Digest*, pp. 821 - 824, 1998.

[34] L. O. Chua, Pen-Min Lin, Computer-Aided Analysis of Electronic Circuits, Prentice-Hall Inc, Englewood Cliffs, New Jersey, Sec. 9-5, pp. 377 - 384, 1975.

[35] S. Amari, "Synthesis of Cross-Coupled Resonator Filters Using an Analytical Gradient-Based Optimisation Technique", *IEEE Transaction on Microwave Theory and Technique*, Vol. 48, No.9, Sept 2000.

[36] S. Ramo, J. R. Whinnery and T. Van Duzer, Fields and Waves in Communication Electronics, Third Edition, John Wiley and Sons, Inc., Canada, 1994.

[37] R. E. Collin, Foundations for Microwave Engineering, Second Edition, McGraw-Hill, Inc., Singapore, 1992.

[38] R. M. Kurzrok, "Couplings in Direct-Coupled Waveguide Band-Pass Filters", IRE Transactions on Microwave Theory and Techniques, Vol. 50, pp. 389 - 390, September 1962.

[39] S. B. Cohn, "The Electric Polarisability of Apertures of Arbitrary Shape", *Proceedings of the IRE*, Vol. 40, pp. 1069 - 1071, September 1952.

[40] S. B. Cohn, "Microwave Coupling by Large Apertures", *Proceedings of the IRE*, Vol. 7, pp. 696 - 699, June 1952.

[41] R. Levy, "Improved Single and Multiaperture Waveguide Coupling Theory, Including Explanation of Mutual Interactions", *IEEE Transactions on Microwave Theory and Techniques*, Vol. MTT-28, No. 4, pp. 331 - 338, April 1980.

[42] N. A. McDonald, "Electric and Magnetic Coupling through Small Apertures in Shield Walls of Any Thickness", *IEEE Transactions on Microwave Theory and Techniques*, Vol. MTT-20, No. 10, pp. 689 - 695, October 1972.

[43] J. Uher, J. Bornemann, U. Rosenberg, Waveguide Components for Antenna Feed Systems: Theory and CAD. Artech House, Boston, 1993.

[44] G. Matthaei, L. Young, E. M. T. Jones, Microwave Filters. Impedance-Matching Networks, and Coupling Structures. Artech House, Dedham Massachusetts, 1980.

[45] U. Rosenberg, D. Wolk, "New Possibilities of Cavity-Filter Design by a Novel TE-TM- Mode Iris Coupling", *IEEE MTT-S Int. Microwave Symp. Digest*, pp. 1155 - 1158, 1989.

[46] E. Arvas, R. F. Harrington, "Computation of the Magnetic Polarizability of Conducting Disks and the Electric Polarizability of Apertures", *IEEE Transactions on Antennas and Propagation*, Vol. AP-35, No. 5, pp. 719 - 724, September 1983.

[47] K L. Wu, "An Optimal Circular-Waveguide Dual-Mode Filter Without Tuning Screws", *IEEE Transactions on Microwave Theory and Techniques*, Vol. 47, No. 3, March 1999.

[48] L. Q. Bui, D. Ball, "Broad-Band Millimeter-Wave E-plane Bandpass Filters", *IEEE Transactions on Microwave Theory and Techniques*, Vol. MTT-32, No. 12, pp. 1655 – 1658, December 1984.

[49] A. E. Williams, A. E. Atia, "Dual-Mode Canonical Waveguide Filters", *IEEE Transactions on Microwave Theory and Techniques*, Vol. MTT-25, No. 12, pp. 1021 - 1026, December 1977.

[50] L. Accatino, G. Bertin, M. Mongiardo, "A Four-Pole Dual Mode Elliptic Filter Realized in Circular Cavity Without Screws", *IEEE Transactions on Microwave Theory and Techniques*, Vol. 44, No. 12, pp. 2680 - 2686, December 1996.

[51] H. L. Thal, "Microwave Filter Loss Mechanisms and Effects", *IEEE Transactions on Microwave Theory and Techniques*, Vol. MTT-30, No. 9, pp. 1330 - 1334. September 1982.

[52] M. Dishal, "Alignment and adjustment of syncronously tuned multipleresonator circuit filters", *Proc. IRE*, Vol. 39, pp. 1448 - 1455, Nov. 1951

[53] A. E. Atia, A. E. Williams, "Measurement of Intercavity Couplings", *IEEE Transactions on Microwave Theory and Techniques*, Vol. 23, pp. 519 - 522, June 1975.

[54] A. E. Williams, R. G. Egri, R. R. Johnson, "Automatic Measurement of Filter Coupling Parameters", *IEEE MTT-S International Symposium Digest*, pp. 418 - 420, 1983.

[55] N. A. McDonald, "Measurement of Intercavity Couplings", *IEEE Transactions on Microwave Theory and Techniques*, Vol. MTT-24, No.3, p. 162, March 1976.

[56] A. E. Atia, Hui-Wen Yao, "Tuning and Measurement of Couplings and Resonant Frequencies for Cascaded Reosonators", *IEEE MTT-S International Symposium Digest*, June 2000.

[57] M. H. Chen, "Short-Circuit Tuning Method for Singly Terminated Filters", *IEEE Transactions on Microwave Theory and Techniques*, Vol. MTT-25, No. 12, pp. 1032 - 1036, December 1977.

[58] J. B. Ness, "A Unified Approach to the Design, Measurement, and Tuning of Coupled-Resonator Filters", *IEEE Transactions on Microwave Theory and Techniques*, Vol. 46, No. 4, pp. 343 - 351, April 1998.

[59] L. Accatino, "Computer-Aided Tuning of Microwave Filters", *IEEE MTT-S Int. Microwave Symp. Digest*, pp. 249 - 252, 1986.

[60] M. Kahrizi, S. Afavi-Naeini, S. K. Chaudhuri, "Computer Diagnosis and Tuning of Microwave Filters using Model-based Parameter Estimation and Multi-level Optimization", *IEEE MTT-S International Symposium Digest*, June 2000.

[61] H. L. Thal, "Computer-Aided Filter Alignment and Diagnosis", *IEEE Transactions on Microwave Theory and Techniques*, Vol. MTT-26, No. 12, pp. 958 - 963, December 1978.

[62] P. Couffignal, H. Baudrand, B. Théron, "A New Rigorous Method for the Determination of Iris Dimensions in Dual-Mode Cavity Filters", *IEEE Transactions on Microwave Theory and Techniques*, Vol. 42, No. 7, pp. 1314 - 1320, July 1994.

[63] "Simplified Filter Tuning Using Time Domain", *Agilent Application note* 1287-8.

[64] "Advanced Filter Tuning Using Time Domain Transforms", *Agilent Application note* 1287-10.

[65] F. Arndt, R. Beyer, J. M. Reiter, T. Sieverding, T. Wolf, "Automated Design of Waveguide Components Using Hybrid Mode-Matching/Numerical EM Building Blocks in Optimisation - Oriented CAD Frameworks - State-of-the-Art and Recent Advances", *IEEE Transactions on Microwave Theory and Techniques*, Vol. 45, No. 5, pp. 747 - 759, May 1997.

[66] S. Costiner, F. Manolache, S. Ta'asan, "Multilevel Methods Applied to the Design of Resonant Cavities", *IEEE Transactions on Microwave Theory and Techniques*, Vol. 43, No. 1, pp. 48 - 54, January 1995.

[67] J. Ma Gil, J. P. Webb, "A New Edge Element for the Modeling of Field Singularities in Transmission Lines and Waveguides", *IEEE Transactions on Microwave Theory and Techniques*, Vol. 45, No. 12, pp. 2125 - 2130, December 1997.

[68] R. Lehmensiek and P. Meyer, "Using efficient model-based parameter estimation for pole-free solutions of modal propagation constants, as applied to shielded planar structures," *Applied Computational Electromagnetics Society Journal*, to be published.

[69] J. W. Bandler, R. M. Biernacki, S. H. Chen, P. A. Grobelny, and R. H. Hemmers, "Space mapping technique for electromagnetic optimization", *IEEE Transactions on Microwave Theory and Techniques*, Vol. 42, pp. 2536 - 2544, 1994.

[70] G. G. Gentili, "Properties of TE-TM mode-matching techniques," *IEEE Transactions on Microwave Theory and Techniques*, Vol. 39, pp. 1669 - 1673, Sept. 1991.

[71] C. A. W. Vale, Growth-based Computer Aided Design Strategies for Multimode Design with the Aid of Functional Blocks, *Ph.D. Dissertation*, University of Stellenbosch, 2001.

[72] G. V. Eleftheriades, A. S. Omar, L. P. B. Katehi, G. M. Rebeiz, "Some Important Properties of Waveguide Junction Generalized Scattering Matrices in the Context of the Mode Matching Technique", *IEEE Transactions on Microwave Theory and Techniques*, Vol. 42, No. 10, pp. 1896 - 1903, October 1994.

[73] F. Dai, "Scattering and Transmission Matrix Representations of Multiguide Junctions," *IEEE Transactions on Microwave Theory and Techniques*, Vol. 40, o. 7, pp. 1538 - 1544, July 1992

[74] R. Keller, F. Arndt, "Rigorous Modal Analysis of the Asymmetric Rectangular Iris in Circular Waveguides", *IEEE Microwave and Guided Wave Letters*, Vol. 3, No. 6, June 1993.

[75] C.A.W Vale and P.Meyer "Automated Intelligent Mode Selection for Fast Mode Matching Analysis of Waveguide Discontinuities," *IEEE MTT-S Intl. Symp. Digest,* Phoenix, 20-25 May 2001.

[76] L. Accatino, G. Bertin, "Design of Coupling Irises Between Circular Cavities by Modal Analysis", *IEEE Transactions on Microwave Theory and Techniques*, Vol. 42, No. 7, pp. 1307 - 1313, July 1994.

[77] A.S. Omar and K. Schunemann, "Tarnsmission Matrix Representation of Finline Discontinuities," *IEEE Trans. Microwave Theory Tech.*, vol. MTT-34, no.9, pp. 765-770, Sept. 1985.

[78] J. W. Bandler, R. M. Biernacki, S. H. Chen, R. H. Hemmers and K. Madsen, "Electromagnetic optimization exploiting aggressive space mapping," *IEEE Trans. Microwave Theory Tech.*, vol. 43, pp. 2874-2882, 1995.

[79] H. J. Riblet, "Waveguide filter having nonidentical sections resonant at same fundamental and different harmonic frequencies", US Patent No. 3,153,208, 1964.

[80] Rosenberg, U, "A New Multiplexing Principle", *IEEE MTT-S International Microwave Symposium Digest*, pp. 203 - 206, 1990.

[81] C. Kudsia, R. Cameron, W. Tang, "Innovations in Microwave Filters and Multiplexing Networks for Communications Satellite Systems", *IEEE Transactions on Microwave Theory and Techniques*, Vol. 40, No. 6, pp. 1133 - 1149, June 1992.

[82] J. M. Reiter, F. Arndt, "Rigorous Analysis of Arbitrarily Shaped H- and E-Plane Discontinuities in Rectangular Waveguides by Full-Wave Boundary Contour Mode-Matching Method", *IEEE Transactions on Microwave Theory and Techniques*, Vol. 43, No. 4, pp. 796 - 801, April 1995.

[83] A. Melloni, M. Politi, G. G. Gentili, "Mode-Matching Analysis of TE_{011}-Mode Waveguide Bandpass Filters", *IEEE Transactions on Microwave Theory and Techniques*, Vol. 43, No. 9, pp. 2109 - 2116, September 1995.

[84] X. Liang, K. A. Zaki, A. E. Atia, "Dual Mode Coupling by Square Corner Cut in Resonators and Filters", *IEEE Transactions on Microwave Theory and Techniques*, Vol. 40, No. 12, pp. 2294 - 2301, December 1992.

[85] J. Liang, X. Liang, K. A. Zaki, A. E. Atia, "Dual-Mode Dielectric or Air-Filled Rectangular Waveguide Filters", *IEEE Transactions on Microwave Theory and Techniques*, Vol. 42, No. 7, pp. 1330 - 1336, July 1994.

[86] G. Lastoria, G. Gerini, M. Guglielmi, F. Emma, "CAD of Triple-Mode Cavities in Rectangular Waveguide", *IEEE Microwave And Guided Wave Letters*, Vol. 8, No. 10, pp.339 - 341, October 1998.

[87] R. Orta, P. Savi, R. Tascone, D. Trinchero, "Rectangular Waveguide Dual-Mode Filters Without Discontinuities Inside the Resonators", *IEEE Microwave and Guided Wave Letters*, Vol. 5, No. 9, pp. 302 - 304, September 1995.

[88] M. Guglielmi, R. C. Molina, A. A. Melcon, "Dual-Mode Circular Waveguide Filters Without Tuning Screws", *IEEE Microwave and Guided Wave Letters*, Vol. 2, No. 11, November 1992.

[89] R. Beyer, F. Arndt, "Efficient Modal Analysis of Waveguide Filters Including the Orthogonal Mode Coupling Elements by an MM/FE Method", *IEEE Microwave and Guided Wave Letters*, Vol. 5. No. 1, January 1995.

[90] L. Accatino, G. Bertin, M. Mongiardo, "A Four-Pole Dual Mode Elliptic Filter Realized in Circular Cavity Without Screws", *IEEE MTT-S Int. Microwave Symp. Digest*, pp. 627 - 629, 1996.

[91] L. Accatino, G. Bertin, M. Mongiardo, "Elliptical Cavity Resonators for Dual-Mode Narrow-Band Filters", *IEEE Transactions on Microwave Theory and Techniques*, Vol. 45, No. 12, pp. 2393 - 2401, December 1997.

APPENDIX A

Gram-Schmidt Orthonormalisation Process

Orthogonal sets of vectors simplify mathematical manipulations. The Gram-Schmidt process uses a set of linearly independent vectors to construct an orthogonal basis. If the given set of linearly independent vectors are $\mathbf{X}_i$, the corresponding orthogonal vectors $\mathbf{V}_i$ can be found by a recursive formula [1, 2]:

$$\mathbf{V}_i = \mathbf{X}_i - \frac{\mathbf{X}_i \cdot \mathbf{V}_1}{\mathbf{V}_1 \cdot \mathbf{V}_1}\mathbf{V}_1 - \frac{\mathbf{X}_i \cdot \mathbf{V}_2}{\mathbf{V}_2 \cdot \mathbf{V}_2}\mathbf{V}_2 - \cdots - \frac{\mathbf{X}_i \cdot \mathbf{V}_{i-1}}{\mathbf{V}_{i-1} \cdot \mathbf{V}_{i-1}}\mathbf{V}_{i-1}$$

These vectors need to be normalised to unit vectors to produce a set of orthonormal vectors.

References:

[1] R. H. Lance, "Orthogonal Sets", *http://tam.cornell.edu/courses/math293/L41/L41.html*, Math 293, Lecture 41, Cornell University, 5 January 1996.

[2] H. Anton, Elementary Linear Algebra, 6th edition, Wiley & Sons, New York, 1991.